UNIVERSITY OF CALIFORNIA, SAN DIEGO

# Marine Electromagnetic Methods for Gas Hydrate Characterization

A dissertation submitted in partial satisfaction of the
requirements for the degree Doctor of Philosophy
in
Earth Sciences

by

Karen Andrea Weitemeyer

Committee in charge:

Professor Steven Constable, Chair
Professor Kevin Brown
Professor Jeffrey Gee
Professor Stefan Llewellyn Smith
Professor Robert Parker

2008

The dissertation of Karen Andrea Weitemeyer is approved, and it is acceptable in quality and form for publication on microfilm:

---

---

---

---

---

Chair

University of California, San Diego

2008

*To my grandma Elisabeth Weitemeyer, who with a determined look, advised me to stay in school as long as possible. And to my grandpa Bert Weitemeyer, who told me I could be anything I wanted to be.*

"Always saddle your own horse" - *Connie Douglas Reeves (1901-2003).*

TABLE OF CONTENTS

LIST OF FIGURES

LIST OF TABLES

# ACKNOWLEDGMENTS

The journey leading up to a doctorate degree requires self-determination, but also necessary is the support from family, friends and colleagues.

First I would like to thank my advisor Professor Steven Constable for creating opportunities to pursue my interest in gas hydrates and electromagnetic methods. When I first came to Scripps Institution of Oceanography I would have never imagined I would be at sea collecting marine electromagnetic data in such places as India, Hawaii, the Gulf of Mexico, offshore Oregon and San Diego. Nor would I have ever thought there would be such a large network of people (academic and industrial) interested in our research. I thank him for pushing me to be a better scientist and writer. Within a year of being at Scripps Institution of Oceanography he arranged for the collection of my thesis data: an electromagnetic survey at Hydrate Ridge, Oregon made possible by funding from Exxon Mobil and GERD, Japan. I wish to thank the captain and crew of the R.V. New Horizon and the scientific party: Chester Weiss, Adam Schultz, Yamane Kazunobu, Chris Winters, Garth Engelhorn, Chris Armerding, Patricia Cheng-Terry, Courtney Schatzman, James Behrens, Kerry Key, Steve Constable, and the land based crew Jacques Lemire, and John Souders. I thank Anne Tréhu for early discussions in cruise planning, for providing seismic data and for later discussions and general encouragement.

I benefited from the knowledge and experience of Steven Constable as well as his past students: Jim Behrens and Kerry Key. I thank Jim for making a special effort to explain the basics of controlled source electromagnetic methods and for answering my many questions in processing CSEM data as well as for the use of his SFT6 processing code. I thank Kerry for allowing me the time to talk with him about electromagnetic methods and computational questions. Kerry Key's 1D modeling code and Marquardt script used in Chapter 5 was instrumental in solving for the navigation of the transmitter. Yugou Li and Kerry Key are thanked for the

development of the finite element forward modeling code used in Chapter 6. Using the code has been a very educational process and having Yugou and Kerry at hand to answer questions and explain results has been very beneficial. The 2D inversion (Chapter 6 and 7) of the Hydrate Ridge data was made possible by collaboration with David Alumbaugh and Guozhong Gao of EMI-Schlumberger. My trips to Oakland were always very productive and I thank them for the opportunity and assistance, as the 2D inversion of the data is a significant result.

The Seafloor Electromagnetics Consortium provided much of my funding and some additional funding came from the Society of Exploration Geophysicists to attend meetings and this also provided some personal financial support.

I thank some new members of the EM Lab crew: Cambria Colt and Jake Perez for sharing in some amazing adventures, I am sure there will be many more to come. I also am glad to have fellow students David Myer and Brent Wheelock around to talk to about EM.

I also thank my committee members for taking an interest in my research: Professor Robert Parker for reference letters and general encouragement, Professor Jeff Gee for assistance in ODP logging results, Professor Stefan Llewellyn Smith for keeping this thesis short, and Professor Kevin Brown for early discussions.

I am grateful to Catherine de-Groot-Hedlin for taking me, in my first year, out into the field to collect land MT data, and for the good company of Lucrezia Terzi. You couldn't ask for a much prettier place to do field work than Yellowstone and the Snake River Plain.

I wish to thank Dan Orange, Marianne Mulrey, and Dan McConnell for the opportunity to spend some time working on industry data and with industry relevant problems. I thank them for their encouragement and sharing their knowledge with me about electromagnetic methods and hydrates. I thank Arnie and Marget Orange for their hospitality in Austin. I thank Arnie for publicizing my work and presenting it around the world and for connecting us with the Economic Bureau of Geology in Austin Texas.

I thank the faculty in the UBC geophysics program for their encouragement and Bruce Buffett for convincing me to think and dream big. I thank Ted Lilley for the opportunity to work with him in Australia and his suggestion that I rethink my decision as to which graduate school I should attend.

I have many friends to thank, and I guess I did not realize how many friends I had until my surprise birthday this year - thank you. I thank my fellow Canucks Jill Pearse and Lindsay Smith for many laughs and conversations. I thank my good friend Guoqing Lin for many many fun salsa dancing classes, and venturing to the many salsa clubs in San Diego. I thank Bettina Allmann and Alexander Goertz, my very good friends, for both academic stimulation as well as many many outback adventures - thanks for letting me be a third wheel, I will never forget our times together. Urska Manners is thanked for her tea times and funny sense of humor; Ashley Medin for being a great roommate and resource person; my Keller-mates: Bettina Allmann, Karen Luttrell, Kristin Lawrence, Ashley Medin, John Blum, and Robert Kern - note that Karen Luttrell and Bettina Allmann are the GMT gurus! My horsey friends are also to be thanked: Jane Wiggins who in my first year let me spend many weekends at the funny farm riding and doing farm things. Virginia and Guy Masters are also thanked for unlimited access to riding their horse Stoli. I cannot thank them enough for keeping me in the saddle while in San Diego. I never knew extreme trail riding until I went with Guy. I also thank Virginia for the horse rides and lovely dinners that would follow, and for 'adopting' me while here. I also would like to thank Rafael for sharing his horsemanship knowledge and for friendship.

I also thank Steve and Cathy Constable for the many dinners at the Constabulary and for inviting me to attend Opera and symphonies. These events made me feel very welcome.

I wish to thank my family Mom, Dad, my sister Theresa, Chad, Kendra, Edithe; my brother Rob; Grandma; Auntie Chris and Uncle Tom, James and Nicole, Jeff and Chloe; Auntie Judy, Uncle Murray and Patrick.

## VITA

| | |
|---|---|
| 2003 | B.Sc. Honors Geophysics<br>University of British Columbia, Vancouver |
| 2003–2008 | Research Assistant<br>Scripps Institution of Oceanography,<br>University of California, San Diego |
| 2006 | Consulting Geophysicist, AOA Geophysics/AOA Geomarine Operations |
| 2008 | Ph.D., Earth Science<br>Scripps Institution of Oceanography,<br>University of California, San Diego. |

## PUBLICATIONS

Lilley, F.E.M. and K.A. Weitemeyer, 2004: Apparent aeromagnetic wavelengths of the magnetic signals of ocean swell. *Exploration Geophysics*, 35,137–141.

Weitemeyer, K.A., Constable, S.C., Key, K.W., Behrens, J.P., 2006: First results from a marine controlled-source electromagnetic survey to detect gas hydrates offshore Oregon. *Geophysical Research Letters*, 33(3), doi:10.1029/2005GL024, 896.

Weitemeyer, K. A. and B. A. Buffett, 2006: Accumulation and release of methane from clathrates below the Laurentide and Cordilleran ice sheets. *Global and Planetary Change*, 53(3),176–187.

Weitemeyer, K., Constable S., Key K., 2006: Marine EM techniques for gas-hydrate detection and hazard mitigation. *The Leading Edge*, 25 (5),629–632.

## SELECTED PRESENTATIONS

Weitemeyer, K.A. and B.A. Buffett, 2002: Clathrates, ice sheets and global climate change? *Eos, Transactions, American Geophysical Union*, vol. 83 no. 47. Suppl. Abstract PP62B-09, San Francisco, California.

de Groot-Hedlin, C., Constable, S., Booker, J. R., Terzi, L., Weitemeyer, K., 2003: Deep MT Sounding Across the Yellowstone-Snake River Hotspot Track, *Eos, Transactions, American Geophysical Union*, vol.84, no.47, Suppl., Abstract GP12B-06, San Francisco, California.

de Groot-Hedlin, C., Constable, S., Weitemeyer, K., Terzi, L., 2004: Conductivity structure associated with the Yellowstone-Snake River hotspot track, *Eos, Transactions, American Geophysical Union*, vol.85, no.47, Suppl., Abstract GP13A-03, San Francisco, California.

de Groot-Hedlin, C., Constable, S., Weitemeyer, K., Terzi, L., 2004: What can magnetotellurics tell us about the Yellowstone-Snake River Hotspot?, *Geological Society of America, Rocky Mountain Section, 56th annual meeting; Geological Society of America, Cordilleran Section, 100th annual meeting*, Boise, Idaho.

Weitemeyer, K., Constable, S., Key, K. W., Behrens, J., 2004: A pilot marine EM study of Hydrate Ridge, Oregon, *Eos, Transactions, American Geophysical Union*, vol.85, no.47, Suppl., Abstract GP13A-05, San Francisco, California.

Weitemeyer, K., Constable, S., Key, K. W., Behrens, J., 2005: Imaging Gas Hydrate with Marine EM at Hydrate Ridge, Offshore Oregon, *Offshore Technology Conference*, Abstract 17170, Houston, Texas.

Weitemeyer, K., Constable, S., Key, K. W., Behrens, J., 2005: Imaging Gas Hydrate with Marine EM at Hydrate Ridge, Offshore Oregon, *Eos, Transactions, American Geophysical Union* 86(52), Fall Meet. Suppl., Abstract GP41B-0869, San Francisco, California.

Weitemeyer, K., Constable, S., Key, K., 2006: Imaging Submarine Gas Hydrates Using EM Methods, *MARELEC Meeting*, Amsterdam, Netherlands.

Weitemeyer, K., Constable, S., Key, K., 2006: Marine EM studies of Hydrate Ridge, Oregon, USA-imaging hydrates and the accretionary complex, *$18^{th}$ International Workshop on EM Induction in The Earth*, El Vendrell, Spain.

Constable, S., Key K., Weitemeyer, K. A., Myer D., 2006: Reducing Exploration Risk with Marine Electromagnetics: Hydrate Detection and Base Salt Mapping *AAPG International Conference and Exhibition*, Perth, West Australia, Australia.

Orange A., Weitemeyer, K. A., Constable, S., Lewis L., 2006: Marine CSEM, a geophysical technique for identification and characterization of hydrates. *Schlumberger North and South America Reservoir Symposium*, Dubai. UAE.

Orange A., Weitemeyer, K. A., Constable, S., Lewis L., 2006: Marine CSEM, a geophysical technique for identification and characterization of hydrates. *Joint Hydrate and Wellbore Temperature and Heat Transfer Workshop*, Japan.

Weitemeyer, K. A., Constable, S., Alumbaugh, D., 2007: Electromagnetic imaging of hydrates and accretionary structure at Hydrate Ridge, Oregon using 2.5 D model studies, *Eos, Transactions, American Geophysical Union*, 88(52), Fall Meet. Suppl., Abstract GP33B-1249, San Francisco, California.

ABSTRACT OF THE DISSERTATION

Marine Electromagnetic Methods for Gas Hydrate Characterization

by

Karen Andrea Weitemeyer
Doctor of Philosophy in Earth Sciences
University of California, San Diego, 2008
Professor Steven Constable, Chair

Gas hydrate is a type of clathrate consisting of a gas molecule (usually methane) encased in a water lattice, and is found worldwide in marine and permafrost regions. Hydrate is important because it is a geo-hazard, has potential as an energy resource, and is a possible contributor to climate change. There are large uncertainties about the global amount of hydrate present, partly because the characterization of hydrate with seismic methods is unreliable. Marine electromagnetic (EM) methods can be used to image the bulk resistivity structure of the subsurface and are able to augment seismic data to provide valuable information about gas hydrate distribution in the marine environment.

Marine controlled source electromagnetic (CSEM) sounding data from a pilot survey at Hydrate Ridge, located on the Cascadia subduction zone, show that regions with higher concentrations of hydrate are resistive. The apparent resistivities computed from the CSEM data are consistent for both apparent resistivity pseudosections and two-dimensional regularized inversion results. The 2D inversion results provide evidence of a strong resistor near the seismic bottom simulating reflector (BSR), and geologic structures are imaged to about a kilometer depth. Comparisons with electrical resistivity logging while drilling (LWD) data from Ocean Drilling Program Leg 204 show a general agreement except for one of three sites where the CSEM inversion shows a large resistor at depth as compared

to the LWD. An overlay of the CSEM inversion with a collocated seismic line 230 from Tréhu et al. (2001) exhibits remarkable similarities with the sedimentary layering, geologic structures, and the seismic BSR. Magnetotelluric (MT) sounding data collected simultaneously during the CSEM survey provide an electrical image of the oceanic crust and mantle (50 km depth) and the folding associated with the accretionary complex (top 2 km depth). In addition, the MT model provides a complementary low-resolution image for comparison with the CSEM inversion results. The CSEM data characterize the gas hydrate stability zone and both CSEM and MT models map the geologic structures that allow methane to migrate to the gas hydrate stability zone.

# 1

# Introduction

## 1.1 Motivation

Imaging, quantifying and understanding the distribution of hydrate is important for geohazard assessment, resource evaluation, and global climate studies. Remote detection of gas hydrate is unreliable with seismic methods alone and the use of electromagnetic (EM) methods (controlled source electromagnetic and magnetotelluric soundings) to augment seismic data collected over hydrates can provide additional information to constrain the areal extent of hydrate. EM methods image the bulk resistivity structure of the subsurface and may provide valuable information about gas hydrate distribution. EM soundings are possibly the only non-invasive technique capable of quantifying the amount of hydrate present in an area. The EM techniques can be employed to image gas hydrates if a resistivity contrast is present, and also map any geologic structures and fluid pathways that allow methane to migrate to the seafloor and form hydrate.

## 1.2 Gas Hydrates

Natural gas hydrate, a type of clathrate, is an ice-like solid that commonly consists of a methane molecule encaged by a water lattice (Sloan, 1990). Methane hydrates require cool temperatures, high pressures and methane in excess

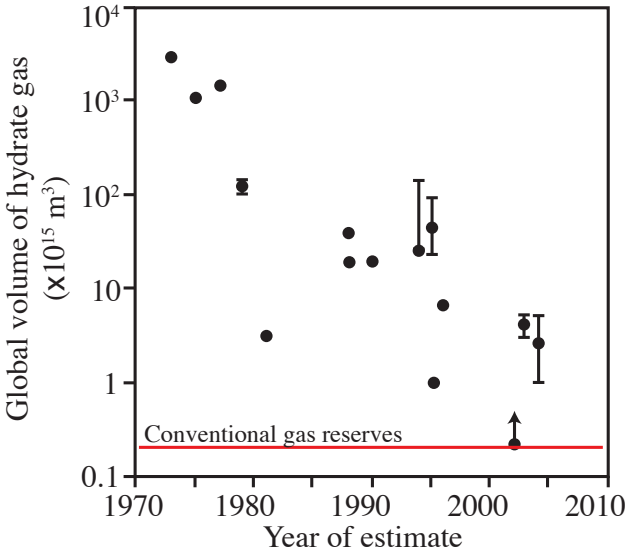


**Figure 1.1**: Global estimate of the offshore gas hydrate resource versus the year each estimate was made and estimate of the world conventional gas reserves (from Milkov and Sassen (2002); Milkov (2004)).

of solubility to form (Kvenvolden, 2003). These conditions are met in both marine and permafrost regions worldwide, and as a result methane hydrates may occur in vast quantities – an estimate of $\sim$ 10,000 Gt of methane in carbon is the highly cited "concensus value" (or 21 x $10^{15}$ $m^3$ of methane at standard temperature and pressure (STP)) (Kvenvolden, 1999; Milkov, 2004). The global hydrate estimate has changed over the past 35 years (Figure 1.1) as a result of continued efforts to directly and indirectly observe hydrates world-wide and by the addition of more complex global models (Archer and Buffett, 2005; Klauda and Sandler, 2005).

Figure 1.2 outlines recent known and inferred gas hydrate locations; evidence is provided by both direct and indirect methods. Four conditions needed for hydrate formation are outlined by Sloan (1990):

**1.** Adequate gas molecules to stabilize most of the hydrate cavities.

**2.** Sufficient water molecules to form the cavity.

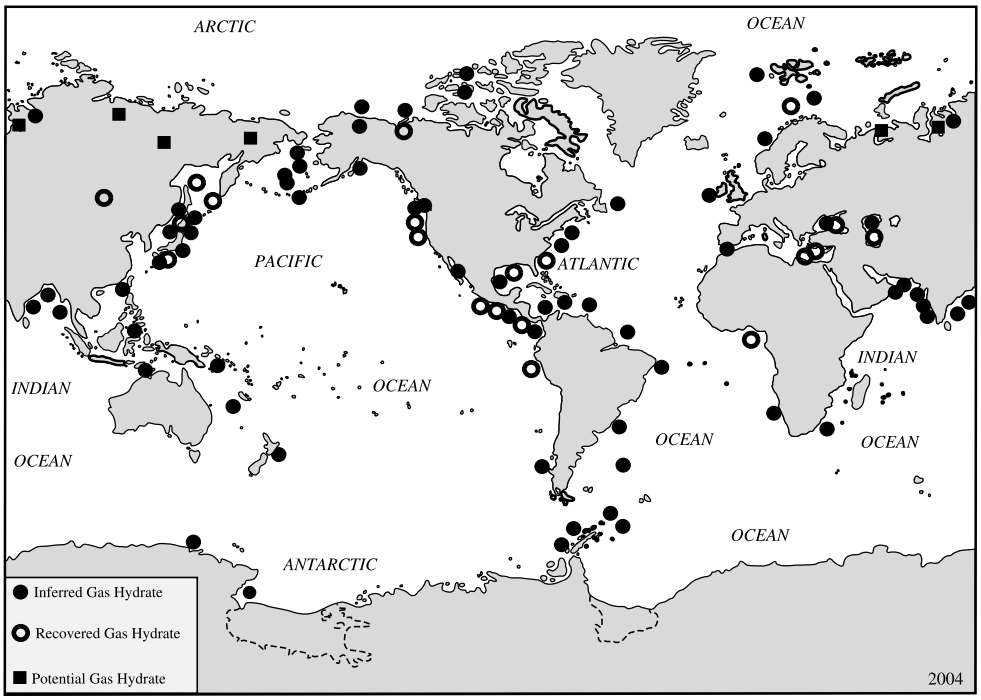


**Figure 1.2**: Worldwide locations of known and inferred gas hydrates; filled circles are locations inferred to have gas hydrate, open circles are regions where samples of gas hydrate have been recovered, and squares are regions for potential gas hydrate occurrence (from Kvenvolden (2005)).

**3.** A temperature within the hydrate phase equilibrium.

**4.** A pressure within the hydrate phase equilibrium.

A phase diagram for a pure water and pure methane system is shown in Figure 1.2. The presence of ions such as NaCl will depress hydrate formation temperature and the presence of other gases such as $CO_2$ will increase the hydrate formation temperature and gas hydrate stability zone (Sloan, 1990; Kvenvolden, 1993a).

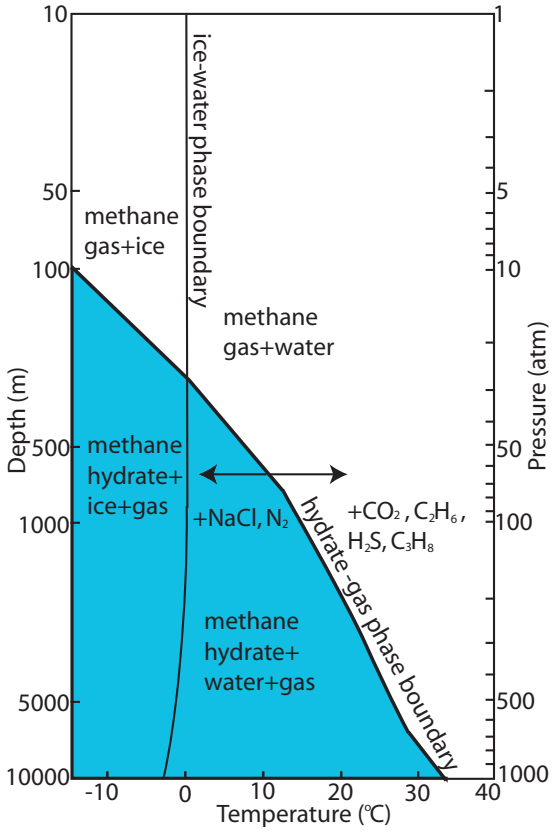


**Figure 1.3**: Phase diagram for a pure water and methane system showing the boundaries for free methane gas (white region) and methane hydrate (blue region). Addition of salt, NaCl, shifts the curve to the left and addition of $CO_2$, $H_2S$, $C_2H_6$, $C_3H_8$ to methane shifts the curve to the right. Figure redrawn from Kvenvolden (1993a).

### 1.2.1 Distribution of Gas Hydrates

Hydrates have been categorized into two types of accumulations: stratigraphic and structural (Milkov, 2005). Stratigraphic hydrate formation is typical of low gas flux regimes in permeable sediment layers and is very dispersed (Milkov, 2005), representing the larger global hydrate reservoir (modeled by Archer and Buffett (2005)). Stratigraphic hydrate is also the most difficult to extract because of its disperse nature (Moridis and Sloan, 2007). Structural hydrate accumulation is typical in high gas flux regimes where gas migrates from deep within the subsurface along faults and permeable layers above petroleum reservoirs; surface features may

result in the form of mud volcanoes, or gas chimneys (Milkov, 2005). Structural accumulations of hydrate are very concentrated and are currently thought to be the economically favorable resource (Milkov and Sassen, 2002).

The natural formation of hydrate can be from one of two processes – thermogenic or biogenic (Sloan, 1990). The thermogenic process is common to natural gas reservoirs, requiring much higher temperatures. Gas migrates from a deep source and may contain such molecules as ethane and higher hydrocarbons (Sloan, 1990; Kvenvolden, 2003). The biogenic process results from methanogenesis whereby microbes living in the sediment break down organic matter and convert it to methane (Sloan, 1990).

Hydrates occur in a variety of geometries within sediment, such as disseminated, nodular, layered, and massive; these may be distributed uniformly or heterogeneously across a region (Malone, 1985). The way hydrate is distributed depends on sediment properties, fluid flow, and the process by which hydrate formed. The geometry of hydrate distribution is dependent on the sediment type. For example, layers and laminae of hydrate are found in fine-grained sediments intrinsically or in fractures; hydrate nodules are numerous in fine sediments as well as sediments with more than one grain size; hydrate cements are associated with coarser sediment types (Spangenberg, 2001). The geometry of hydrate distribution, hydrate growth on grain surfaces, and hydrate growth in the pore space will vastly affect the bulk electrical resistivity by several orders of magnitude (Spangenberg, 2001; Tzirita, 1992). Stern et al. (2004) were able to reproduce very similar grain textures and pore geometries in laboratory-produced pure Structure I (SI) and Structure II (SII) hydrate to those of samples from the Gulf of Mexico, as confirmed by scanning electron microscopy (SEM). The effects of these geometries and textures on the electrical resistivity of hydrate have been largely undocumented and never examined in laboratory studies.

### 1.2.2 Importance of Gas Hydrates

The large stores of concentrated methane found in hydrate (1 volume of hydrate contains 164 volumes of methane gas at STP) has led many countries to view hydrate as a potential energy resource, especially countries without conventional hydrocarbon resources and countries which import energy, such as Japan, China, India, and the USA (Koh and Sloan, 2007; Milkov and Sassen, 2002; Max et al., 2006; Dawe and Thomas, 2007). Concentrated accumulations of hydrate may be the target for mineral resource exploitation; however finding and locating subsurface structures of this type may be difficult or even impossible with conventional seismic methods (Kleinberg, 2006). Electromagnetic methods maybe preferable to seismic methods because the resistivity contrast is highly sensitive to the concentration as well as the geometric distribution of hydrate.

High abundances of hydrate have significant implications for the global carbon cycle (Dickens, 2003). Perturbations of the stability conditions of hydrate could cause the catastrophic release of methane (a significant greenhouse gas), which may have contributed to past climate change (Kennett et al., 2003; Kvenvolden, 1993b). However, it is the chronic release of hydrate, currently taking place in Arctic regions, that is more likely to be a significant contributor to future climate change and has been associated with past climate change. For example, the carbon isotopic excursion at the end of the Paleocene is possibly from hydrate (Archer, 2007; Archer and Buffett, 2005; Dickens, 2001). Some studies also suggest that climate change will, in turn, affect hydrate deposits worldwide (Fyke and Weaver, 2006).

Immediate interest in gas hydrate arises from the potential geohazard posed by drilling into and through hydrate, and slope instability (Mienert et al., 2005; Nixon and Grozic, 2007), which may threaten seafloor infrastructure (Kven-

volden, 2000; Hovland and Gudmestad, 2001). As deep sea exploration becomes more common, the threat of drilling into hydrate sediments will become a more significant problem, because more drilling and production operations will be within the thermodynamic stability conditions for hydrate (Dawe and Thomas, 2007). Warm drilling fluids can cause pre-existing hydrate to dissociate; this can cause gas to build up and cause blow-outs of wells. Melted hydrate may also cause sediments to become loose slurries and provide little or no structural support, leading to tubing collapse or seafloor instability. Additional hazards while drilling may result from the formation of gas hydrate in the event of a kick – when hydrocarbon flows into the well bore from the reservoir – causing serious well safety, operational, and control problems (Ostergaard et al., 2000).

Slope failure due to hydrate dissociation has been implicated in the Storrega slide offshore Norway (Paull et al., 2007; Sultan et al., 2004) and may have released enough sediment to generate a tsunami (Smith et al., 2004). Similarly, hydrates are implicated as one of many possible factors for the Humboldt slide off the coast of California, where decaying gas hydrate released methane gas in the bubble phase, increasing the pore water pressure and decreasing the effective strength of the sediment, and thereby reducing the stability of the slope (Field and Barber, 1993).

A developing interest in hydrate is to use carbon dioxide ($CO_2$) hydrate as an aid to carbon sequestration in the deep oceans (Lee et al., 2003). Carbon dioxide would be injected into the sediments and the formation of $CO_2$ hydrate would create a natural barrier to the release of carbon dioxide stored beneath the hydrate (Lee et al., 2003). It will be necessary to develop long-term non-invasive monitoring techniques of hydrate formation during ocean carbon sequestration.

The economic and environmental uses for hydrate, and the geohazards

posed by it, all make mapping the extent and distribution of hydrate important.

### 1.2.3 Detection of Gas Hydrate

Traditionally, seismic methods are used to detect hydrate; a bottom simulating reflector (BSR) typically marks the phase change of solid hydrate above and free gas below the BSR (Shipley et al., 1979). The BSR runs parallel to the seafloor and often cross-cuts sedimentary structures. The depth to the BSR, and hence the thickness of the gas hydrate stability zone (GHSZ), is controlled by the intersection of the hydrate stability field with the local geothermal gradient. However, the BSR may not guarantee hydrate, as was observed on DSDP Leg 84 site 496 and site 596, where no hydrate was recovered and the presence of free gas created the BSR (Sloan, 1990 p. 424; Sloan and Koh, 2008 p. 575 ). Other types of seismic signatures have been noted at the Blake Ridge by Hornback et al. (2003) and Gorman et al. (2002), such as a fossil BSR, seismic blanking, and seismic bright spots. Unfortunately, the lack of any seismic signature does not rule out the existence of hydrate. For instance, hydrates have been known to occur in the Gulf of Mexico without a seismic BSR (Sloan, 1990). There are also cases when the sedimentary layering is parallel to the seafloor, creating ambiguity between a seismic BSR and a sedimentary reflection. While seismic methods are often able to detect the lower stratigraphic bound of hydrate, the diffuse upper bound is not well imaged and there is often no seismic reflectivity signature from within the hydrate region.

Other methods for hydrate detection include electrical resistivity measurements made during well logging, which indicate that regions containing hydrate are more resistive compared to water saturated zones (e.g. Collett and Ladd, 2000). Although this effect can be modest (e.g. ODP Leg 204 had resistivity well logs with a resistivity of 2.5 $\Omega$m for sediments containing hydrate and 1 $\Omega$m for background sediments (Shipboad Scientific Party, 2003d)), it provides a suitable

electromagnetic (EM) target for the detection of hydrates, since the EM response increases with an increase in hydrate volume fraction.

Well logging requires the presence of a well to provide only a point measurement of the hydrate distribution at a particular location. Multiple drilling is required to gain a regional scale distribution for hydrate, and even then there may be little correlation between wells. Drilling is expensive and also disturbs hydrate (Paull and Ussler, 2001) and so a technique to provide bulk *in situ* assessment of gas hydrate content is needed. Marine controlled-source electromagnetic (CSEM) methods are non-invasive techniques and can evaluate the bulk properties of hydrate over a much larger volume than well logging.

### 1.2.4 Resistivity of Gas Hydrate

Laboratory studies of the electrical conductivity of hydrate have been proposed by a number of academic groups and individuals: GHASTLI - Gas Hydrate and Sediment Test Laboratory Instrument (Winters et al., 2003); the Georgia Tech, IPTC - Instrumented Pressure Testing Chamber (Yun et al., 2006); National Oceanography Centre, Southampton UK (Ellis et al., 2006). However, no results from these studies have been yet reported and the resistivity of pure hydrate is not documented.

Zones containing gas hydrate are more resistive than the surrounding sediment, creating a contrast that is measurable with electromagnetic methods (Collett and Ladd, 2000). The resistivity of hydrate increases proportionally with an increase in hydrate concentration, providing a quantitative measure of the amount of hydrate, rather than the qualitative assessment given by sonic velocities (Pearson et al., 1983). The success of characterizing and quantifying hydrate concentrations accurately with electrical methods in the natural environment is dependent on understanding how the conductivity (or resistivity) of hydrate behaves in controlled

laboratory studies.

Knowledge of the electrical properties of hydrate comes from well logging in both permafrost and marine environments and from a handful of laboratory studies of structure II tetrahydrofuron (THF) hydrate, $CH_4$ hydrate and $CO_2$ hydrate, and ice (an analogue for hydrate) (Dvorkin et al., 2003; Pearson et al., 1986; Tzirita, 1992; Santamarina et al., 2004). Generally, electrical resistivity measurements made during laboratory studies are used to monitor the formation of hydrate rather than to actually measure its absolute electrical resistivity (Zatsepina and Buffett, 2002, 2001; Spangenberg et al., 2005).

Well logs provide only apparent resistivity measurements rather than the true resistivity of the hydrated sediment (Tzirita, 1992). Resistivities measured in well logs vary from region to region and are based on differences in sediments, hydrate distribution, and pore fluids. There are a few examples in the literature of resistivity studies on sediment cores of dissociating hydrate. In these cases the resistivity of the pore fluid before and after hydrate dissociation is the important parameter (e.g. Hyndman et al., 1999; Riedel et al., 2003; Francisca et al., 2005).

### 1.2.5 Relationship between Resistivity and Hydrate Concentration

In the absence of laboratory studies, the relationship between resistivity and hydrate concentration relies empirically on Archie's Law, commonly used in oil and gas exploration. Archie's Law (Archie, 1942), was developed from estimating water saturations in gas-oil-water-matrix systems (Archie, 1942) and has been used to obtain quantitative hydrate concentrations (Collett, 1998), as demonstrated in Collett and Ladd (2000) and ODP Leg 204 Initial Reports (Shipboard Scientific Party, 2003):

$$S_w = (aR_w/\varphi^m R_t)^{1/n}. \qquad (1.1)$$

Here $S_w$ is the water saturation (or fraction of water in a given pore space); $R_w$ is the resistivity of the formation water; $R_t$ is the formation resistivity; and $\varphi$ is the porosity of the sediments. The constants $a$, $m$ and $n$ are empirical parameters in Archie's equation and are typically $0.5 < a < 2.5$, $1.5 < m < 3$ and, $n \approx 2$ (Edwards, 2005; Archie, 1942). A hydrate saturation, $S_h$, is calculated using:

$$S_h = 1 - S_w \tag{1.2}$$

assuming that hydrate fills the remaining pore space. Archie's Law requires knowledge of the saturation exponent, $n$, which is dependent on pore shape, connectivity, constrictivity of the pore network, and distribution of the conducting phase (Spangenberg, 2001). Archie's Law is valid if hydrate is disseminated through the pore space, as hydrate will act to reduce the porosity (Hyndman et al., 1999). However, a massive gas hydrate occurrence will not be modeled correctly by simple mixing rules (Lee and Collett, 2001).

Our current relationships between hydrate concentration and resistivity are speculative because direct measurements of hydrate content in sediments are not presently available (Spangenberg, 2001; Hyndman et al., 1999), and field and laboratory calibration studies are lacking (Collett and Ladd, 2000; Collett, 1998). Depending on the geometric distribution of hydrate, Archie's Law may not be a representative model, especially if hydrate is found in veins and fractures. The extremal bounds for effective conductivity $\sigma$ are the Hashin Shtrikman bounds (HS-bounds) (Schmeling, 1986; Hashin and Shtrikman, 1963):

$$\sigma_{HS^-} = \sigma_0 + \zeta \left( \frac{1}{\sigma_f - \sigma_0} + \frac{1-\zeta}{3\sigma_0} \right)^{-1} \tag{1.3}$$

$$\sigma_{HS^+} = \sigma_f + (1-\zeta) \left( \frac{1}{\sigma_0 - \sigma_f} + \frac{\zeta}{3\sigma_f} \right)^{-1} \tag{1.4}$$

where $\zeta$ is the volumetric fraction of the fluid and $\sigma_0$ and $\sigma_f$ are the specific conductivities of the matrix solid and the fluid. Conductivity must lie somewhere

between these two bounds (and indeed Archie's Law does). The HS lower bound, $\sigma_{HS^-}$, corresponds to resistive spherical inclusions within a conductive matrix and the HS upper bound, $\sigma_{HS^+}$, corresponds to conductive spherical inclusions within a resistive matrix (Hashin and Shtrikman, 1963). In terms of hydrate, the HS lower bound may represent a low concentration of granular disseminated hydrate distributed in isolated spheres within the conductive sediment. For a higher concentration of hydrate, Archie's Law may be more appropriate. In clay-rich sediments hydrate may occur in veins or fractures and be better represented by the HS upper bound – where resistive material occurs in sheets impeding current flow through the matrix of fluid.

## 1.3 Goals of Dissertation

This thesis discusses an electromagnetic survey conducted at Hydrate Ridge about 80 km offshore from Newport, Oregon. This work is a first step to using EM for hydrate detection and for understanding the relationships between hydrate, gas, and fluid flow in the accretionary complex. 1D forward model studies of hydrates are discussed in Chapters 2 and 3 in order to explain the experimental design. The collection and processing of the data is discussed in Chapter 3, with preliminary interpretations shown as pseudosection results in Chapter 4. The Hydrate Ridge experiment demonstrated the importance of good navigation for the transmitter. A technique described in Chapter 5 uses near field electric and magnetic data to invert for transmitter and receiver geometries, allowing a 2D inversion of the data set as discussed in Chapters 6 and 7.

# 2

# Marine Controlled Source Electromagnetic Method

## 2.1 History

The marine electromagnetic (EM) methods, controlled source electromagnetic (CSEM) and magnetotelluric (MT) techniques, are sensitive to the electrical resistivity of the sediments and the formation porosity, permeability, and resistivity of the pore fluids. The marine CSEM technique was first developed in the academic world to explore mid-ocean ridges (MacGregor et al., 1998; Evans et al., 1994) and the oceanic lithosphere (Constable and Cox, 1996; Chave et al., 1991; Cox et al., 1986) and is becoming commonplace in industry to explore for hydrocarbons (Eidesmo et al., 2002; Hesthammer and Boulaenko, 2005; Ellingsrud et al., 2002). Implementation of CSEM to detect gas hydrates has shown great potential (Weitemeyer et al., 2006c; Schwalenberg et al., 2005; Yuan and Edwards, 2000) and the CSEM techniques' ability to detect this sometimes subtle electromagnetically resistive target is under active development.

The marine MT signal is the natural magnetic field generated in Earth's magnetosphere and ionosphere as a result of the interaction of the solar wind with the main geomagnetic field which produces local plane-wave electromagnetic energy in the frequency band of 0.0001 Hz - 10 Hz (Telford et al., 1998; Vozoff, 1991;

Key, 2003). In the marine MT method (Figure 2.1) seafloor recorders measure Earth's naturally time-varying magnetic field and induced electric fields. From these an electromagnetic impedance can be computed and in turn large-scale geologic structure involving resistivity contrasts can be imaged.

The CSEM method developed from academic research to replace the high frequency MT signals lost at the deep seafloor due to attenuation in the thick water column and to study the upper oceanic lithosphere (Cox et al., 1986; Flosadóttir and Constable, 1996; Constable, 1990). Prior to the advent of the broadband magnetotelluric instrument (Constable et al., 1998) only the CSEM technique could be used to study the upper oceanic lithosphere, as MT studies were limited to frequencies lower than 0.0001 Hz and imaging only deep mantle structure (Constable, 1990). Today the broadband MT instrument is capable of imaging crustal depths as shallow as a few hundred meters as well as deep mantle structures, overlapping with CSEM measurements to some extent. Generally speaking, the CSEM method images shallower structure and is sensitive to more resistive parts of the seafloor, while MT is sensitive to more conductive and deeper features.

The CSEM method used in this thesis was developed at Scripps Institution of Oceanography over the past thirty years and is a frequency-domain technique whereby a horizontal electric dipole transmitter is towed on or close to the seafloor and receivers record the transmitted fields at various frequencies and ranges (Constable and Cox, 1996). The marine CSEM method (Figure 2.1) uses the same seafloor recorders as the MT method. Electric fields recorded at receivers are larger over resistive seafloor structures such as basalt, salt, carbonates, hydrocarbon reservoirs, or gas hydrates (Constable, 2006).

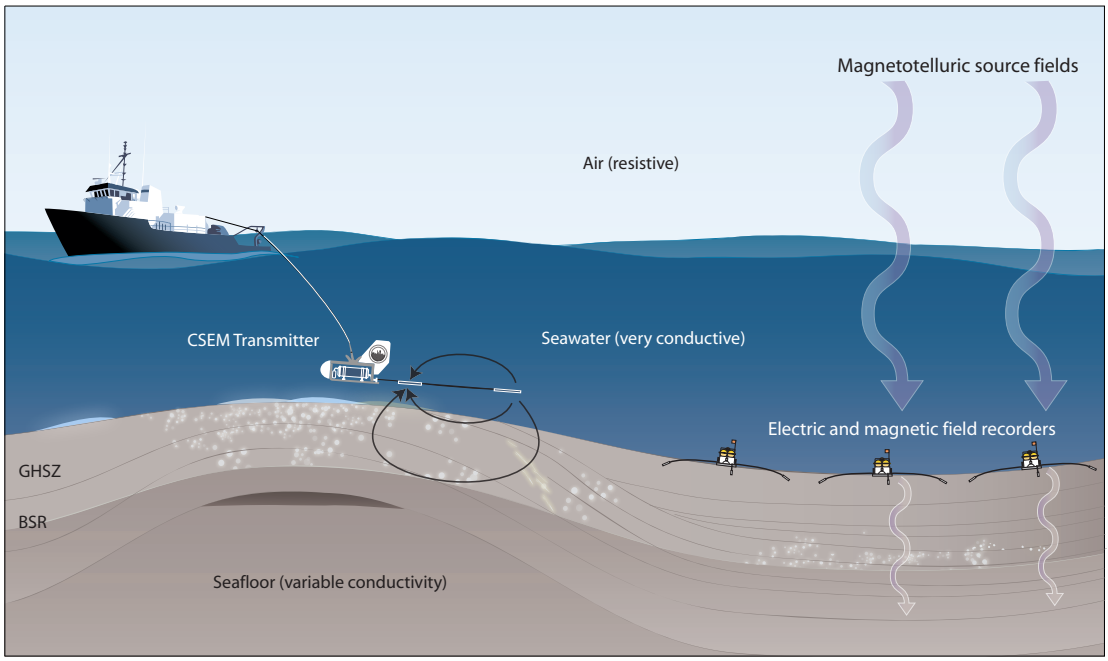


**Figure 2.1**: For CSEM surveys, an electric dipole transmitter is towed above the seafloor (about 100 m) and an alternating electromagnetic field is transmitted along the antenna, which can be 50 m to 200 m long. Seafloor receivers record the electric fields (and magnetic fields) from the transmitter. For the magnetotelluric (MT) method the same seafloor receivers can be used to record Earth's time-varying magnetic fields along with induced electric fields. From these an electromagnetic impedance can be computed and in turn large-scale geologic structure imaged. BSR – bottom simulating reflector, GHSZ – gas hydrate stability zone. The gas hydrate stability zone thickness is controlled by the intersection of the geothermal gradient with the gas hydrate stability field (modified from Weitemeyer et al. (2006b)).

### 2.1.1 CSEM to Detect Gas Hydrates

The application of CSEM methods to hydrate detection was first considered by Edwards (1997). He modeled the transient electric dipole-dipole method as a means of estimating hydrate volume and argued for the usefulness of EM methods in augmenting drilling and seismic techniques. Field studies conducted at the Northern Cascadia margin off the west coast of British Columbia, Canada, demonstrated the merits of CSEM by showing the existence of hydrate when no BSR is present (Yuan and Edwards, 2000), and the existence of hydrate or free gas

in seismic blank zones thought to represent hydrate bearing pipes (Schwalenberg et al., 2005).

The system employed at Northern Cascadia was a towed horizontal electric dipole-dipole array (Edwards and Chave, 1986), made up of a transmitter dipole and reciever dipoles attached at fixed offsets behind the transmitter (Yuan and Edwards, 2000). The time-domain system operates by producing a pulse of EM energy and then measuring the diffusion time through the seabed (Cheesman et al., 1986). The traveltime is related linearly to the resisitivity: the higher the resistivity, the shorter the traveltime (Yuan and Edwards, 2000). The electric dipole-dipole technique was selected because of its sensitivity to intermediate resisitive crustal zones (top 200 m). Hyndman et al. (1999) claim it is useful if lateral resistivity changes in sediments are small compared to the lateral changes in hydrate resistivity.

A similar towed system, based upon the Geological Survey of Canada's magnetic dipole system, has been used in the Gulf of Mexico as a mapping tool to image hydrate mounds (Evans, 2007). It is a frequency-domain towed magnetic dipole system that generates harmonic magnetic fields over a range of frequencies (Hz to kHz) which are recorded by three receivers, each tuned to a specific frequency and towed at a fixed distance behind the transmitter. It is designed to image very shallow sediments – the top 20 m. The survey conducted at Atwater Valley hydrate mound showed raised porosity (conductivity) as a result of high pore fluid temperatures and salinity beneath the mound (Evans, 2007).

Since Evans' (2007) EM system is only capable of imaging the top 20 m of sediment, the rest of the hydrate stability zone goes unmapped using this instrumentation. Edwards' (1997) EM method images the gas hydrate stability zone but is depth-limited by the separation distance of the bipole array. Both lack the abil-

ity to image the source of fluid and methane flow migrating into the gas hydrate stability zone. In addition, both methods are mapping tools dragged along the seafloor, limiting their use to undeveloped sedimentary basins. The receivers are at fixed geometries and thus are only capable of recording a radial mode (source and receiver are in-line) component of the 3D vector field. This limits resolution and the ability to detect and characterize anistropy or 3D structures. Their data are generally interpreted by only considering 1-D inversions to obtain simple surface resistivity maps.

Two other studies utilizing electromagnetic methods include a towed DC resistivity survey conducted in the Japan Sea (Goto et al., 2008) and a planned survey at the hydrate observatory site, Mississippi Canyon 118 (Dunbar, 2008). In the Japanese study locations of higher resistivity are claimed to be associated with hydrate, although these also appear to correlate with bathymetric effects. The range in resistivities (from 0.3 to 0.8 $\Omega$m) is very small and not suggestive of the significant concentration of hydrate which is expected from the recovery of a massive hydrate sample during the same experiment. The Mississippi Canyon 118 study is scheduled to take place later in 2008.

The Scripps CSEM transmitter system is deep-towed 50–100 m above the seafloor, making it possible to operate in regions with seafloor infrastructure. Because receivers are autonomous almost any geometric arrangement between source and receiver is possible. In addition, all components of the electromagnetic field (i.e. $E_{x,y,z}$ and $B_{x,y}$) are recorded, providing a rich data set compared to the collection a single in-line component. However, navigation of the transmitter becomes very important, unlike the tandem towed systems of Evans and Edwards (above) which are at fixed and known positions.

## 2.2 Principles of CSEM

### 2.2.1 Mathematical Governing Equations

The physics of CSEM is represented by Maxwell's equations (following Griffiths (1999) and Ward and Hohmann (1987)) which govern the four vector functions: the electric field, $\mathbf{E}$ (V/m), the magnetic induction, $\mathbf{B}$ (T), the dielectric displacement, $\mathbf{D}$ (C/m$^2$), and the magnetic field $\mathbf{H}$ (A/m) :

$$\nabla \cdot \mathbf{D} = q, \tag{2.1}$$

$$\nabla \cdot \mathbf{B} = 0, \tag{2.2}$$

$$\nabla \times \mathbf{E} = -\frac{\partial \mathbf{B}}{\partial t}, \tag{2.3}$$

$$\nabla \times \mathbf{H} = \mathbf{J} + \frac{\partial \mathbf{D}}{\partial t}, \tag{2.4}$$

where $q$ is charge density (C/m$^3$), $\mathbf{J}$ is current density (A/m$^2$), $t$ is time (s) and the operator $\nabla$ is the spatial gradient $(\frac{\partial}{\partial x}, \frac{\partial}{\partial y}, \frac{\partial}{\partial z})$. Equation 2.1 is Gauss's Law: the flux through any surface enclosing a given charge will be the same. Equation 2.2 states that the divergence of the magnetic field is zero. Equation 2.3 is Faraday's Law: a changing magnetic field induces an electric field. The last equation, Equation 2.4, is Ampere's Law, which states that the current enclosed by an Amperian loop will generate a magnetic field, and a moving charge induces a magnetic field. The Maxwell equations are coupled by the constitutive relations:

$$\mathbf{D} = \epsilon \mathbf{E}, \tag{2.5}$$

$$\mathbf{B} = \mu \mathbf{H}, \tag{2.6}$$

$$\mathbf{J} = \sigma \mathbf{E}, \tag{2.7}$$

where $\epsilon$, $\mu$, and $\sigma$ are respectively the dielectric permittivity, the magnetic permeability, and the electrical conductivity (the reciprocal of resistivity, $\rho$). To simplify the electromagnetic problem the magnetic permeability is assumed to be that of

free space $\mu_o$=4$\pi$ $\times 10^{-7}$N/A$^2$ (a valid approximation for non-ferromagnetic materials (Stratton, 1941)), so constitutive relation, Equation 2.6 becomes:

$$\mathbf{B} = \mu_o \mathbf{H}. \quad (2.8)$$

In the CSEM problems the transmitter is an additional source term, $\mathbf{J_s}$, and so equation 2.7 is re-written as:

$$\mathbf{J} = \sigma \mathbf{E} + \mathbf{J}_s. \quad (2.9)$$

The displacement term in Maxwell's Equations 2.1 and 2.4 can be replaced by constitutive relation, Equation 2.5, to yield:

$$\nabla \cdot \mathbf{E} = \frac{q}{\epsilon} \quad (2.10)$$

$$\nabla \times \mathbf{H} = \epsilon \frac{\partial E}{\partial t} + \mathbf{J}. \quad (2.11)$$

The quasi-stationary approximation for Maxwell's equations can be used since the frequencies considered in marine electromagnetics methods are very low (less than kHz) which eliminates the displacement term: $\epsilon \frac{\partial E}{\partial t}$. This removal of the displacement term also allows Maxwell's equations be well approximated by the diffusion equation rather than the wave equation (Løseth et al., 2006). Assuming a harmonic time variation of $e^{-i\omega t}$ for the electric and magnetic fields, where $i = \sqrt{-1}$ and $\omega$ is the angular frequency ($\omega$=2$\pi f$, $f$ is frequency), by substituting constitutive relation 2.8 into 2.3, and including the source term, $\mathbf{J_s}$, the governing Equations 2.3 and 2.11 become:

$$\nabla \times \mathbf{E} = i\mu_o \omega \mathbf{H} \quad (2.12)$$

$$\nabla \times \mathbf{H} - \sigma \mathbf{E} = \mathbf{J}_s. \quad (2.13)$$

### 2.2.2 Physical Behavior

In electromagnetic methods there are two phenomena related to a changing electric field: a galvanic effect and an inductive effect. A galvanic effect is

associated with surface charges as in DC resistivity surveying. An inductive effect is a result of an electromotive force that is generated by a change in current flow that induces a magnetic field and in turn induces a secondary electric field in the body (e.g. Equations 2.3 and 2.4). Galvanic techniques rely on geometry for depth penetration whereas inductive techniques rely on both geometry and frequencies to determine depth. Inductive, plane wave EM fields will attenuate as they propagate away from the source in a uniform conductive medium. At a distance $\delta$ field strengths are reduced by a factor of $1/e$; this is also called the "skin depth" (Ward and Hohmann, 1987):

$$\delta = (\rho/\pi f \mu_o) \approx 500\sqrt{\rho/f}. \qquad (2.14)$$

The skin depth is dependent on the resistivity of the medium and on the frequency of the source field. In the case of CSEM methods a transmitter 100 m above the seafloor is almost one skin depth away from the seafloor for a transmission frequency of 5 Hz. The skin depths for the various frequencies considered for the hydrate project are shown in Table 2.1.

**Table 2.1**: Attenuation of the EM fields in seawater (0.3 Ωm) and sediment (1 Ωm) for different frequencies

| Frequency (Hz) | 0.1 | 1 | 5 | 15 | 25 | 35 | 100 |
|---|---|---|---|---|---|---|---|
| $\delta_{seawater}$ (m) | 866.0 | 273.9 | 122.5 | 70.7 | 54.8 | 46.3 | 27.4 |
| $\delta_{sediment}$(m) | 1581.1 | 500 | 223.6 | 129.1 | 100.0 | 84.5 | 50 |

## 2.3 Modes

There are two end-member transmitter and receiver orientations: radial (in-line), and azimuthal (broadside or cross-line), as shown in Figure 2.2. For the radial mode ($\phi = 0°$, $180°$, where $\phi$ is the angle between the direction of the transmitter antenna and the source-receiver vector) the azimuthal component of the electric field $E_\phi$ goes to zero, and for the azimuthal mode ($\phi = 90°$, $270°$) the radial component of the electric field $E_\rho$ goes to zero. At azimuths in between

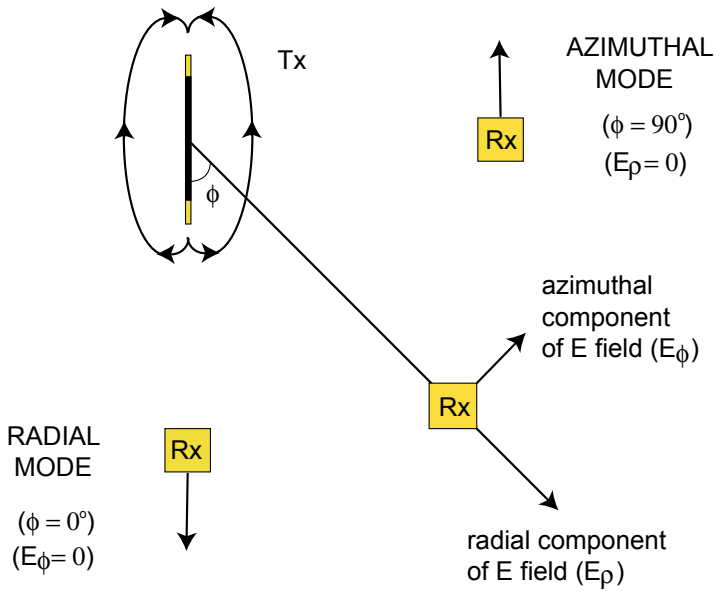


**Figure 2.2**: A plane view of transmitter and receiver geometries outlining the two modes: radial and azimuthal. Figure is taken from Behrens (2005). Tx is transmitter and Rx is receiver.

the two end-member cases the horizontal fields are composed of both an azimuthal and a radial component.

## 2.4 Polarization Ellipses

The pure radial and azimuthal modes of the horizontal electric fields are rarely observed by seafloor instruments; more commonly the combination of these two end-member cases is recorded. To eliminate some uncertainty in the source-receiver geometry one can look at CSEM data in terms of polarization ellipse parameters (Smith and Ward, 1974). The two orthogonal horizontal electric field measurements, $E_1 = |E_1|\mathrm{e}^{i\theta_1}$ and $E_2 = |E_2|\mathrm{e}^{i\theta_2}$, with magnitudes $|E_1|$ and $|E_2|$ and phases $\theta_1$ and $\theta_2$ are combined in terms of the major ($P_{max}$) and minor ($P_{min}$), axes of the polarization ellipse (Figure 2.3):

$$P_{max} = ||E_1|e^{i\triangle\theta}\sin\alpha + |E_2|\cos\alpha| \qquad (2.15)$$

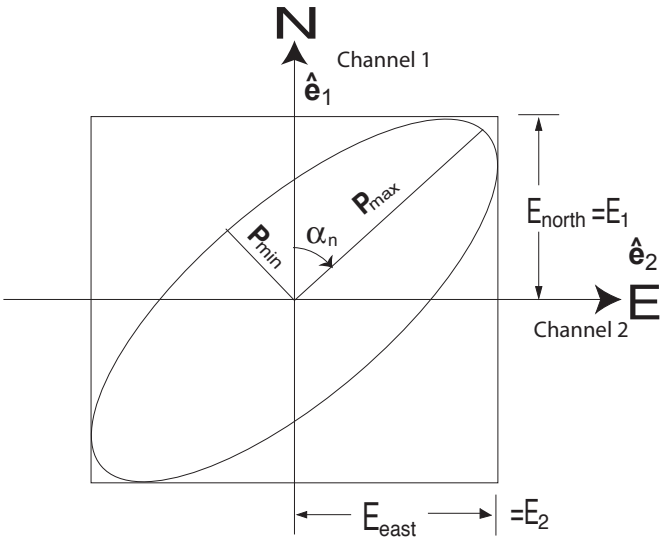


**Figure 2.3**: The horizontal electric field polarization ellipse parameters consists of major and minor axes and is oriented an angle $\alpha_n$ = 90-$\alpha$ from channel 1 $\hat{\mathbf{e}}_\mathbf{1}$. Figure modified from Behrens (2005).

$$P_{min} = ||E_1|e^{i\triangle\theta}\cos\alpha + |E_2|\sin\alpha| \qquad (2.16)$$

where $\triangle\theta = \theta_1 - \theta_2$, with $P_{max}$ oriented at a tilt angle $\alpha$ counterclockwise from channel 2 ($\hat{\mathbf{e}}_\mathbf{2}$ in Figure 2.3) and $\alpha$ given by:

$$\tan 2\alpha = \frac{2|E_2||E_1|\cos\triangle\theta}{|E_2|^2 - |E_1|^2} \qquad (2.17)$$

and geographic orientation $\alpha_N$ is 90° - $\alpha$.

The first analysis of the Hydrate Ridge experiment used $P_{max}$. $P_{max}$ is the largest component of the field data and is insensitive to receiver orientation and less sensitive to transmitter azimuth than the individual cartesian components ($x$ and $y$ ) (Flosadóttir and Constable, 1996). Furthermore, because $P_{max}$ uses relative phase, the absolute phase of the transmitter does not need to be known (Behrens, 2005). While this works well for 1D modeling, much information has been suppressed, and we shall need to take a different approach when we move to 2D modeling in Chapters 6 and 7.

## 2.5 1D Forward Modeling

Forward modeling is an important component of marine electromagnetic methods, especially for experimental design of a field survey where it is used to determine the sensitivity of a target to frequency and source-receiver geometry. There are several numerical modeling codes available in 1D and 2D (2D modeling is discussed in Chapter 7).

The speed and ease of 1D modeling allows for many range and frequency combinations to be computed in order to find an optimal survey design (Constable and Weiss, 2006). The 1-D forward modeling code used for the analysis presented in Chapters 3 and 4 is that of Flosadóttir and Constable (1996), developed from the work of Chave and Cox (1982). Chave and Cox (1982) decompose the vector fields in Maxwell's equations into a combination of three scalar fields in a cylindrical coordinate system and numerically solved the radial, azimuthal, and vertical components of the horizontal electric fields using a Fast Hankel transform (e.g. Anderson (1979, 1989)) or by a method of Gaussian quadrature over Bessel functions developed by Chave (1983) (Flosadóttir and Constable, 1996).

A newer 1D forward modeling code developed by Key (submitted) uses a Lorentz-gauged vector potential formulation of Maxwell's equations and solves these in a cartesian coordinate system. This allows for modeling of dipping and rotated transmitters which are more realistic in practice. This code was available for the later work in Chapter 5 to model the transmitter geometry using the short range electromagnetic fields recorded at the receivers.

# 3

# Hydrate Ridge Experiment

## 3.1 Hydrate Ridge Geology

Hydrate Ridge is located on the accretionary complex where the Juan de Fuca plate subducts obliquely (N69°E) beneath the North American plate at a rate of 42 mm/yr (MacKay et al., 1992; DeMets et al., 1990) (Figure 3.1). This region is also called the Cascadia subduction zone. The subducting plate's thick sediment cover – 3 to 4 km of sandy and silty turbidites – is accreted to North America by offscraping at the deformation front or by underplating beneath the accretionary complex which occurs tens of kilometers east of the deformation front, creating an extensive fold and thrust belt on the continental slope (Tréhu et al., 2006; Tréhu and Flueh, 2001). One of the resulting ridges is a 25 km long by 15 km wide feature called Hydrate Ridge, a north-south trending peanut-shaped structure, approximately 80 km offshore Newport, Oregon (Tréhu et al., 2004). It is located where the dominant direction of thrusting at the deformation front undergoes a transition from landward vergence to the north to seaward vergence to the south (Tréhu et al., 2006; MacKay et al., 1992).

Evidence for hydrate comes from the bottom simulating reflector (BSR) present over much of Hydrate Ridge (Tréhu et al., 1999; Tréhu and Flueh, 2001), recovered samples of massive hydrate (Tréhu and Flueh, 2001; Bohrmann et al.,

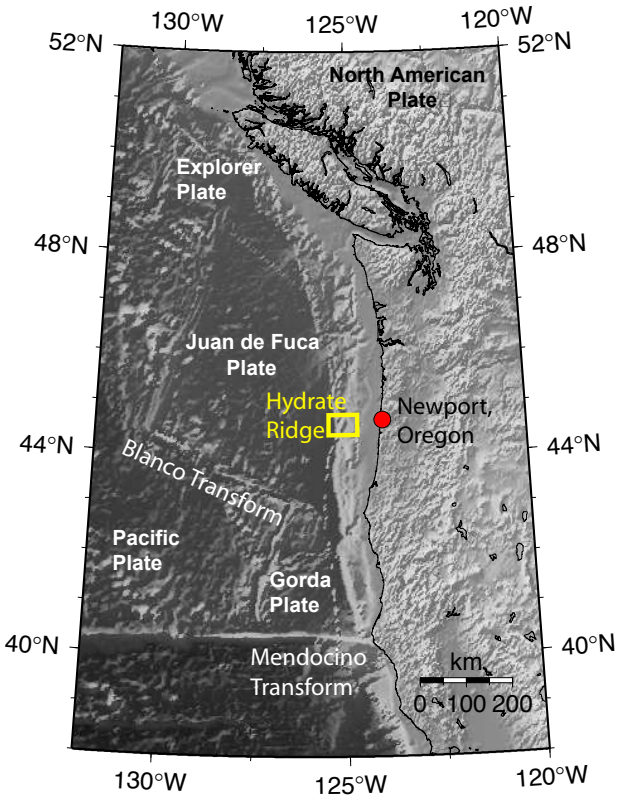


**Figure 3.1**: Hydrate Ridge is located on the accretionary complex where the Juan de Fuca plate subducts beneath the North American plate, approximately 80 km off shore from Newport, Oregon.

1998), as well as logs and cores from Ocean Drilling Program (ODP) Leg 204 (Tréhu et al., 2006). The ODP Leg 204 drilling and 3D seismic data provide information about the distribution of hydrate that may be used to develop useful CSEM forward model studies necessary for the experimental design of the Hydrate Ridge EM survey.

## 3.2 1D Hydrate Models

The 1D models presented here are based on Ocean Drilling Program Leg 204 resistivity well logs. Well logs showed a background resistivity at Hydrate

Ridge of about 1 Ωm, and that sediments containing hydrate vary between 2 and 6 Ωm; 2 Ωm was conservatively used as the resistivity for hydrate containing sediment in the model studies. According to ODP Leg 204 Initial Reports, the hydrate distribution north of the southern summit begins at 45 meters below seafloor (mbsf), which is used as the starting depth for the hydrate layer in the model studies. The thickness of the hydrate layer comes from the seismic BSR depth, about 150 mbsf. A water depth of 1200 m was originally used, however later models were computed with an average water depth of 910 m for Hydrate Ridge. This should have little effect on the model results.

Using the 1D code of Flosadóttir and Constable (1996) it was found that the azimuthal mode has very little sensitivity to a hydrate layer and that the radial mode is most sensitive to such a layer. A suite of frequencies (0.1 to 300 Hz) and ranges (0 to 4000 m) were explored to determine the largest signal from the hydrate layer. Figure 3.2 is a shaded anomaly plot of frequency versus range. The contours are electric field amplitude and the color scale is the ratio of the two models: hydrate layer to a background sediment of 1 Ωm.

The largest normalized response from hydrate occurs at ranges and frequencies to the right of the thick white line at $10^{-15}$ V/Am$^2$, which is the instrument system noise floor. Despite this, a large hydrate signal is detectable at high frequencies ($> 10$ Hz) and short ranges ($< 2000$ m), to the left of the noise floor. However, the electric fields attenuate very quickly at these high frequencies and navigation of the transmitter becomes very important at these ranges and the range window of detection is much narrower.

In general, high frequencies and short ranges are best for distinguishing the top of hydrate, whereas lower frequencies and longer ranges will discriminate the bottom of hydrate. An increase in hydrate concentration will be reflected by

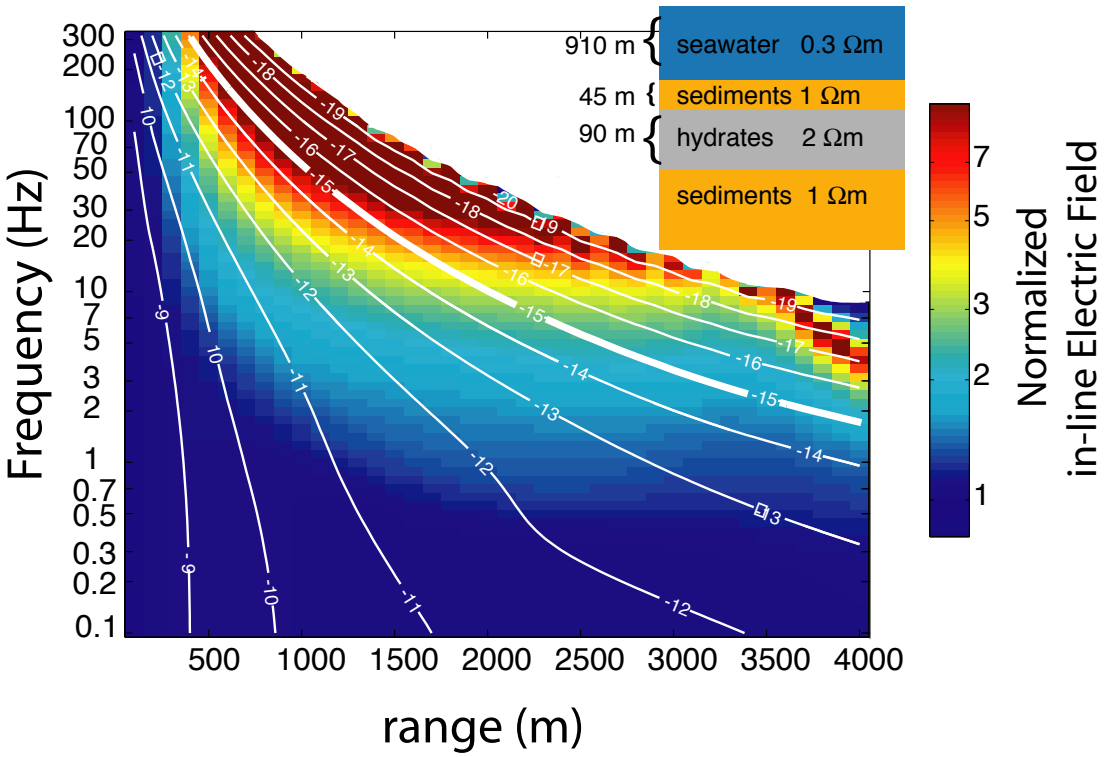


**Figure 3.2**: Electric field as a function of frequency and range for the hydrate model. Contours are $\log_{10}$ electric field values in V/Am$^2$. Shading shows the electric fields of the hydrate model normalized by the electric fields of the half space response (no-hydrate). The system noise floor is the thick white line at $10^{-15}$ V/Am$^2$ (from Weitemeyer et al. (2006b)).

a larger electromagnetic signal across all frequencies and ranges. There is a trade off between the large signal from hydrate observed at high frequencies and short ranges, and the subtler signal observed at longer ranges and at lower frequencies. Ideally, we want to use a wide frequency spectrum and collect data over a wide window of ranges to detect all aspects of the hydrate response. This can be partly accomplished by transmitting a square wave with a fundamental frequency that has sensitivity to the base of the hydrate layer. The square wave transmission allows for the odd harmonics to be processed to obtain the higher frequencies sensitive to shallower structure. For Hydrate Ridge, choosing 5 Hz as a fundamental transmission frequency means the detection hydrate is possible out to a range of

about 3000 m, and the odd harmonics of 15, 25 and 35 Hz provide detection of the larger signal from hydrate at shorter ranges (< 1700 m).

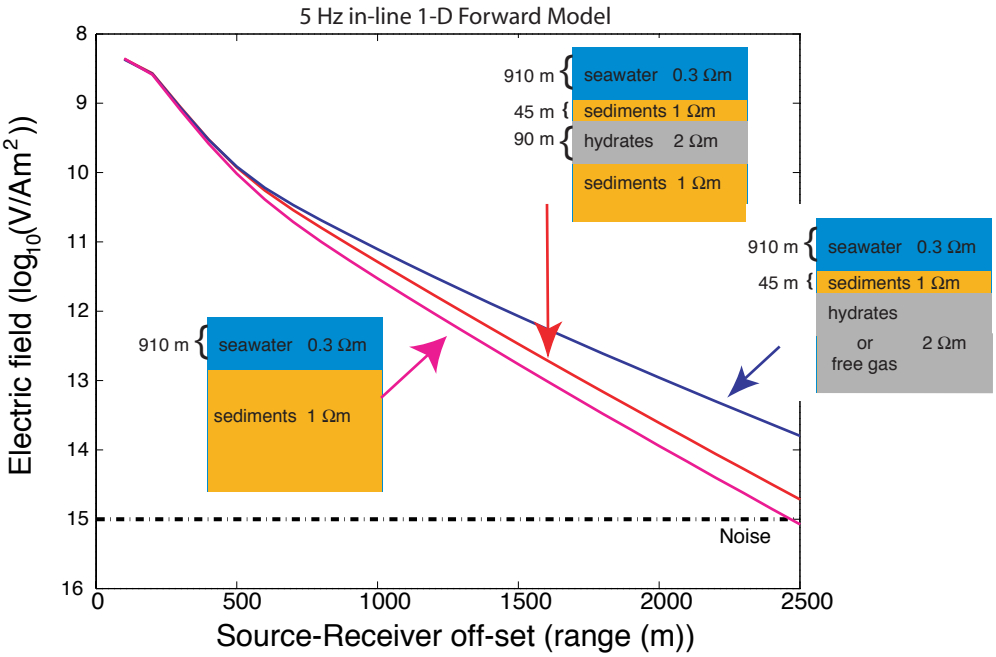


**Figure 3.3**: In-line electric field attenuation for three resistivity models: uniform sediments, a thin hydrate layer, and a thick hydrate layer at a frequency of 5 Hz (modified from Weitemeyer et al. (2006b)).

A horizontal slice along the 5 Hz frequency-range space in Figure 3.3 allows one to plot the electric field amplitude versus range, a typical way of looking at CSEM data. This is shown in Figure 3.3 for three models: sediment, a thin hydrate layer, and a thick hydrate layer. Each model response has a different electric field attenuation as the source-receiver range increases. The largest signal comes from the thick hydrate layer, while the weakest signal is from the sediment half-space. The model study demonstrates that the CSEM method is sensitive the existence and thickness of the modeled hydrate layer.

Another sensitivity analysis was conducted to test the ability of CSEM

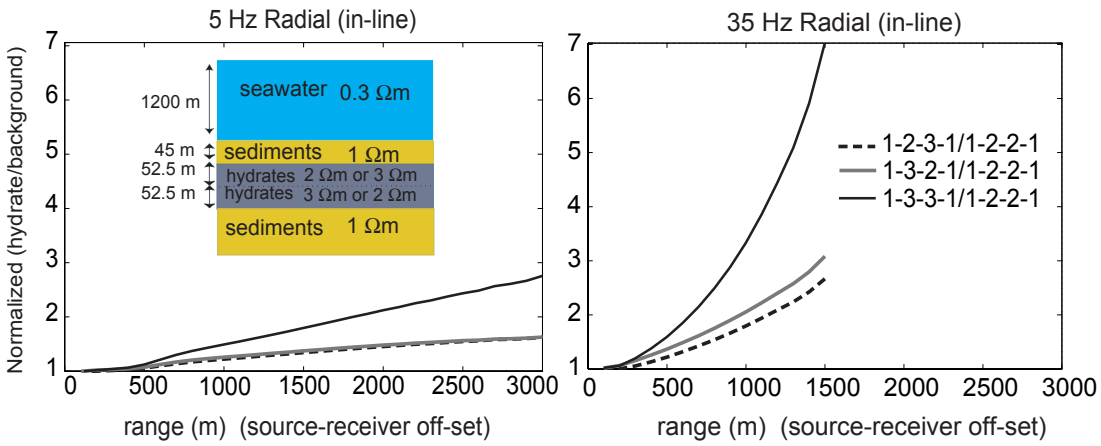


**Figure 3.4**: Normalized radial electric fields are sensitive to different resistivities of hydrate distributed in layers as shown for both 5 Hz (left) and 35 Hz (right). The top and bottom hydrate layer resistivities are toggled from 2 to 3 Ωm and are then normalized by a single hydrate layer of 2 Ωm of equivalent thickness. The label 1-2-3-1/1-2-2-1 refers to each layer's resistivity normalized by the single hydrate layer with resistivity 2 Ωm

techniques to distinguish two different layers of hydrate, one below the other, with different resistivities due to differing concentrations of hydrate (Figure 3.4). The layers are each swapped between 2 and 3 Ωm generating four possible hydrate layer models: a) 1-2-2-1, b) 1-2-3-1, c) 1-3-2-1, and d) 1-3-3-1; each number indicating the resistivity of the overburden sediment, hydrate 1, hydrate 2, and underlying sediment layers. Surprisingly, the 1-3-2-1 and 1-2-3-1 models are distinguishable at high frequencies. The uncertainty of this distinction between the 35 Hz 1-3-2-1 and 1-2-3-1 models requires the source-receiver off-set be known to within 50 m or less at a range of 1500 m. This suggests that CSEM methods can distinguish the diffuse upper hydrate region from a more concentrated hydrate region at the BSR.

These simple models provide important information for the collection of CSEM data at Hydrate Ridge. With a 5 Hz in-line transmission at ranges $< 3$ km, we should get good sensitivity to the hydrate. The data collection and processing is discussed in the following sections.

## 3.3 Experimental Layout

The Hydrate Ridge Experiment (HyREX'04) conducted in August 2004 resulted from an opportunistic use of shiptime aboard the R.V. New Horizon as it transited from San Diego, California to Newport, Oregon for another project. A marine electromagnetic experiment to image shallow gas hydrates was conducted successfully at Hydrate Ridge with only 3 days available on station for operation. The experimental layout shown in Figure 3.5 consisted of a single east-west line of 25 ocean bottom electromagnetic receivers spaced 600 m apart and two controlled source electromagnetic (CSEM) tow lines. One tow was over the top of the recievers (CSEM Tow 1) to get radial data and another tow was about 2 km to the north of the recievers (CSEM Tow 2) to get azimuthal data. A test of a new marine EM technique, controlled source magnetotelluric sounding (CSMT) was conducted and consisted of towing the transmitter at the surface of the ocean around Northern Hydrate Ridge (CSMT Tow). The receivers and CSEM Tow 1 are co-located with the Ocean Drilling Program (ODP) Leg 204 drill sites 1245, 1246, 1244, and 1252 and seismic line 230, intended to provide ground truth for the EM results. In addition to the CSEM data, about half of the receivers deployed had magnetometer sensors and so also recorded Earth's natural time varying magnetotelluric (MT) signal during the experiment.

During CSEM Tow 1 the transmitter, called Scripps Undersea Electromagnetic Source Instrument (SUESI) and shown in Figure 3.6, was flown approximately 100 m above the seafloor and transmitted a 100 A, 5 Hz square wave along a 90 m dipole antenna. The current was turned up to 200 A for CSEM Tow 2. For CSMT Tow the 90 m antenna was swapped for a 200 m antenna and the transmitter was towed a few meters below the sea's surface with a 100-200 A square wave of 0.1 Hz to mimic the higher frequency natural MT signal.

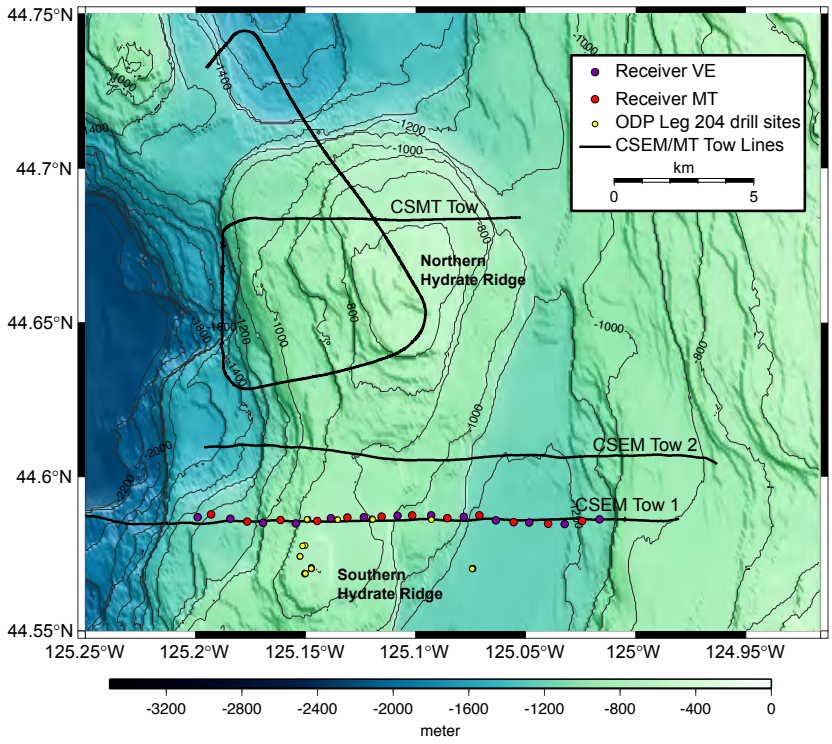


**Figure 3.5**: Electromagnetic experimental survey conducted at Hydrate Ridge utilized two different receiver configurations: a vertical electric field (VE) receiver and a magnetotelluric (MT) receiver. Three different tows occurred in-line with the 25 deployed receivers – CSEM Tow 1– collocated with ODP Leg 204 drill sites, a tow 2 km to the north of the receiver line – CSEM Tow 2 – and a surface towed transmission –CSMT tow – which is a loop tow further to the north. The bathymetry data is ETOPO2v2c from the National Geophysical Data Center.

An attempt was made to tow a dipole array in tandem behind the transmitter with a recording device. Unfortunately, the receiver flooded as a result of a missing o-ring and so no data was recovered. Aside from this error the towed receiver array appeared to work well physically and mechanically with no loss of equipment, despite the fact that it appeared to have been dragged along the bottom as evidenced by the presence of mud on the tandem receiver.

This thesis only discusses results from CSEM Tow 1 and briefly mentions the MT results. This is mainly because no more information about hydrate is

provided by the azimuthal tow (CSEM Tow 2) and the CSMT Tow was a test of the CSMT technique unrelated to detection of gas hydrates.

## 3.4 Data Acquisition

### 3.4.1 Transmitter

The transmitter used is a horizontal electromagnetic source similar to that described in Constable and Cox (1996), capable of a 200 A transmission – a moderate current output considering that now SIO has a transmitter capable of 500 A, and industry commonly transmits 1000 A when collecting CSEM data. Nevertheless, this is a sufficient current for shallow hydrate imaging (top 100s

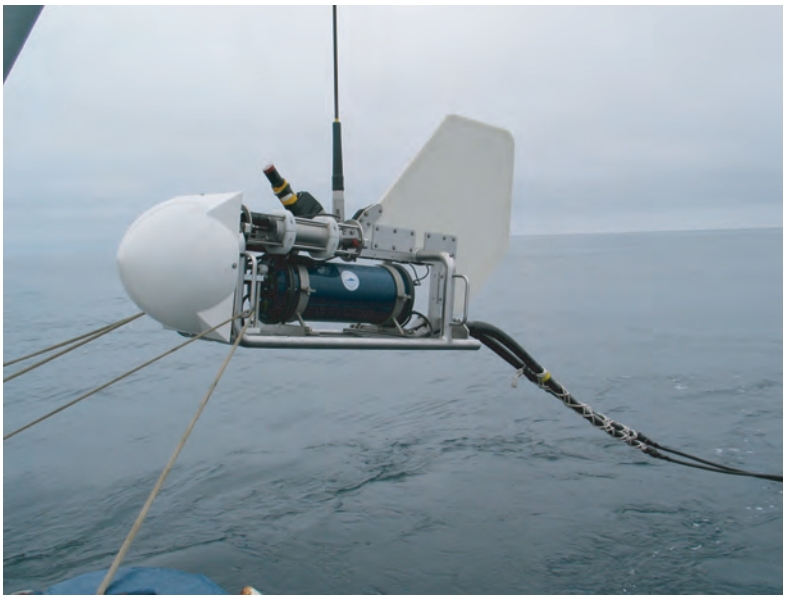

**Figure 3.6**: Deployment of the transmitter at Hydrate Ridge.

of meters) compared to the deeper targets (1000s of meters) for which CSEM technology has been commonly used. A low current is preferred as the higher currents may saturate the instrument amplifiers at close ranges where the electric fields are most sensitive to the hydrate. The electric dipole moment ($\mathbf{p}$) of the transmitter is dependent on the separation distance, $\mathbf{r}$, of the two copper pipes

**Figure 3.7**: Control unit for SUESI (left), *LabView* GUI for SUESI, *Fledermaus* bathymetry visualization and control unit for acoustic ranging (center), and a close up of the *LabView GUI* (right)

(electrodes) that alternate between positive and negative current, $I$. The dipole moment is given as $\mathbf{p} = I\mathbf{r}$. The Fourier series representation of a square wave is:

$$F(t) = \mathbf{p}\frac{4}{\pi}(\sin\omega t + \frac{\sin 3\omega t}{3} + \frac{\sin 5\omega t}{5} + ...) \qquad (3.1)$$

where $\omega = 2\pi f$ is the angular frequency ($f$ is frequency).

The dipole moment for CSEM Tow 1 was 1.15 kAm, for CSEM Tow 2 was 2.29 kAm, and for CSMT Tow ranged from 2.55 kAm to 5.09 kAm. A transmission of a 5 Hz square wave was used based on a compromise between the larger hydrate signal at higher frequencies and the accuracy of the transmitter navigation required for higher frequencies.

The transmitter was deep-towed approximately 100 m above the seafloor at the end of coaxial 0.680" cable that is used to power the transmitter and for telemetry between the transmitter and the shipboard control console. A standalone AC power source, located in the lab, takes shipboard 60 Hz three phase power and transforms it up to 2000 V, which is then transmitted down the tow cable (at 400 Hz) with telemetry. Once the power reaches the transmitter it is transformed down to about 100 V, and internal control circuitry, a set of rectifiers, and bipolar transistors are used to generate a square wave with a lower frequency

envelope. A display system of the environmental parameters (internal temperatures, current, navigational sensors) of the transmitter and topside control unit are shown in Figure 3.7. The left panel of Figure 3.7 shows the current and voltage control on the power source, a global positioning system (GPS) to monitor and keep time of the transmitter, and the control computer. The middle panel displays the environmental parameters of the transmitter, a *Fledermaus* view of the local bathymetry, and a computer controlling the acoustic ranging to receivers and the transmitter. The right panel is a close up of the of the *LabView* GUI displaying the transmitter environmental parameters such as transformer temperatures, the depth and altitude of the transmitter, and output current.

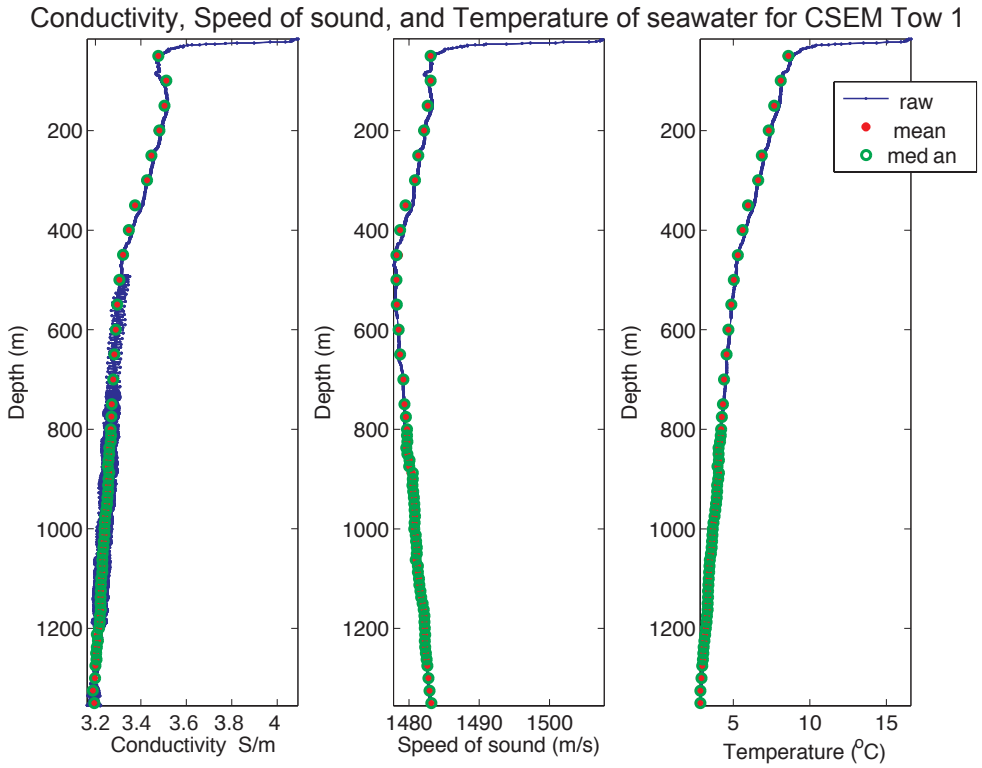


**Figure 3.8**: Conductivity, temperature and sound velocity of water column recorded by the *Valeport* while SUESI is deployed.

SUESI is equipped with a *Paroscientific Inc.* depth sensor, a *Valeport*

*Limited* CTD (conductivity, temperature, depth sensor and sound velocity meter), an altimeter, and an acoustic transponder. These sensors and acoustic ranges from the ship to the transmitter aid in locating the position of the transmitter as a function of time. The *Valeport* allows for an accurate conductivity, velocity, and temperature profile of the seawater as the transmitter is lowered to its tow depth shown in Figure 3.8. The seawater conductivity profile is used in Chapter 7 for inversion of the CSEM data.

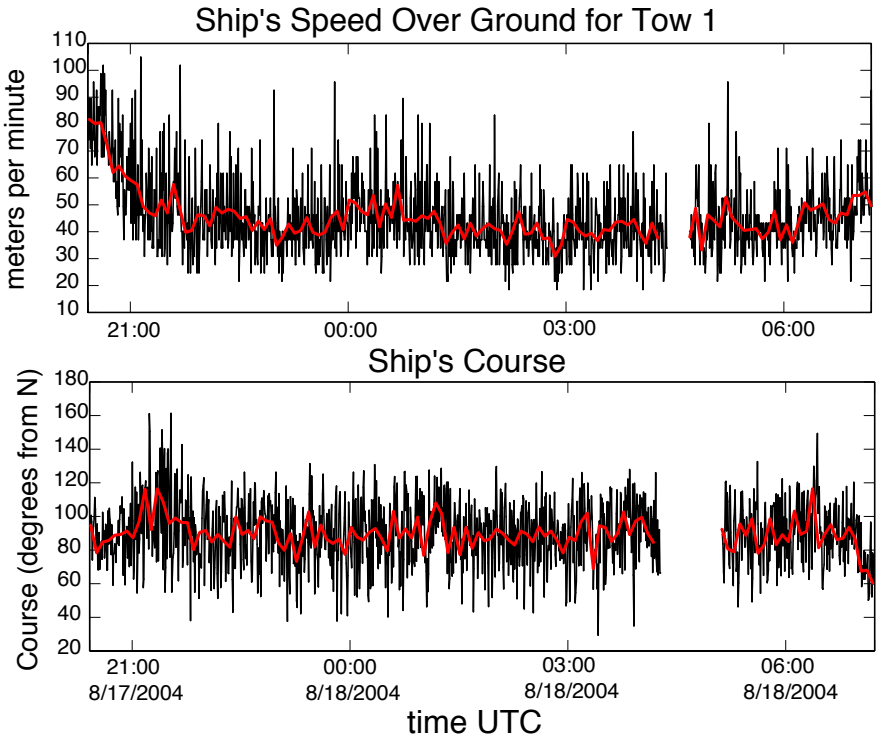


**Figure 3.9**: During CSEM Tow 1 the ship's speed over ground is kept at about 46 m/minute and the ship's course is approximately due east at 90°. The black line is all of the data and the red line is a moving average for the data. The GPS had a short blackout around 4:30 UTC time. The gaps in the time series for the ship's course are for unknown reasons.

During deep towing of the transmitter it is important to maintain a steep wire angle (short lay-back), which is done by keeping a slow and steady ship speed

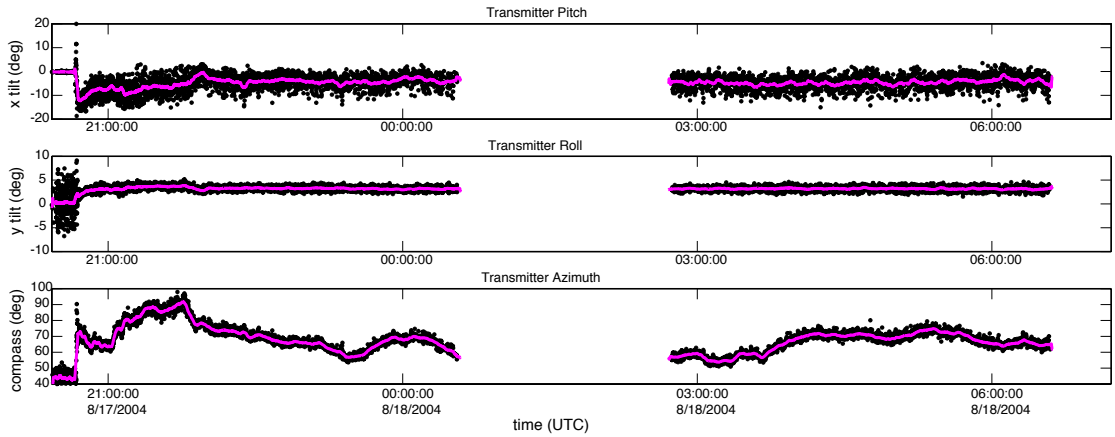


**Figure 3.10**: Tow 1 internal SUESI compass and navigational data. The pitch, roll and compass are internal measurements made during the tow providing a relative orientation of the transmitter. The depth and altitude come from two separate instruments, the *Parascientific* pressure gauge and the altimeter. The compass and tiltmeters failed for a duration of the tow for unknown reasons.

of about 1.5 knots (46 meters/minute). The sea state was very good during this survey, which allowed a steady ship speed (Figure 3.9). The variation in the ship's course is a result of variations in surface currents and wind. The New Horizon does not have dynamic positioning capability.

The transmitter contains an internal compass and tiltmeters to provide information about its relative orientation (Figure 3.10). The transmitter pitch suggests the transmitter is dipping by about 10°. The compass measurement is very different from the ship's course given in Figure 3.9 and is also very different from the computed orientation of the transmitter discussed later in the text.

### 3.4.2 Receiver

Two types of reciever configurations were used (Figure 3.11): a vertical electric (VE) receiver (odd numbered sites) and a magnetotelluric (MT) receiver (even numbered sites), allowing the collection of MT data at every other site. All receivers consisted of two horizontal perpendicular sets of Ag-AgCl (silver-silver

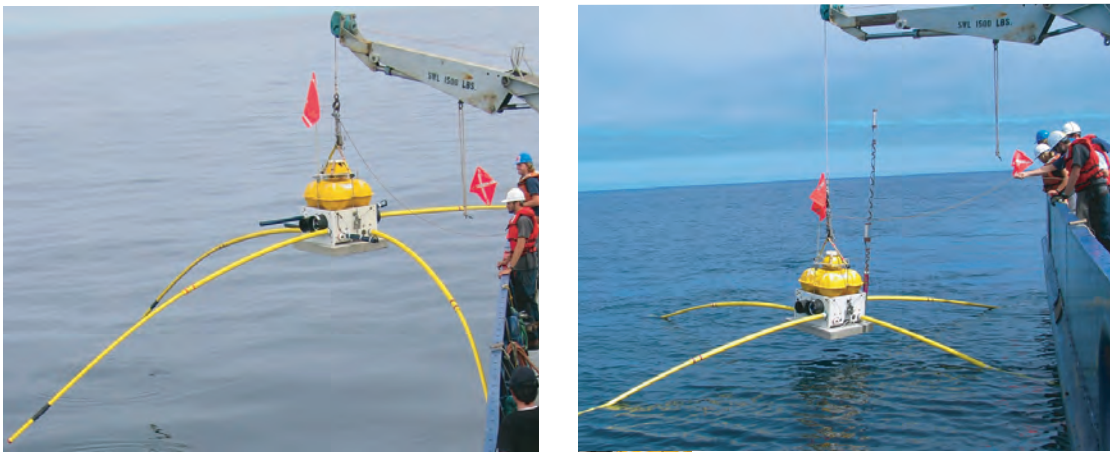

**Figure 3.11**: Two configurations of the ocean bottom electromagnetic reciever: magnetotelluric (MT) (left) and vertical electric (VE) (right).

chloride) electrodes on a 10 m dipole. The VE receiver had additional Ag-AgCl electrodes along a vertical 1.5 m dipole. The MT instrument had two horizontal and orthogonal induction coil magnetometers.

The receivers record both the natural time varying MT field of the earth and the synthetic man-made source from the transmitter, as well as any ocean-generated noise. A spectrogram for a magnetotelluric instrument is shown in Figure 3.12. The ocean acts like a low pass filter on the natural MT signal, only allowing frequencies below about 0.1 Hz to be detected. There is some electronic noise observed by the striping pattern when the instrument writes to disk, indicated by the tick marks on the top edge of the plots. There is a quiet period where the instrument is sitting on the deck of the ship, which is followed by a very noisy segment as the instrument falls to the seafloor (and noisy again at the end of deployment time when the instrument floats to the surface). There is a diurnal pattern observed as a result of ocean tides and/or daily variations in the MT signal. One can see the location of the 5 Hz and odd harmonic transmitted frequencies (at 00:00 Aug 18) as well as the CSMT tow of 0.1 Hz (at 15:00 Aug 18).

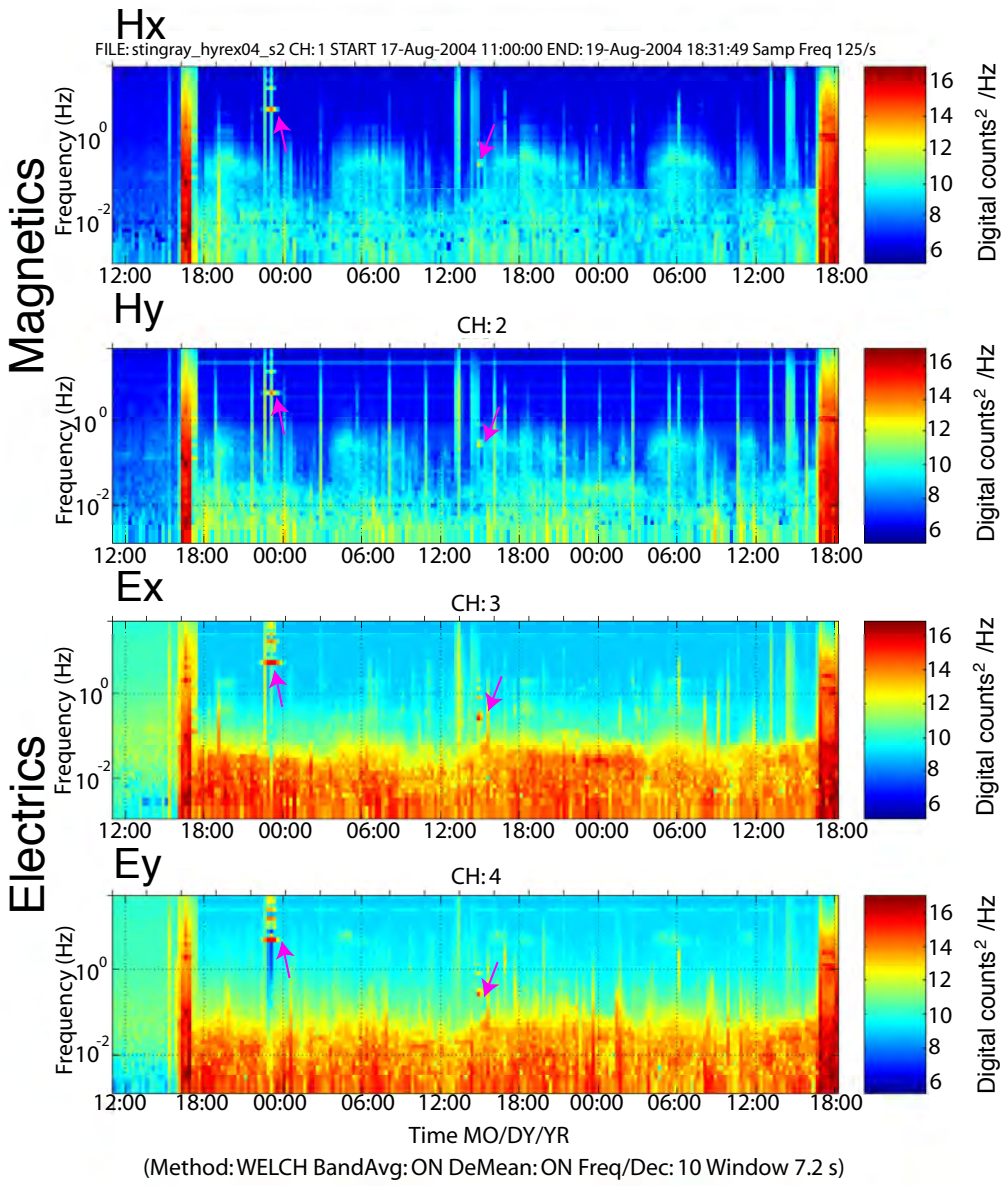


**Figure 3.12**: A spectogram for site 2 during the Hydrate Ridge experiment. Units are in digital counts per $\sqrt{Hz}$. Arrows up point to the CSEM signal of 5 Hz and arrows down point the the CSMT signal of 0.1 Hz.

One can also examine the time series when the transmitter signal is recorded by the receiver (Figure 3.13). The 5 Hz square wave is detected and shows a fairly good signal to noise ratio for the electric field sensors. The amplitude of the signal varies for each component depending on the orientation of the instrument relative to the transmitter. The vertical electric field has a smaller amplitude than the other two channels because it is collected on a shorter dipole (1.5 m versus 10 m). The magnetic field channels (channels 1 and 2 for the MT site s10) are modulated at low frequency by the natural magnetotelluric signal.

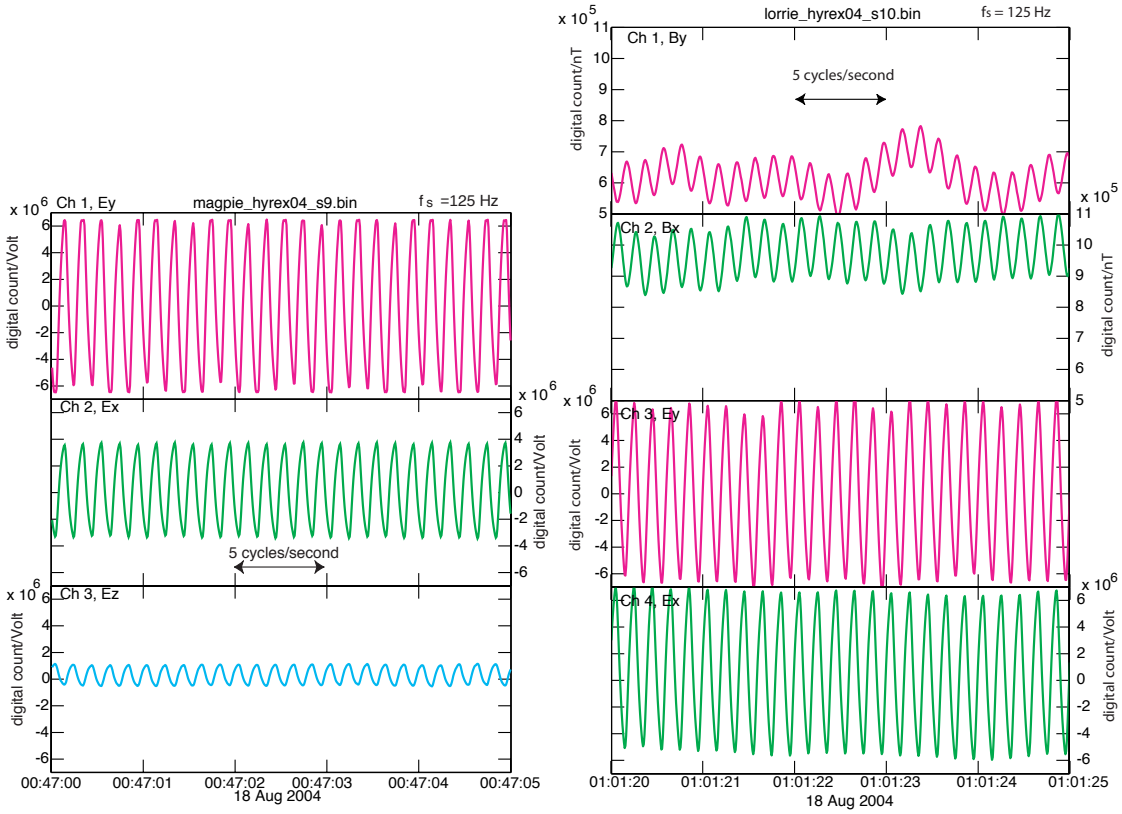


**Figure 3.13**: Vertical electric field configured receiver CSEM time series (left) and MT configured receiver CSEM time series (right). Both receivers show the 5 Hz signal from the transmitter, and the magnetic field recordings (top two panels on right) have evidence of the natural MT signal at a longer period. The vertical electric field recording (bottom left) has a much smaller signal because the recieving antenna (1.5 m dipole) is about 6.6 times smaller than the horizontal dipoles (10 m).

## 3.5 Data Processing

The data were processed using Behrens' (2005) *SFT6* Matlab based CSEM processing routine. The raw time series recorded by the receiver are cut into 120 second stack frames and fit with sinusoids of an angular frequency $\omega_i = 2\pi f_i$, where $i$ is the index of the frequency:

$$A\cos(\omega_i t) + B\sin(\omega_i t) = d(t) \tag{3.2}$$

and $A$ and $B$ are constant coefficients. This can also be represented in matrix form as:

$$\begin{bmatrix} \cos(\omega_i t_1) & \sin(\omega_i t_1) \\ \cos(\omega_i t_2) & \sin(\omega_i t_2) \\ . & . \\ . & . \\ . & . \\ \cos(\omega_i t_n) & \sin(\omega_i t_n) \end{bmatrix} \begin{bmatrix} A_i \\ B_i \end{bmatrix} = \begin{bmatrix} d_1 \\ d_2 \\ . \\ . \\ . \\ d_n \end{bmatrix} \tag{3.3}$$

which is an overdetermined system, allowing the coefficients $A$ and $B$ to be solved using a linear least squares factorization algorithm such as **QR**. The data at a particular frequency can be represented by an amplitude $|E|$ and a phase $\theta$:

$$d_{j,i} = |E_i|\cos(\omega_i t_j - \theta_i) \tag{3.4}$$

where

$$|E_i| = \sqrt{A_i^2 + B_i^2} \tag{3.5}$$

$$\theta_i = \tan^{-1}\frac{B_i}{A_i} \tag{3.6}$$

and $j$ is an index of stack frames.

The data loggers store several hours of data in RAM and then write the data to disk. The disk write operation creates electronic noise lasting about a minute but the *SFT6* routine ignores the coefficients at these times. Digital counts

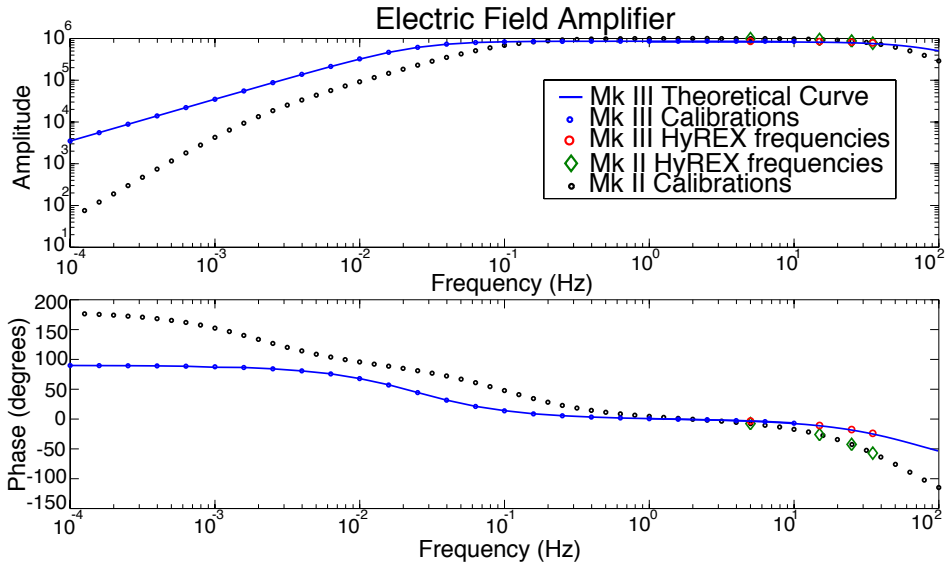


**Figure 3.14**: Electric field amplifier board calibrations for Mark II and Mark III data logger high gain ADC corrections.

are converted to volts, using the least count (V/count) of the analogue to digital converter, and then the data are normalized by the receiver's antenna length and the amplifier gain to get electric field in V/m. The data are then normalized by the transmitter dipole moment and the receiver amplifier transfer function applied.

The two generations of instruments used, Mark II and Mark III, have different amplifier transfer functions plotted in Figures 3.14 and 3.15. Higher frequency electric field calibrations were difficult to obtain because of high frequency laboratory noise. A theoretical curve was used to determine the higher frequency (odd harmonics of 15 Hz, 25 Hz, and 35 Hz from the 5 Hz fundamental transmitter frequency) calibrations for the Mark III electric field amplifiers, and an interpolation of calibration measurements was used for the magnetic field amplifiers for both generations of instruments.

Examples of calibrated amplitude and phase values versus a transmission time are shown for two sites in Figure 3.16 for a vertical electric field and

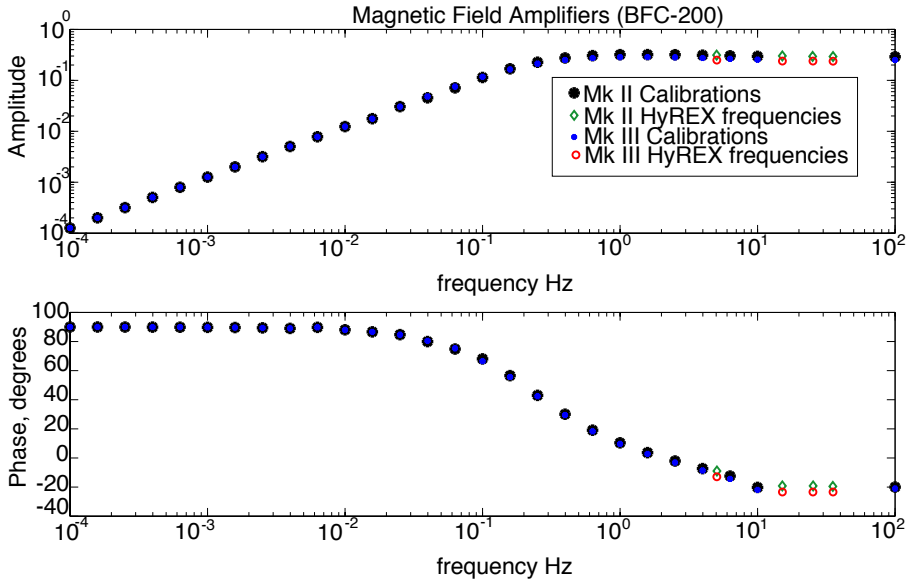


**Figure 3.15**: Mark III and Mark II data logger high gain ADC corrections for a magnetic field amplifier board.

magnetotelluric instrument versus transmission time. The closest approach of the transmitter to the receiver occurs just before 1:12 UTC for site 9 and at 1:12 UTC time for site 10. Unfortunately the electric field data are saturated at about $10^{-10}$ V/Am$^2$ because the electric field amplifier gains were set to 1,000,000. Subsequent work shows that the gain can be lowered without compromising long range data. The noise floor for the horizontal electric fields is about $10^{-15}$ V/Am$^2$ and $10^{-14}$ V/Am$^2$ for the vertical electric field (proportional to dipole length). The magnetic field sensors rarely saturate, as the gains are lower than for the electric field amplifiers. Magnetic field sensors have a noise floor of about $10^{-17}$ T/Am. When there is no signal from the transmitter or the signal is below the noise floor of the receiver the phase data are scattered.

The *SFT6* modules compute the polarization ellipse parameters, used in the next chapter to compute apparent resistivities. Finally, the data are merged with the transmitter's navigational parameters to obtain data (amplitude, phase,

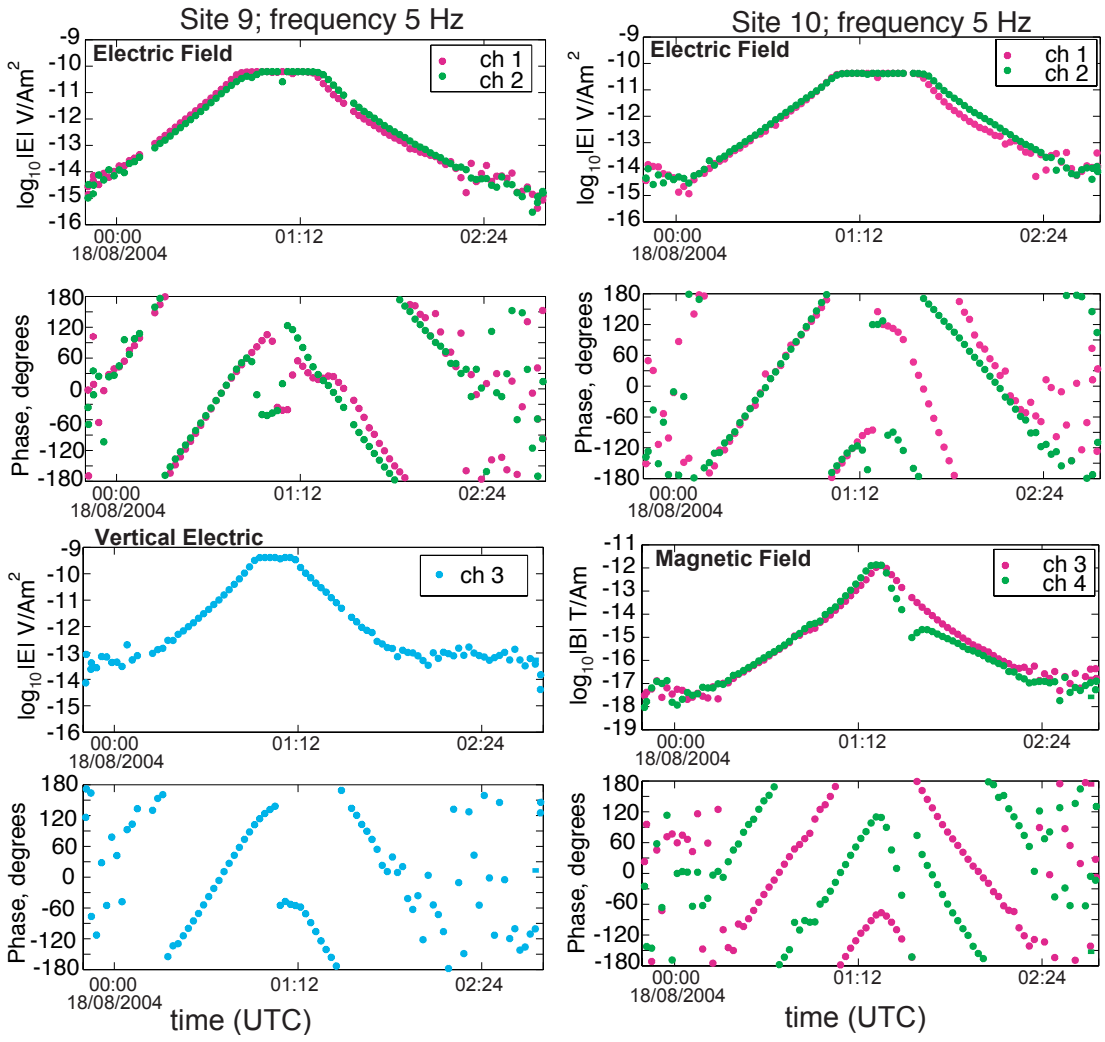


**Figure 3.16**: Amplitude and phase versus transmission time.

$P_{max}$) versus range. Issues associated with determining transmitter position accurately are discussed in Chapters 4 and 5.

# 4

# Preliminary Interpretation Using Pseudosections

## 4.1 Navigation

The Hydrate Ridge CSEM experiment was designed to target gas hydrates in the shallow seafloor (upper 150 m) and therefore required a relatively high transmitter frequency (of 5 Hz) compared to deep oil exploration. Because higher frequency electric fields vary more rapidly with source-receiver separation, the navigational data for the transmitter and receivers had to be more accurate than for earlier academic crustal-scale CSEM experiments (Cox et al., 1986). Accurate navigational data was meant to be collected using a rented, commercial short baseline (SBL) acoustic navigation system, but unfortunately this system failed. Instead, long baseline (LBL) acoustic navigation data were collected using a backup system, recording ranges between ship, receivers, and the transmitter.

### 4.1.1 Receiver Navigation

Receiver positions were found using a Marquardt inversion of LBL acoustic travel times, using seawater sound speed versus depth from the transmitter *Valeport* instrument (Figure 3.8 in Chapter 3).

Orientation of the receivers could not be determined using the internal

compass due to field distortion from nearby magnetometers and batteries. This issue has since been resolved by making the compass external to the instrument. Estimates for receiver orientation can be made by correlation with fields from a land site of known orientation (Key, 2003), but this was not possible here because there was no land site operating. Instead, receiver orientations were approximated by using the geometry of polarization ellipses of the electric or magnetic fields (Behrens, 2005), using forward modeling of the $x$ and $y$ components of electric and magnetic fields to resolve 180° ambiguities.

To find the orientation of the receivers using polarization ellipses it is assumed that the major axis of the ellipse is aligned with the transmitter axis (Figure 4.1) when the transmitter is located in-line with the receiver. The angle from channel 1 to the major axis of the polarization ellipse, $\alpha_N$, and the angle between the transmitter and north (TxRx) can then be used to compute the orientation of the receiver. However, there will be a 180° ambiguity that needs to be resolved using forward modeling. Finding the orientation of receivers based on 2D

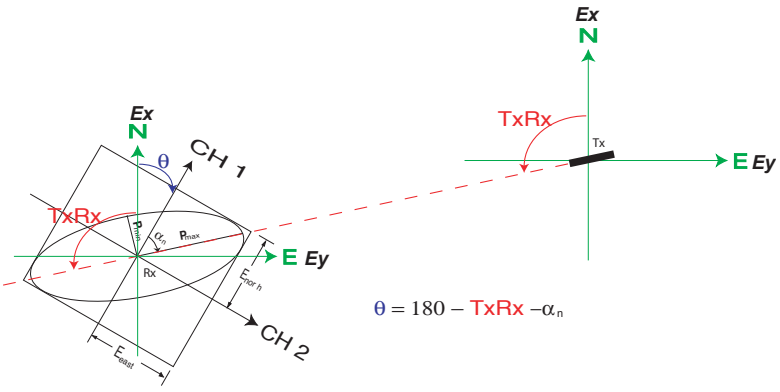


**Figure 4.1**: Illustration of how to compute the orientation of the receiver based on polarization ellipse parameters.

modeling is demonstrated for an MT instrument at site 4, as shown in Figure 4.2. 2D modeling is used to take into account any bathymetric effects on the data. A coordinate system with $y$ along the page and $x$ into the page is assumed. A pure

in-line response from a bathymetric half-space model is incrementally rotated and decomposed into $x$ and $y$ components. To first order the quadrant in which the receiver is oriented can be found by looking only at the magnetic field phase data, but inclusion of the electric field phase data helps to constrain this. In this particular example the magnetic phase data indicate the receiver could be in quadrants 2 or 4, and inclusion of the electric field phase data reveals it is in quadrant 2. The split between the two amplitude channels (electric and magnetic) determines the angle exactly as being well represented by both the 95° angle and the 178° angle. However, to get electric field CH 2 aligned with $y$ and magnetic field CH 1 aligned with $x$ requires the 178° orientation.

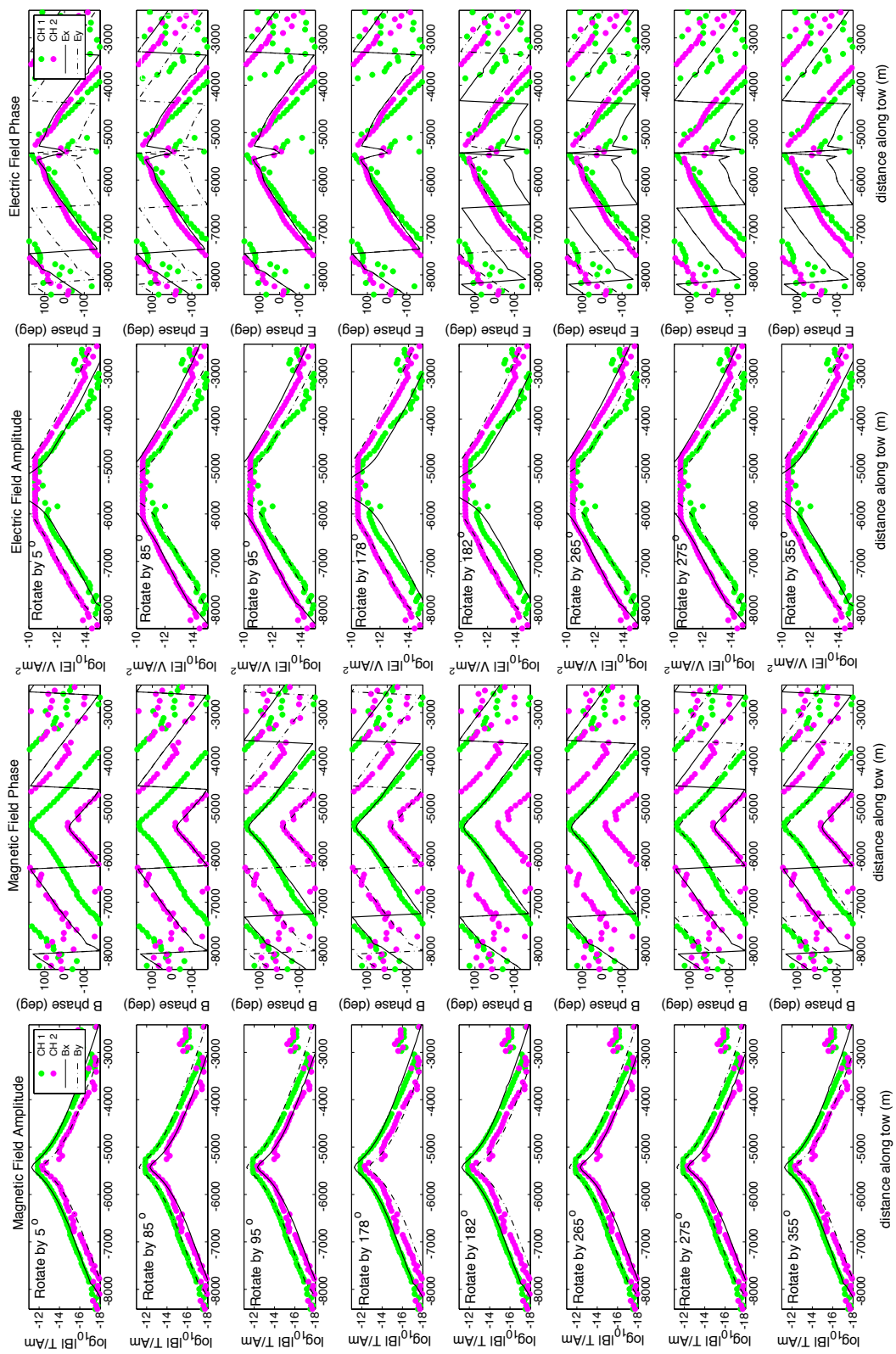


**Figure 4.2**: The orientation of receivers is found by rotating an in-line 2D model.

### 4.1.2 Transmitter Navigation

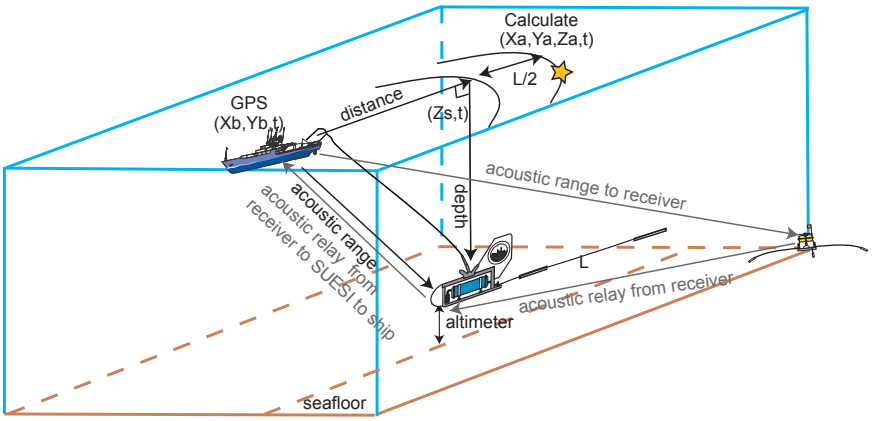


**Figure 4.3**: The transmitter position was modeled assuming the transmitter followed directly behind the ship and is somewhere on a horizontal arc. We were able to use acoustic relays from the receivers to transmitter to get an idea of which side of the arc the transmitter path took.

To first order it can be assumed the transmitter follows directly the path of the ship at a horizontal distance computed from the transmitter depth and the acoustic slant range (distance from the ship to the transmitter, Figure 4.3). This distance changes with depth and ship's speed. Global positioning system (GPS) provides the latitude and longitude for the ship. Figure 4.4 shows these measurements, as well as a comparison of the actual water depth of the transmitter (from summing the depth gauge and altimeter) compared with that mapped by the ship's echosounder.

The transmitter may be set to one side of other of the ship's track by water currents. This can be estimated by including acoustic relays from the receivers to the transmitter (Figure 4.3), providing an intercept of the acoustic range from the receiver and the transmitter arc. The acoustic relay navigation model was used for the first results paper (Weitemeyer et al., 2006c).

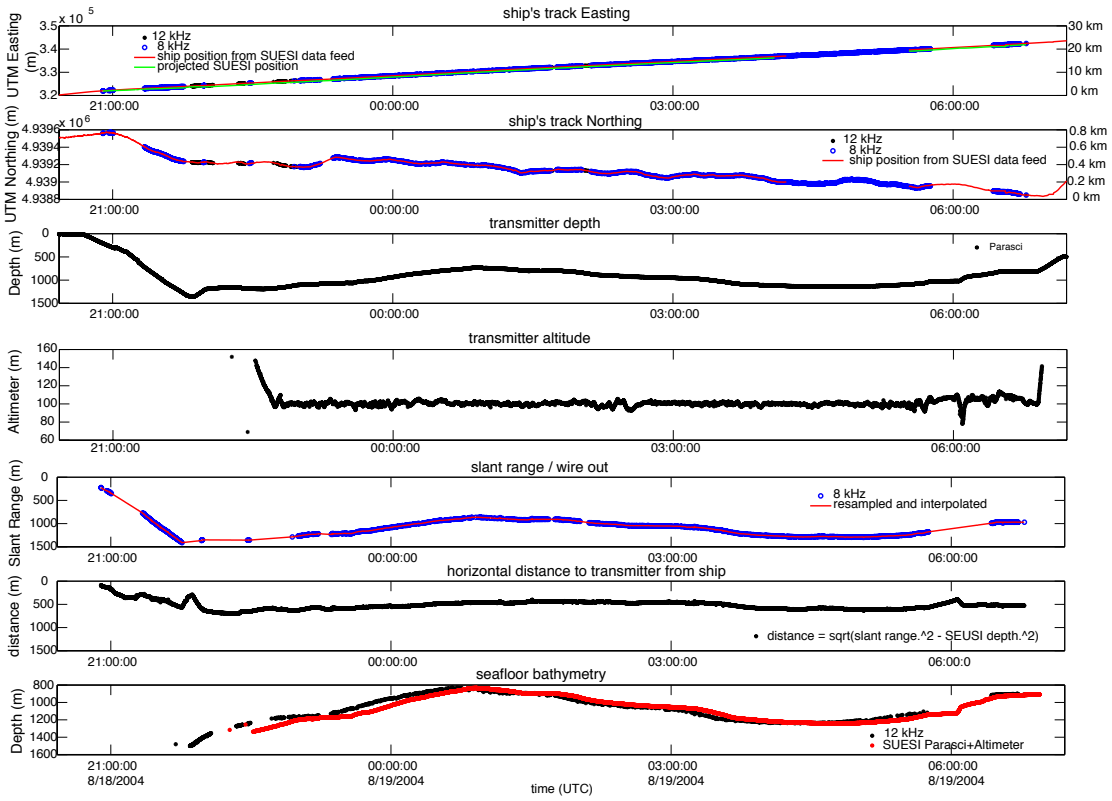


**Figure 4.4**: Data used in computing the position of the transmitter located on an arc behind the ship. The easting and northing for the ship and the calculated transmitter position, assuming it follows the ship's path, are shown in the top two panels. The depth of the transmitter for the duration of the tow and the slant range are the data input into Pythagoras' theorem to give the distance of the transmitter behind the ship (second to last panel). The bottom panel is a comparison of the 12 kHz echosounding seafloor depth from the ship with the transmitters computed seawater depth (altimeter + transmitter depth). N.B. 8 kHz is the ship to transmitter to ship acoustic relay.

A comparison of the two models for transmitter location is shown in Figure 4.5. The northing and easting plots differ in a number of places. The depth differs considerably in the beginning of the tow because of the large shift in easting for the distance and relay calculations. The transmitter rotation (angle from geodetic north) was computed from the difference between successive transmitter positions. The transmitter rotation for the most part is around 90°, but there are some frequent oscillations.

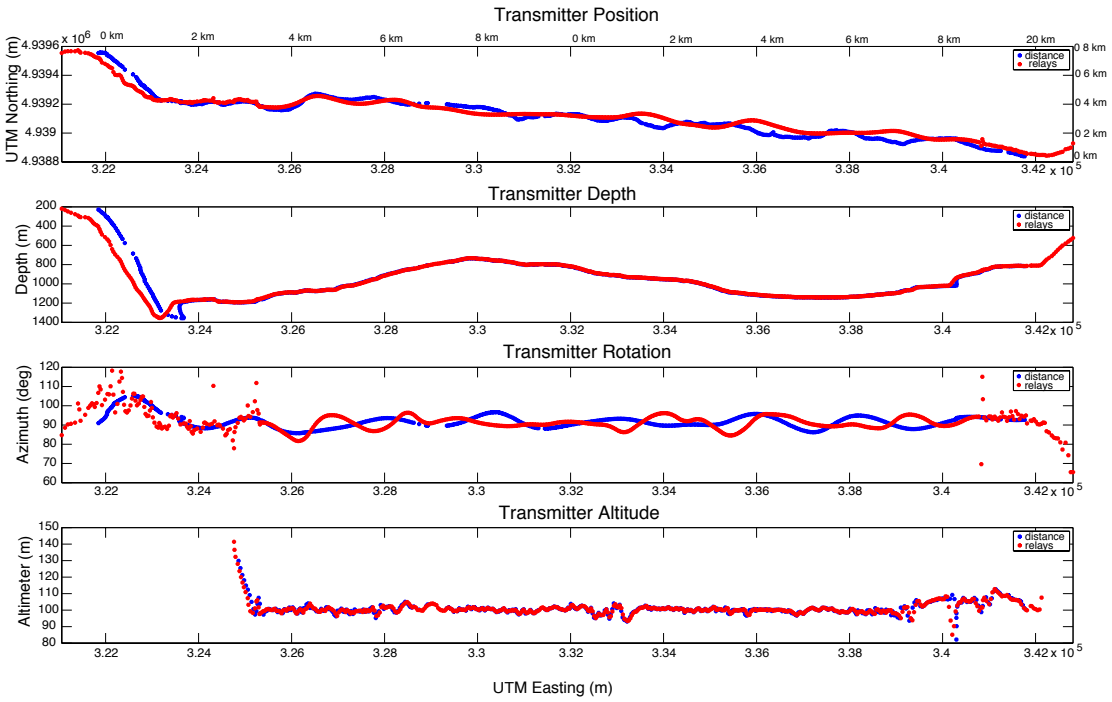


**Figure 4.5**: The two different models for transmitter position based on, (1) the arc the transmitter (blue) may be on, and, (2) the relays from the receivers (red). The top panel is a map view of transmitter position, the next panel is the depth versus easting, the second to last is the transmitter rotation and finally the altitude of the transmitter.

We tried to improve transmitter navigation by matching the 10 m resolution bathymetry data collected by Clague et al. (2001) with the depth observed at the transmitter (altimeter + depth). However, the bathymetry is relatively uniform and there were not enough constraints to get a meaningful transmitter position.

The antenna rotation and dip are not well constrained (Figure 4.6), and cannot be constrained without the use of a short or long base-line acoustic navigation system on the tail end of the antenna. The dip of the antenna may vary because the transmitter is pulled in or let out to maintain a constant towing al-

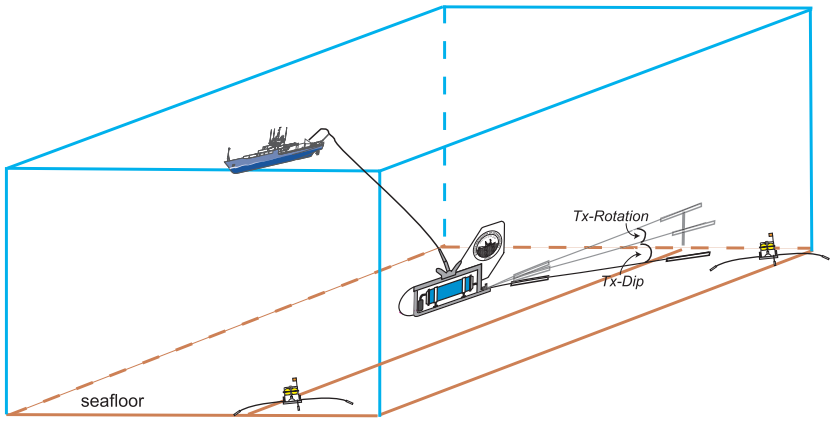


**Figure 4.6**: The antenna dip and the antenna rotation are unknown in all assumptions about transmitter navigation.

titude over seafloor bathymetry, or because the antenna is not perfectly neutrally buoyant.

### 4.1.3 Merge Navigation with $P_{max}$

The transmitter navigational model is approximate, and for this reason the data are expressed in terms of polarization ellipse parameters. This is because the major axis of the polarization ellipse, $P_{max}$ is insensitive to receiver orientation and relatively sensitive to transmitter azimuth (Flosadóttir and Constable, 1996). Range (source-receiver offset) is well constrained in the current navigation model to within 50 m.

The transmitter navigational parameters (range, azimuth, and altitude as a function of time) were merged with each receiver's polarization ellipse parameters, $P_{max}$, $P_{min}$, and $\alpha_N$ versus transmission time in order to get the polarization ellipse parameters versus range (Figure 4.7). The 5 Hz data reached a noise floor at about a 2.5 km range and the 15 Hz data at about a 1.5 km range.

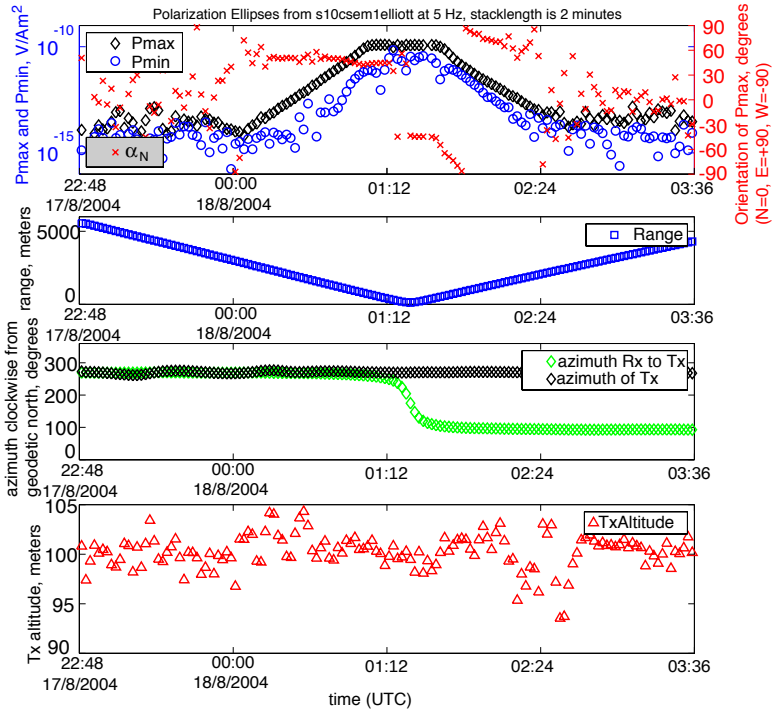


**Figure 4.7**: The amplitude and phase of the two electic field channels were converted into the polarization ellipse parameters: $P_{max}$, $P_{min}$ and $\alpha_N$ versus transmission time. These were merged with the navigation parameters of the transmitter, $x$, $y$, $z$, azimuth and altitude in order to change the transmission time into a range (source receiver offset). The transmitter azimuth flips 180 degrees as it crosses over top of the receiver.

## 4.2 Electrical Resistivity

A look up-table method was used to convert $P_{max}$ amplitudes to apparent resistivities. A table of electric field amplitudes was generated for models of half-space resistivities and ranges using the 1D layered code of Flosadóttir and Constable (1996). Interpolation was then used to convert the 5 Hz and 15 Hz electric field data at each receiver and each range into an equivalent half-space apparent resistivity. Figure 4.8 gives an example of this for site 10. The values of apparent resistivity versus range varied between 1 and 3 Ωm.

To obtain a quick image of the subsurface structure and heterogeneity

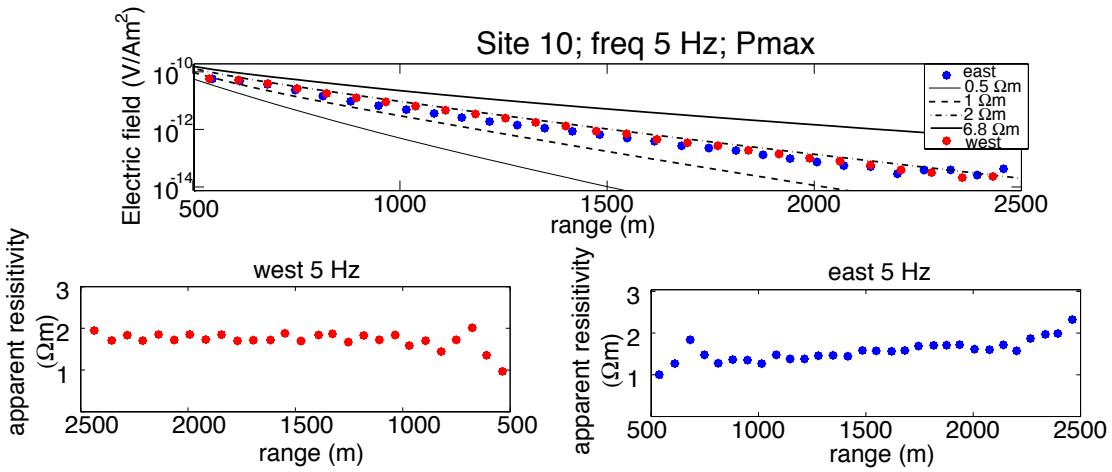


**Figure 4.8**: The look-up table method involves computing a number of half-space resistivities of 0.5 Ωm to 6.8 Ωm versus range to obtain a $P_{max}$ electric field amplitude for the various half-spaces. From this one can find the best half-space resistivity represented by the field data. This is an example for site 10 with data separated into the transmitter to the east and to the west of the receiver. The apparent resistivity for this site falls around 2 Ωm

across the CSEM profile without the complication of a 2D inversion, a pseudosection technique (a method used extensively in land DC resistivity and IP surveys) was used. This provides a way to look at all of the CSEM data collected at every site in one single image. The midpoint between the source and receiver is plotted at a depth given by a 45° projection from the source and receiver, shown in Figure 4.9. EM induction is not a purely geometric phenomenon and so this image is not a depth section.

## 4.3 Pseudosection Results

Contoured apparent resistivity pseudosections are shown in Figure 4.10. Reciprocity between the transmitter and receivers creates a two-fold redundancy in the data with separate pseudosections from east-side and west-side transmissions. The two pseudosections have different sensitivities and there are subtle differences between them. The pseudosection projection technique causes the west

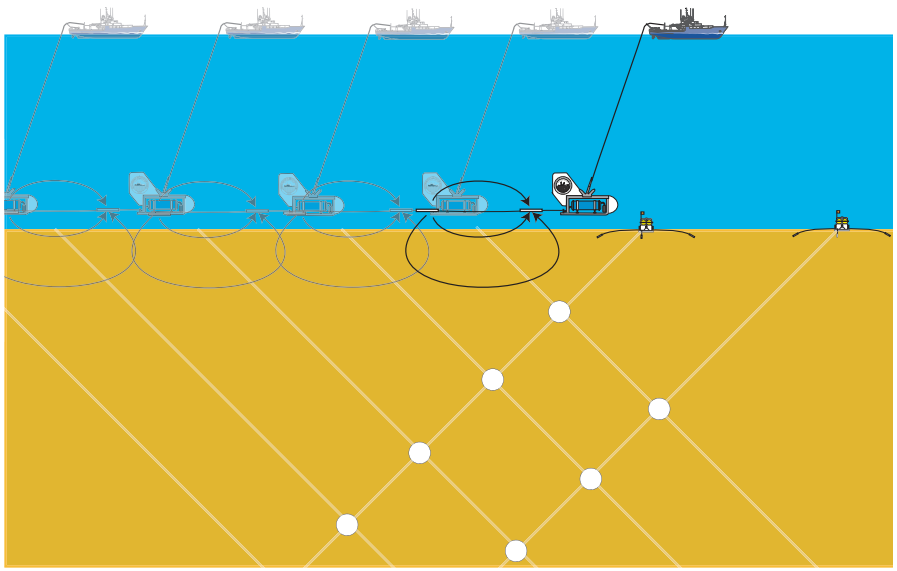

**Figure 4.9**: The pseudosection projection technique is created by taking the midpoint between source and receiver and projecting it down at a 45° angle from the horizontal. This imaging technique was used for both the 5 Hz and 15 Hz data.

pseudosection to have a striping pattern to the west and vice versa for the east pseudosection. This pattern is most obvious for the shallow conductor under site 6. However, the east-side and west-side pseudosections (Figure 4.10 top and middle panel) are sufficiently similar that an average of the two can be taken (Figure 4.10 bottom panel). The combination of the east and west averages the striping pattern except under site 6, where a classic pseudosection "pant-leg" feature is present.

All three pseudosections display a more conductive basin under sites 18 to 25 that increases in resistivity with depth. This is likely a result of a decrease in porosity due to compaction. The pseudosections also give a resistive anomaly where an anticline is evident in the seismic data under sites 16 and 17. The ridge is more resistive under sites 9 to 13. Finally there is a large resistor under sites 1 to 4, particularly evident in the west pseudosection which extends further in this direction.

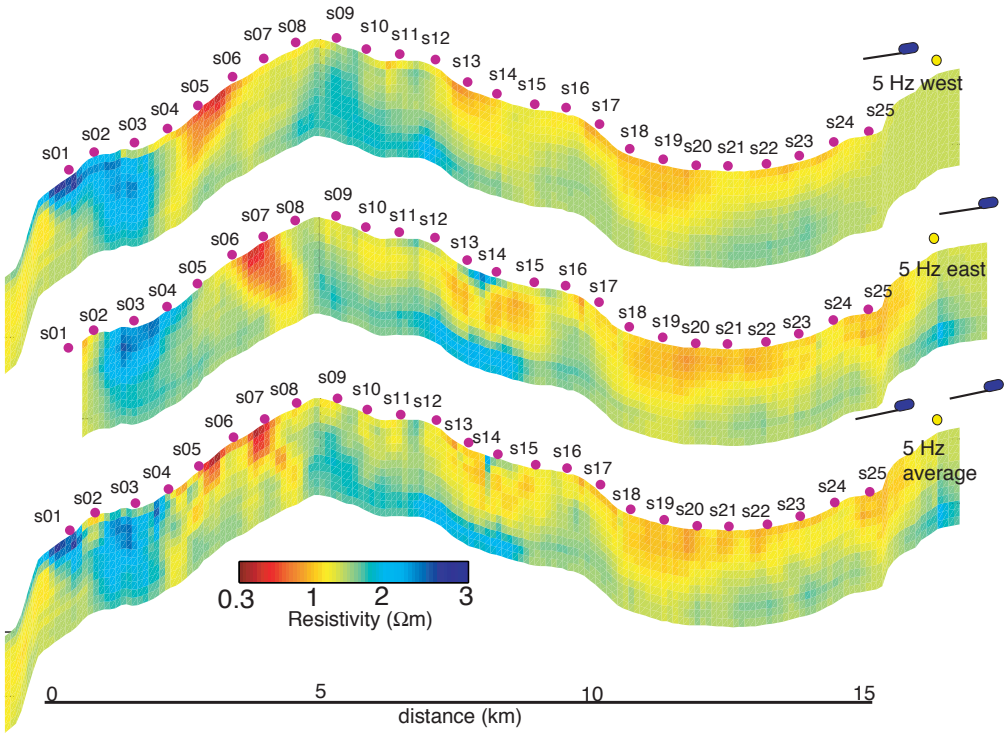


**Figure 4.10**: Resistivity pseudosection of 5 Hz data for a transmitter positioned to the west (top), east (middle), and for combined east and west transmitter positions (bottom).

The pseudosection projection technique was also applied to the 15 Hz data, shown along with the 5 Hz and 15 Hz data in Figure 4.11a and b and Figure 4.12a and b. The 15 Hz pseudosection is sensitive to shallower sediments because of the shorter EM penetration depths and shorter offsets, and this is reflected by a general agreement with the top of the 5 Hz pseudosection. The pseudosection projection method is better at imaging lateral resistivity variations than those that vary with depth. To obtain a true depth section a 2-D inversion is required. However, to gain some insight into the depth extent of the pseudosection a 1D Occam inversion was performed in two regions of the pseudosection marked by the boxes in Figure 4.11a and b, where lateral variations in resistivity are smaller than the vertical variations.

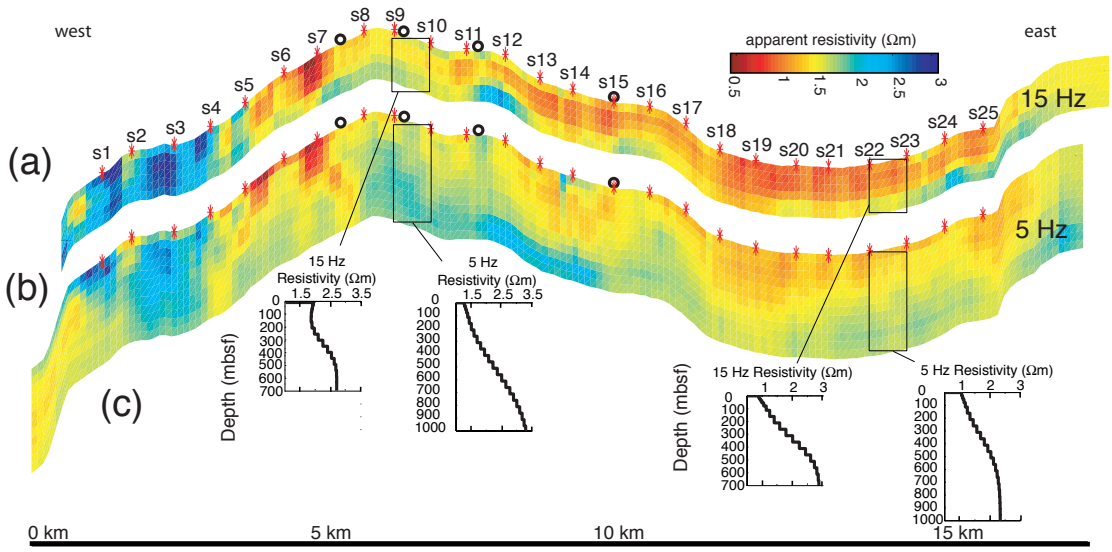


**Figure 4.11**: (a) 15 and (b) 5 Hz data in pseudosection form with a combined apparent resistivity (c) and 1D Occam inversion results. EM receiver sites are marked by red asterisk. From Weitemeyer et al. (2006c).

## 4.4 1D Occam Inversions

A 1D Occam inversion was run to produce a smooth model that fits the data to an acceptable tolerance without introducing unnecessary structure (Constable et al., 1987). The basin structure (sites 18 to 25) appears to be one-dimensional, with sedimentary layers observed in seismic data (Figure 4.12c), and so a smooth 1D inversion (Flosadóttir and Constable, 1996) was applied to all the data that fall in between sites 22 and 23 (Figure 4.11c). The steepest gradient of resistivity with depth in both models lies at about 400 m deep, providing some control on the depth of the resistivity increase in the pseudosection projections. Similar inversions at the ridge between sites 9 and 10 near ODP Leg 1246 (Figure 4.12c) indicate depth of penetration around 500 m for the 15 Hz data and 1000 m for the 5 Hz data.

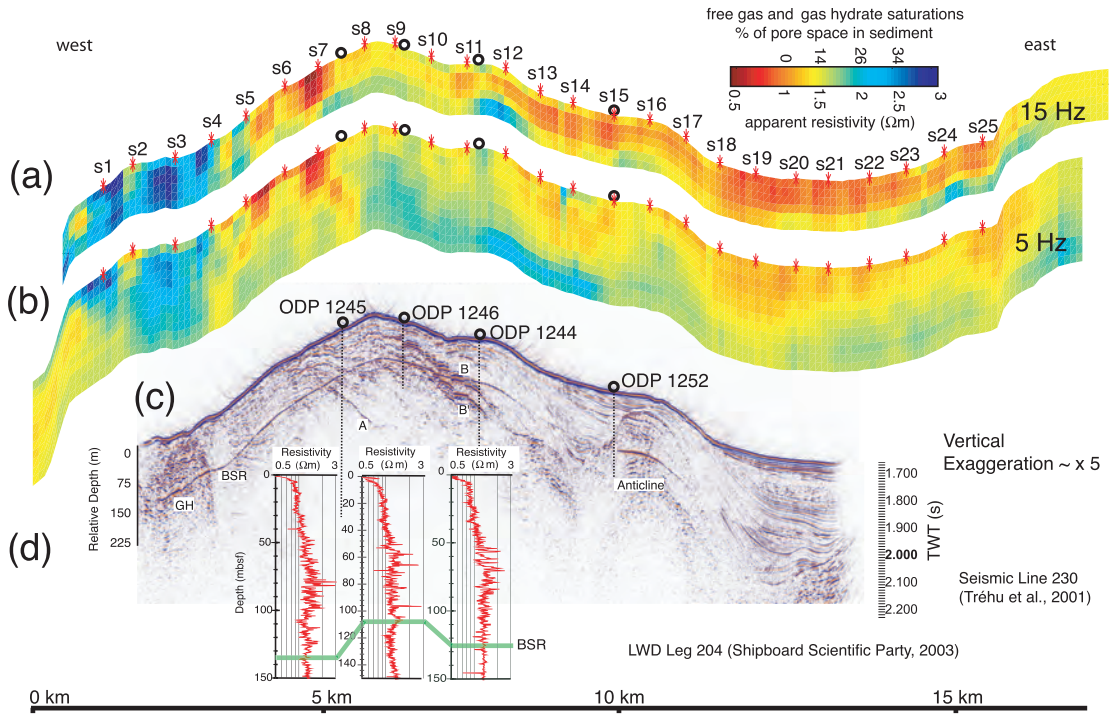


**Figure 4.12**: (a) 15 and (b) 5 Hz data in pseudosection form with a combined apparent resistivity and gas hydrate saturation scale linked through Archie's Law; (c) seismic line 230, and (d) logging-while-drilling (LWD) deep resistivity logs. GH - gas hydrate or free gas inferred from a seismic inversion (Zhang et al., 2003); BSR - bottom simulating reflector; A, B, B' - seismic horizons explained in text. ODP Leg 204 sites are marked on seismic section. EM receiver sites are marked by red asterisk (from Weitemeyer et al. (2006c,b)).

## 4.5 Comparison with Resistivity Well Logs and Seismic Data

Figures 4.12c and d also display seismic line 230 reflectivity data (Tréhu and Bangs, 2001) and ODP Leg 204 logging while drilling resistivity logs (Tréhu et al., 2003) for ODP Sites 1245, 1246, and 1244, allowing comparisons to be made between these data sets and the pseudosections. In regions where little or no hydrate is thought to exist (as in the basin sites s18-s25) we observe more conductive (red) features, and in regions where more hydrate is expected we observe more resistive features (blue) (as on the summit near sites s4-s17). This is consistent

with estimates of higher concentrations of hydrate at the ridge compared to the basin (Tréhu et al., 2004). As previously mentioned, the anticline (under s16 and s17) seen in the pseudosections corresponds to an anticline in the seismic section and is probably associated with a change in lithologic composition. This feature is barely seen in the 15 Hz data, suggesting a resistive core to the anticline that is deeper than 400 m. The high resistivity seen in the 5 Hz data below s8-s15 could be associated with horizons B and B', which consist of highly faulted coarse grained and/or volcanic ash-rich horizons which show high resistivities in logging while drilling data at ODP 1246 (Shipboard Scientific Party, 2003). Two anomalous regions exist: a highly resistive feature to the west (s1-s5), and a conductive feature under sites 6 and 7. The resistive feature is consistent with a seismic inversion by Zhang and McMechan (2003), who inferred that this region contains higher concentrations of hydrate and free gas. The conductive feature projecting from s6 is probably a result of the receiver sitting directly over a conductor, such as a brine. This is not unreasonable considering the evidence for brines to the south at ODP 1249 and 1250 (Milkov et al., 2004; Torres et al., 2004).

To convert apparent resistivities into an approximate hydrate concentration, a simple Archie's Law calculation (Equation 1.1, Chapter 1) is done following the method of Collett and Ladd (2000) and ODP Leg 204 Initial Reports (Shipboard Scientific Party, 2003). The resistivity of the formation water is assumed to be seawater ($R_w$= 0.33 Ωm); the formation resistivity is taken from the CSEM pseudosection; and the porosity of the sediments is taken as an average value of 65% for the gas hydrate stability zone (Tréhu et al., 2003, 2004). The Archie's empirical parameters $a$, $m$, and $n$ used are from nearby ODP Leg 204 well log data ($a$=1, $m$=2.8, $n$=1.9) (Tréhu et al., 2003). The resulting hydrate concentration varies from 0-30%. The basin has 0% hydrate concentration at the surface and increased concentration at depth consistent with reported higher concentrations of hydrate just above the BSR (Shipboard Scientific Party, 2003). At the ridge con-

centrations are 10% to 15%, similar to the 8% previously estimated (Tréhu et al., 2004). West of the ridge are very high hydrate concentrations of about 30%. The EM derived concentrations are subject to any inaccuracies in Archie's equation and to our assumption of uniform values for the associated formation parameters.

## 4.6 Conclusions

The initial analysis of this data set was published in Weitemeyer et al. (2006c) and provided a demonstration of CSEM's potential to image gas hydrate and provide rough hydrate concentration estimates based on Archie's Law. These concentrations were similar to Tréhu et al. (2004). In this chapter use of the major axis of the polarization ellipse ($P_{max}$), and a relative coordinate system between transmitter and receiver similar to that by Constable and Cox (1996), allowed an analysis of the data using only 1D modeling and pseudosection projections. However, to place real depth constraints on the pseudosection images requires a 2D inversion of the data. For this the data must be analysed in an absolute coordinate system ($x$,$y$,$z$) which requires tighter navigational data for the transmitter, the subject of the next chapter.

.

# 5

# Total Field Navigation

## 5.1 Problems with Current Navigation

The quality of marine CSEM data is dependent on accurate navigational information for the transmitter and the receiver positions and orientations. Conventional methods, such as short baseline (SBL) acoustic navigation systems, may not be accurate in all circumstances and may even fail, as happened in the Hydrate Ridge CSEM experiment. The long baseline (LBL) acoustic navigation discussed in Chapter 4 provided limited accuracy for the cross-tow set and no indication of transmitter dip. However, by utilizing the near field electromagnetic (EM) radiation pattern of the horizontal electric dipole source, the cross-tow position and dip of the transmitter can be modeled. Near field (in this case $< 1.5$ km in source-receiver offset) electric and magnetic data collected by seafloor receivers are less sensitive to seafloor resistivity than far field ($> 1.5$ km) data, and can be used to refine the geometry of the transmitter and receivers. A Marquardt inversion was developed to solve for navigational parameters including transmitter position, rotation, and dip and receiver position and orientation. The inversion program uses a one dimensional dipole forward modeling code, *Dipole1D* (Key, submitted), and requires an initial model of half-space seafloor resistivity and the geometry of the transmitter and receivers. The program updates the model parameters until convergence is reached between the synthetic EM responses and the observed EM

data. We call this technique "total field navigation" and applied it to the Hydrate Ridge data.

The total field navigation method requires the use of an absolute coordinate system $(x,y,z)$ which meant all receiver channels had to be oriented, as was discussed in Chapter 4. Since the phase data is no longer treated in a relative sense an absolute phase is required. At the time of the Hydrate Ridge experiment the transmitter was relatively new and the absolute phase of the transmitter output was not measured directly. Transmitter phase was estimated by a comparison of the magnetic field phase data at closest approach of the transmitter to synthetic phases from a model of a seafloor half-space (Figure 5.1). An absolute phase correction of 40° was estimated and found to be valid during the entire tow and for all receivers.

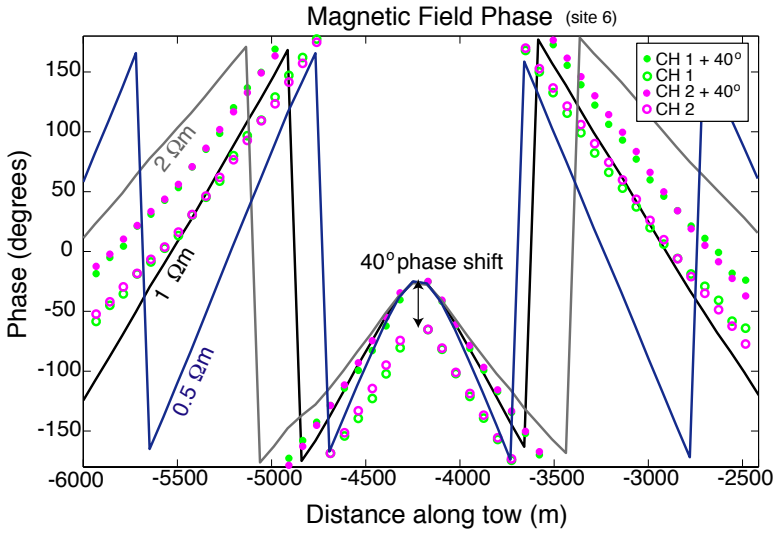


**Figure 5.1**: The phase recorded at site 6 for the two magnetic field channels is shown along with an absolute phase correction of 40° to account for the timing of the transmitter. Bathymetric half-space resistivity models of 0.5, 1 and 1 Ωm's are included as a reference.

Another issue with the use of near-field data is the saturation of the

electric field amplifiers. For the 5 Hz transmission, saturation occurs at about a 750 m range on the 24 bit instruments. Fortunately, the phase data are recoverable from saturated amplitudes. Most of the magnetic field data did not saturate.

## 5.2 General Features of a Dipole

### 5.2.1 Whole Space Dipole Field

To gain some intuition about the behavior of the electric dipole and understand the phase polarities for the field components we consider a sketch of a whole-space electric dipole field in Figure 5.2, for a dipole aligned along the $y$-axis.

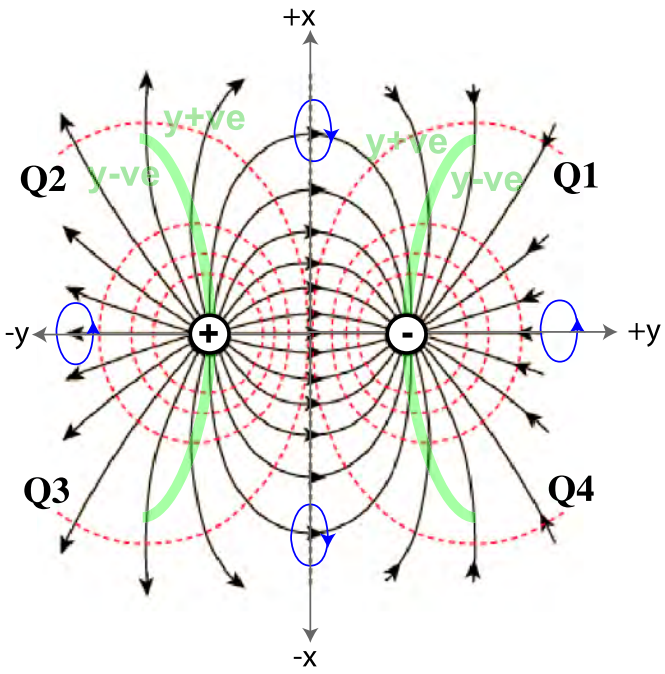


**Figure 5.2**: Sketch of the electric dipole field with equipotential field lines in red and a few examples of the magnetic field (in blue) curling around the electric field lines (in black). The green lines indicate where the $y$ component of the electric field changes direction. The four quadrants are marked Q1, Q2, Q3, and Q4. Modified from http://hyperphysics.phy-astr.gsu.edu/Hbase/electric/dipole.html.

The direction of the dipole field lines indicate the sign of the phase with

respect to the $x$ and $y$ directions for the cross-line $E_x$ and in-line $E_y$ components. In quadrants 1 and 3 the electric field lines are pointing in the negative $x$ direction, so the $x$-phase is negative. In quadrants 2 and 4 the electric field lines are pointing in the positive $x$-direction, so the $x$-phase is positive. For the $E_y$ component the phase is symmetric about the $x$-axis, and there is a phase change within each quadrant across the lines where $E_y$ goes to zero (marked green in Figure 5.2). The $E_z$ component ($z$ positive into the page) has a 180° phase jump across the $x$ axis. For an observation point at $z>0$ (i.e. below the plane of the transmitter) the phase is negative on the negative side of the dipole and the phase is positive on the positive side of the dipole. For an observation point at $z<0$ (above the plane of the transmitter) this is reversed. The magnetic field phases can be determined in a similar manner using the right hand rule; magnetic fields curl around electric fields. Clockwise magnetic fields have negative phase and vice versa.

### 5.2.2 Navigational Effects on Dipole Fields in a Half-space

To model real data we need to replace the whole-space with a half-space and use 1D forward modeling of an arbitrarily oriented transmitter. The mathematical description of the horizontal electromagnetic dipole (HED) source can be found in Chave and Cox (1982) and in Ward and Hohmann (1987). The 1D CSEM forward modeling fortran code, *Dipole1D*, used in this study was developed by Key (submitted) and uses a Lorentz gauged vector potential formulation of Maxwell's equations and Kong's (2007) digital filter coefficients for the Hankel transforms. Unlike the code of Flosadóttir and Constable (1996) it is capable of computing the EM fields from an arbitrarily oriented electric dipole transmitter.

*Dipole1D* uses a right-handed cartesian coordinate system, rather than a cylindrical coordinate system, allowing direct comparison of model response with field data without the need of a coordinate transformation. Figure 5.3 outlines the geometry considered: transmitter rotation is the angle from the $x$-axis to the

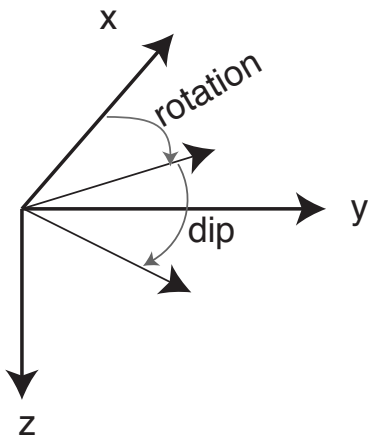


**Figure 5.3**: The coordinate system is a right handed coordinate system where $x$ is into the page, $y$ is along the page and $z$ is positive down. The transmitter may be rotated clockwise at an angle from the $x$ axis or may have a dip positive down from that angle. For the purposes of analyzing the Hydrate Ridge data set positive $x$ will also be considered geodetic north and positive $y$ will be geodetic east.

antenna in the horizontal plane, and transmitter dip is the antenna angle from the horizontal plane into the vertical position.

We first consider a model consisting of a 1 Ωm seafloor with seawater resistivity of 0.3 Ωm and a grid (800 m in $x$ by 3000 m in $y$) of transmitters spaced 25 m apart, 100 m above a single receiver placed on the seafloor at the center of the grid. The grid of 1037 transmitters have the same 90° transmitter rotation and 0° dip throughout the model (Figure 5.4).

Common to all electric and magnetic field components are phase jumps and decreases in amplitude when the transmitter crosses the axis of the receiver. The sign of the 180° phase jump in $E_x$ and $B_y$ is dependent on whether the transmitter is on the north ($+x$) or south (-$x$) side of the receiver, an important indicator for transmitter location unresolved with in-line data ($E_y$, $E_z$ and $B_x$) alone. The $E_z$ component has a single 180° phase jump resulting from the change

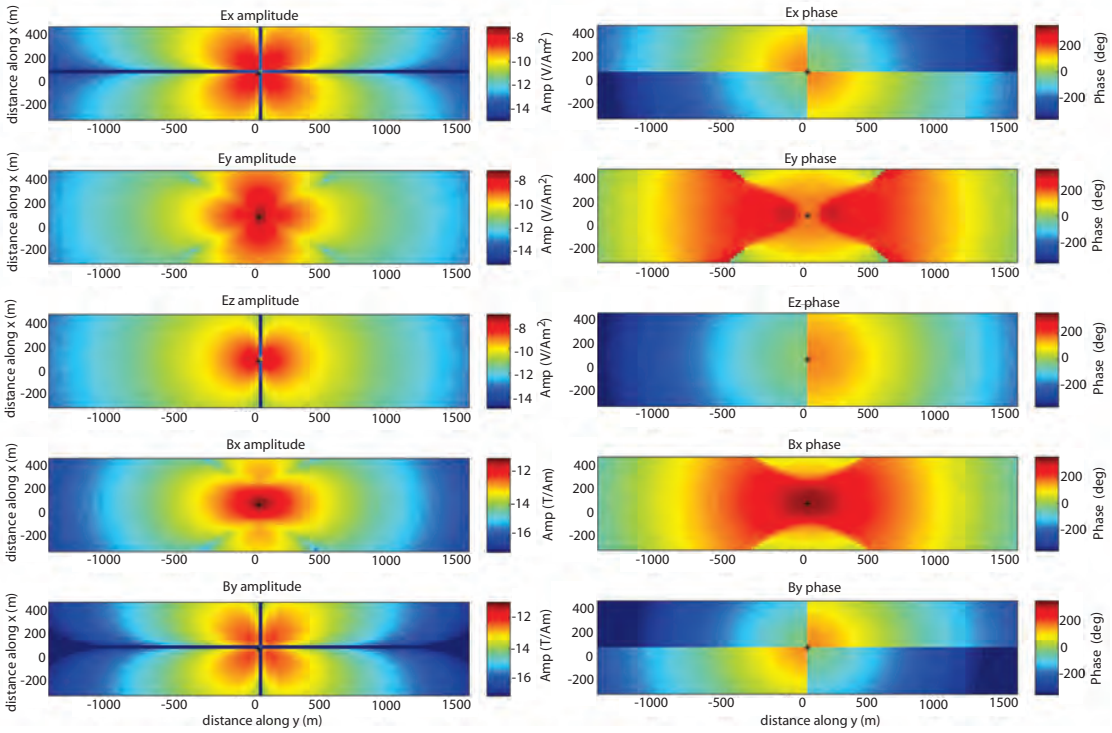


**Figure 5.4**: Electric and magnetic field amplitude and unwrapped phase for a grid of horizontal electric dipole transmitters in plan view, all at a rotation of 90° and a dip of 0°, for a 5 Hz transmission frequency into a 1 Ωm seafloor half-space.

in sign of the dipole field lines. The in-line $E_y$ has two 90° phase jumps that are symmetric about the $x$ axis and whose distance depends on the separation of the transmitter and receiver along $x$. The $E_y$ phase is 180° where the transmitter is 100 m directly above the receiver because $E_y$ is associated with a return current there. In our field data some of the $B_y$ and $B_x$ do not saturate at close range and so the cusps in amplitude can be used to constrain the orientation and position of the transmitter and receivers. Saturation of the electric field amplifiers eliminates the close-range features in electric field amplitude for constraining the dip and rotation of the transmitter.

Having examined the general features for purely $y$-oriented transmitters we can examine the influence of changing the rotation and dip of the antenna.

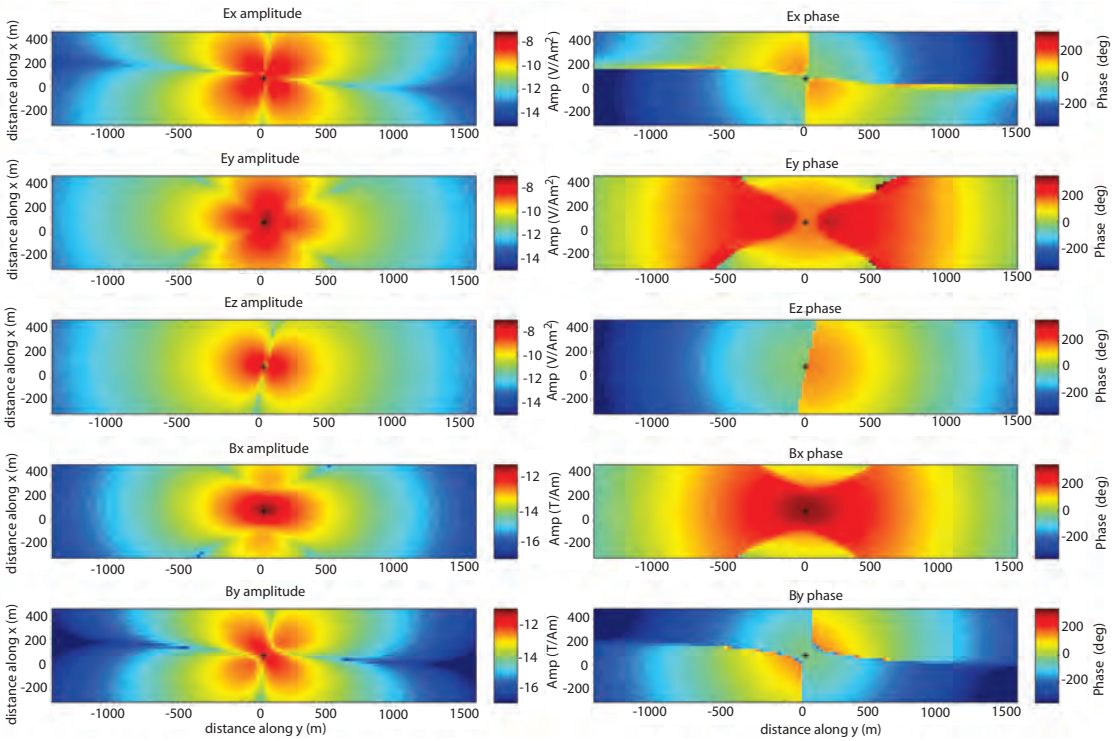


**Figure 5.5**: Electric and magnetic field amplitude and unwrapped phase for a grid of horizontal electric dipole transmitters that are transmitting a frequency of 5 Hz into a 1 Ωm seafloor half-space consisting of transmitters with a rotation of 100° and no transmitter dip.

Changing the rotation simply rotates the features observed in Figure 5.4. For example, Figure 5.5 shows a model for a transmitter rotation of 100°. Notice that the zero crossing point in the $E_x$ and $B_y$ phases are more complex, with jumps in phase that cannot be unwrapped. The zero crossing points are also skewed. This is important if one were to select a profile, say, along $x = 200$ m.

Finally, a transmitter dip of -20° and rotation of 100° is modeled (shown in Figure 5.6). The amplitudes are no longer symmetric and fall off more rapidly on the west side ($x <$ -5500 m) for $E_x$ and $E_y$, but fall off more slowly for the $B_x$, $B_y$, and $E_z$ components here. This asymmetry in amplitude could easily be mistaken for geologic structure on the east or west side of the instrument if "ideal"

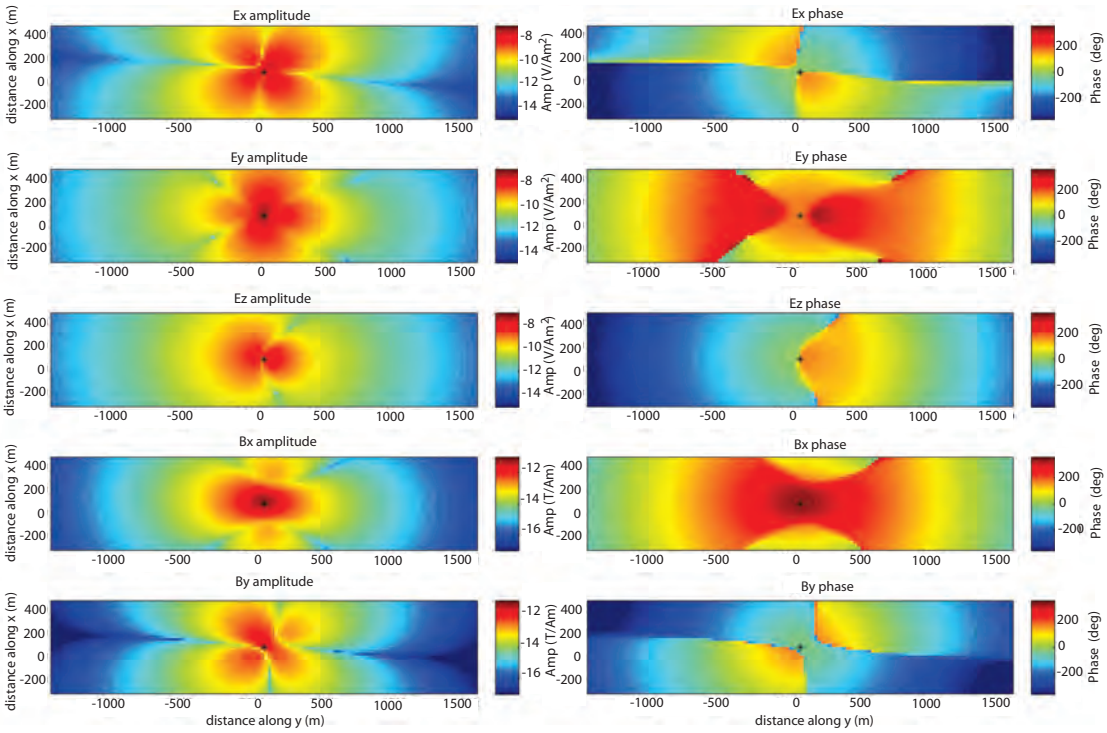


**Figure 5.6**: Electric and magnetic field amplitude and phase for a grid of horizontal electric dipole transmitters that are transmitting a frequency of 5 Hz into a 1 Ωm seafloor half-space with a transmitter rotation of 100° and a dip of -20°.

antenna orientation was assumed (90° transmitter rotation and 0° transmitter dip).

Figure 5.7 and Figure 5.8 are examples of $E_{x,y}$, $B_{x,y}$ and $E_{x,y,z}$ CSEM data, respectively, for profiles along $y$ for different transmitter models, chosen to match features observed in the real data (open circles). In Figure 5.7 the transmitter is about 100 m north of the MT instrument with an antenna rotation of 90° and dip of 0° (dashed lines) and an antenna rotation of 105° with -20° dip (solid lines). The latter model matches the observed data better: notice the $E_x$ phase jump at the closest approach of the transmitter to the receiver (at $y$=5400 m), the width of the $E_y$ phase jumps and their general shape, the cusps in the $B_y$ amplitude, and the cusp in the $B_x$ phase. The $E_x$ and $E_y$ amplitude data saturate, and do not match the synthetic model at close ranges. However, the phases in this region

are usable because they are not affected by amplifier saturation.

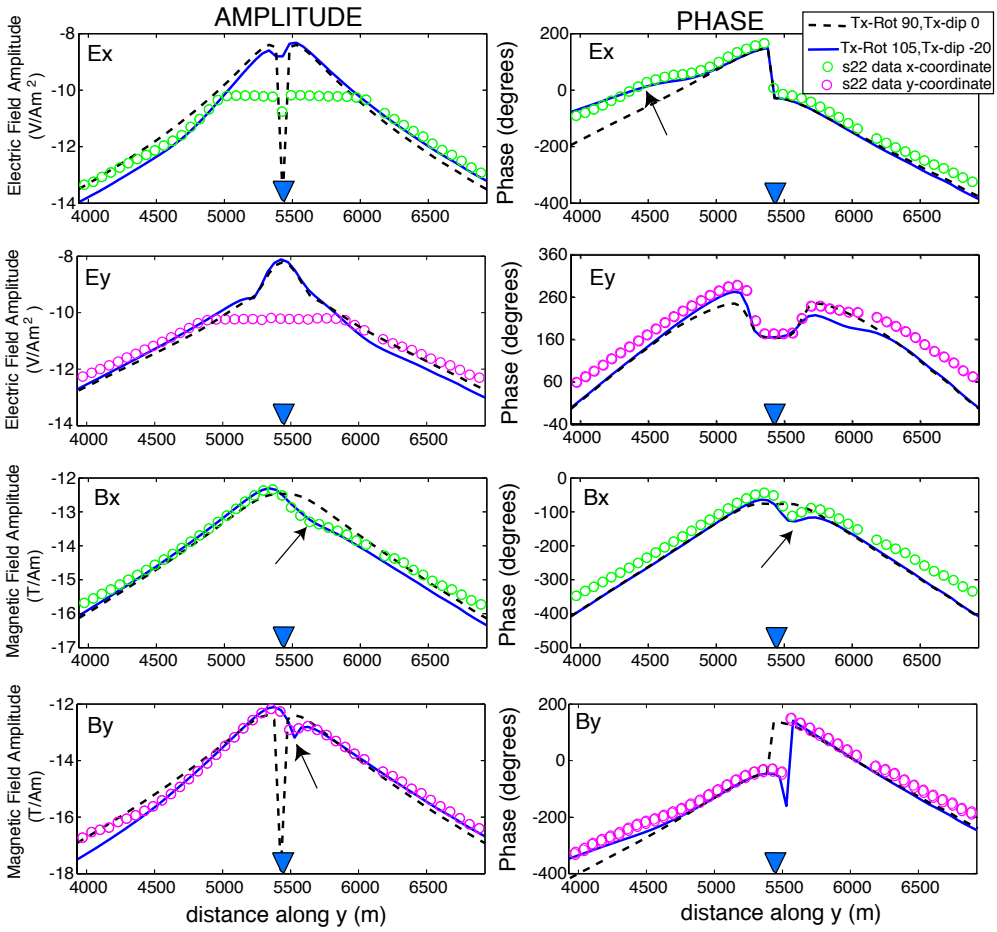


**Figure 5.7**: Example comparison of field data to a 1D forward model of electric and magnetic fields for a transmitter rotation of 105° and a dip of -20° at receiver site 22 (solid line). The dashed line is for a horizontal transmitter with a rotation of 90°. Electric field amplitudes saturate at about $10^{-10}$ V/Am$^2$ (left panel). Unwrapped phases are plotted in the right panel. Open circles are the field data. The arrows show where transmitter orientation and dip are affecting the EM data.

In Figure 5.8 the transmitter is 150 m north of an $E_{x,y,z}$ receiver. An antenna rotation of 80° and a dip of -20° best fits these field data. The inflections in the $E_x$ phase are well represented by this model.

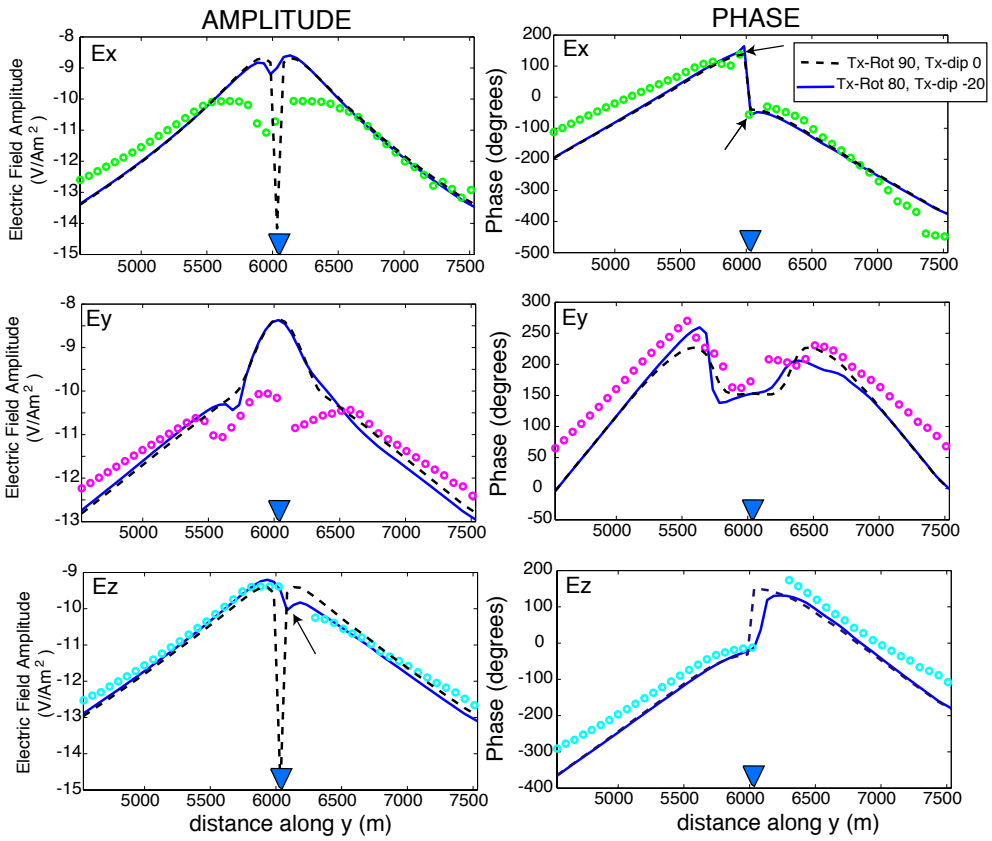


**Figure 5.8**: Example of a 1D forward model for a vertical electric field instrument at site 23. The amplitudes saturate at about $10^{-10}$ V/Am$^2$. A model for a transmitter rotation of 90° and a dip of 0° is given as a reference (dashed lines). Amplitude and unwrapped phase are plotted. Open circles are the field data.

These two representative forward models show that the short range data are sensitive to antenna geometry and that the geometry changes from instrument to instrument due to external forces such as ocean currents, changes in deep-tow wire length, etc. Discrepancies between the forward model and the data in Figures 5.8 and 5.7 are largely due to the assumptions of constant antenna rotation and dip, and the fact that we have not varied the antenna $x$ coordinate, seafloor resistivity or receiver position. However, adding this additional complexity to the transmitter geometry and trying to fit all the receiver data simultaneously is well beyond trial and error forward models.

## 5.3 Marquardt Inversion

A Marquardt inversion, also called ridge regression or maximum neighborhood method, is an algorithm for the nonlinear least-squares estimation of parameters based on an optimum interpolation between the Taylor series expansion and gradient methods (Marquardt, 1963). The predicted response, $\hat{\mathbf{d}}$, to be fitted to the $M$ data, $\mathbf{d}$, is given by

$$\hat{\mathbf{d}} = (\hat{d_1}, \hat{d_2}, \hat{d_3}, ..., \hat{d_M}) = f(\mathbf{x}, \mathbf{m}) \qquad (5.1)$$

where $\mathbf{x}$ is the measurement system or independent data variables associated with the predicted response (e.g. frequency, depth, transmitter altitude, positions, etc.), and $\mathbf{m}$ are the model parameters (e.g. transmitter rotation, dip, half-space apparent resistivity, etc.). The field data collected have errors associated with them:

$$\varsigma = (\varsigma_1, \varsigma_2, \varsigma_3, ..., \varsigma_M). \qquad (5.2)$$

The measure of how well a model $\mathbf{m}$ fits the data is usually given by the sum-squared misfit:

$$\chi^2 = \sum_{k=1}^{M} \left( \frac{d_k - \hat{d}_k}{\varsigma_k} \right)^2 \qquad (5.3)$$

$$= \sum_{k=1}^{M} \frac{1}{\varsigma_k^2} [d_k - f(x_k, \mathbf{m})]^2. \qquad (5.4)$$

In the least squares method $\chi^2$ is minimized with respect to all the model parameters simultaneously by differentiating and setting to zero. When the forward model response $f$ is nonlinear it can be approximated by a Taylor series expansion of $f$ around an initial model guess $\mathbf{m_0}$:

$$\hat{d}_k = f(x_k, \mathbf{m_0} + \triangle\mathbf{m}) \approx f(x_k, \mathbf{m_o}) + \sum_{j=1}^{N} \frac{\partial f(x_k, \mathbf{m_0})}{\partial m_j} \delta m_j \qquad (5.5)$$

where

$$\triangle\mathbf{m} = (\delta m_1, \delta m_2, ...., \delta m_N) \qquad (5.6)$$

is a model parameter perturbation. This approximation for $f$ is substituted into Equation 5.4, which is then minimized with respect to all the model parameters

to give:

$$\beta = \triangle \mathbf{m} \alpha \tag{5.7}$$

where

$$\beta_i = \sum \left( \frac{1}{\varsigma_k^2} [d_k - f(x_k, \mathbf{m_0})] \right) \frac{\partial f(x_k, \mathbf{m_0})}{\partial m_i} \tag{5.8}$$

and

$$\alpha_{ji} = \sum \frac{1}{\varsigma_k^2} \frac{\partial f(x_k, \mathbf{m_0})}{\partial m_j} \frac{\partial f(x_k, \mathbf{m_0})}{\partial m_i}, \tag{5.9}$$

often called the curvature matrix.

The partial derivative matrix $J_{k,j} = \partial f(x_k, \mathbf{m_0}) / \partial m_j$ is the Jacobian matrix relating model perturbations to variations in the data around a model guess $\mathbf{m_0}$. The Jacobian matrix in this application is evaluated by a central difference method because we are unable to solve for it analytically.

The linearization described so far is efficient in a region close to a minimum in $\chi^2$ but often diverges far from the solution (Bevington and Robinson, 2003). To compensate for this behavior, Marquardt suggested that one increase the diagonal terms of the curvature matrix by a factor of $\lambda$ (Bevington and Robinson, 2003; Marquardt, 1963):

$$\alpha_{ji} = \alpha_{ji}(1 + \lambda) \text{ for } j = i$$
$$\alpha_{ji} = \alpha_{ji} \text{ for } j \neq i;$$

which for small $\lambda$ reduces to the solution derived from the Taylor series expansion. For large $\lambda$ the diagonal terms dominate and the method reduces to a gradient algorithm that chooses a path in the direction of maximum reduction in $\chi^2$ (the method of steepest descent). The gradient algorithm is robust to nonlinearity but is very inefficient in the parabolic region near the solution. The recipe adapted from Bevington and Robinson (2003) is:

1. compute $\chi^2(\mathbf{m_0})$
2. start with $\lambda$ small, say 0.00001
3. compute $\triangle\mathbf{m}$ and $\chi^2(\mathbf{m_0} + \triangle\mathbf{m})$ for this $\lambda$
4. If $\chi^2(\mathbf{m_0} + \triangle\mathbf{m}) > \chi^2(\mathbf{m_0})$ increase $\lambda$ by 10, discard $\mathbf{m_0} + \triangle\mathbf{m}$ and go to 3
5. Else if $\chi^2(\mathbf{m_0} + \triangle\mathbf{m}) < \chi^2(\mathbf{m_0})$, decrease $\lambda$ by 10, keep $\mathbf{m_0} + \triangle\mathbf{m}$ as the new model and go to 3.

The limitation on the Marquardt inversion is that it requires a reasonable starting guess for $\mathbf{m_0}$. However, we found that if starting parameters based on our simpler modeling are used the algorithm will generally provide a viable solution to the navigation problem. The error associated with each of the model parameters can be computed from the error matrix, $\varepsilon$, the inverse of the final value of the curvature matrix, $\alpha$:

$$\varepsilon = \alpha^{-1} \qquad (5.10)$$

which is then scaled by the residual variance (final RMS misfit value, see Equation 5.14).

### 5.3.1 Marquardt Inversion for Navigational Parameters

A Marquardt inversion algorithm was written to invert for transmitter and receiver navigational parameters (antenna dip, rotation, $T_x$, $T_y$; receiver $R_x$, $R_y$, $R_{rot}$) based on short-range electric and magnetic field data recorded at seafloor receivers. The program is written in Matlab and calls the external Fortran program *Dipole1D* for the forward model and Jacobian calculation. The main calling program $Totalfield Nav.m$ requires a number of inputs:

1. **Data input:** data vector, $d_k$, of real and imaginary components of $E_x$, $E_y$, $E_z$, $B_x$, $B_y$ for ranges $< 1500$ m, an error vector, $\varsigma_k$, associated with each of these, and an index matrix, $dp_k$, that indentifies the data type, site number, transmitter index, and if it is a real or an imaginary component.

2. **Transmitter model input:** the number of nodes (see below) and the parameters solved at each node: transmitter $x$, $y$, and antenna dip and rotation (all optional) and the step size for the central differencing.

3. **Receiver model input:** the number of receivers and associated parameters to be solved for: receiver $x$, $y$, rotation (all optional) with corresponding step size for central differencing.

4. **Half-space resistivity model input:** An initial half-space resistivity estimate.

5. **x input:** frequency, depth, altimeter height, and model parameters that are held fixed rather than allowed to vary.

Items 2 to 4 above (but not the central difference step) are put into the initial model vector $\mathbf{m_0}$. $Totalfield Nav.m$ computes the first forward model with the current input parameters using the *Dipole1D* Fortran code. To do this the 1D model is initialized for the resistivity of the air, sea, and sediment; the transmitter positions, rotation, and dip are linearly interpolated between nodes to makes the runfile needed for the Fortran *Dipole1D* code, which is then called. After computation the output from *Dipole1D* is read, the modeled electromagnetic responses $\hat{d}_k$ relevant for comparison with the field data are selected, and the residuals

$$\text{residuals} = \left( \frac{d_k - \hat{d}_k}{\sigma_k} \right) \qquad (5.11)$$

are computed. After the first forward model is computed, the Marquardt function is called. The Jacobian matrix is constructed in a similar way by perturbing the model parameters and the Marquardt algorithm is then used to update $\mathbf{m_0}$. This is repeated until convergence, or until the specified maximum number of iterations or maximum number of increases to $\lambda$ are reached.

Transmitter model parameters are linearly interpolated between nodes. The length of the model $\mathbf{m}$ in equation 5.1 can vary depending upon which model

parameters are inverted and how many nodes are used to represent the transmitter geometry. Several receiver positions must be fixed to prevent the coupled motion of transmitter and receiver positions (i.e. drift of the entire coordinate system). The model parameters can consist of transmitter $x$, $y$, rotation, and dip ($Tx_n$, $Ty_n$, $Trot_n$, $Tdip_n$, where $n$ is the node number); receiver position $x$ and $y$; receiver rotation ($Rx_s$, $Ry_s$, $Rrot_s$, where $s$ is the site number); and a single half-space seafloor resistivity ($\rho$). Thus $\mathbf{m}$ can be represented as:

$$\mathbf{m} = (Tx_1, Ty_1, Trot_1, Tdip_1, ..., Tx_n, Ty_n, Trot_n, Tdip_n, Rx_s, Ry_s, Rrot_s, ..., \rho) \quad (5.12)$$

or:

$$\mathbf{m} = (m_1, m_2, ..., m_N) \quad (5.13)$$

where $N$ is the total number of model parameters.

The program run-time depends on how many model parameters are inverted and the number of nodes used. In general, convergence can be obtained within 10 hours or less on an 3 GHz Intel Macintosh using 10-15 iterations.

## 5.4 Application to Hydrate Ridge

The application of the Marquardt Navigation inversion program to the Hydrate Ridge data required the assumption of a constant seawater depth of 1000 m. The Hydrate Ridge tow 1 comprises 253 transmitter positions (about a 70 m spacing). However, as previously mentioned, the transmitter positions are parameterized by discrete nodes, and transmitter geometries linearly interpolated between nodes to force a smooth transmitter path and reduce computation time. Two different node cases are considered: an 18 node (every $14^{th}$ transmitter position) and an 8 node (every $35^{th}$ transmitter position) parameterization.

The step sizes used in the central difference calculation are 10 m for positions in $x$ and $y$; 1° for transmitter dip and rotation and receiver rotation; and 0.1 Ωm for resistivity. The **x** consists of the frequency (5 Hz), depth (1000 m), transmitter altitude (from altimeter recordings collected during the experiment), and fixed model parameters not included in **m**.

The data, **d**, used are the real and imaginary components of the electric and magnetic fields at ranges <1500 m, giving a total of 4876 data points. Real and imaginary components of the data are used to remove the difficulty in unwrapping phases, which can result in residuals offset by factors of 360°. However, the use of real and imaginary components of the fields required the construction of a way to deal with saturated amplitudes. When amplitudes are saturated a fake amplitude of 1 is used to compute the real and imaginary components from phase data.

Typically, the noise floor (detection threshold) is $10^{-15}$V/Am$^2$ for electric fields and $10^{-17}$T/Am for magnetic fields and is representative of the background magnetotelluric signal and the noise in the receiving equipment. Above the detection threshold noise can be considered more or less proportional to the signal strength and associated with random errors in transmitter and/or receiver geometry (Flosadóttir and Constable, 1996). Systematic errors may also occur, for example, in the absolute phase of the transmitter. Other sources of error above the detection threshold that cause data scatter may be near-surface geologic and topographic features that the conductivity model may be unable to describe in detail ('geologic noise') (Cox et al., 1986; Evans et al., 1994). Data used in our Marquardt inversion are from short ranges where the data are above the instrument noise floor, and so a 10% error in amplitude is assigned to account for the random and geologic noise and is applied to the real and imaginary components equally. The errors for the real and imaginary components of the saturated data are also taken to be 10% of the amplitude.

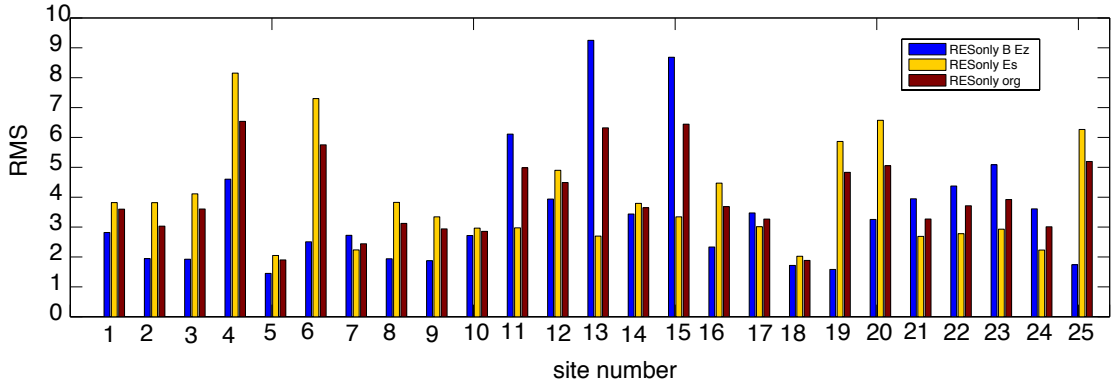


**Figure 5.9**: RMS misfit for Marquardt inversions solving only for half-space resistivity using three different types of data available for each site: only magnetic or only vertical electric field data shown in blue (odd numbered sites are vertical electric fields, even numbered sites are magnetic field sites), only the horizontal electric field data (yellow); and all of the data available at each site (dark red).

The $TotalfieldNav.m$ program was initially tested by using different combinations of single site data to solve for just seafloor resistivity at each site. All available data, only the horizontal electric fields, and either only the vertical electric fields or only horizontal magnetic fields (depending how the site was configured) were inverted. The RMS misfit is given by:

$$\text{RMS} = \sqrt{\frac{\chi^2}{M}} \qquad (5.14)$$

where $M$ is the total number of data. Figure 5.9 shows the RMS misfit for each of these cases. These values are much larger than 1.0 (the expected value) because no navigational parameters for the transmitter or receiver have been included in these inversions.

The different data types generally provide similar estimates for resistivity except for specific cases of using vertical electric field data (Figure 5.10). In general the resistivity varies in a pattern similar to the first apparent resistivity results

(Weitemeyer et al., 2006c), where the west is more resistive than the east and site 6 has an anomalously lower resistivity.

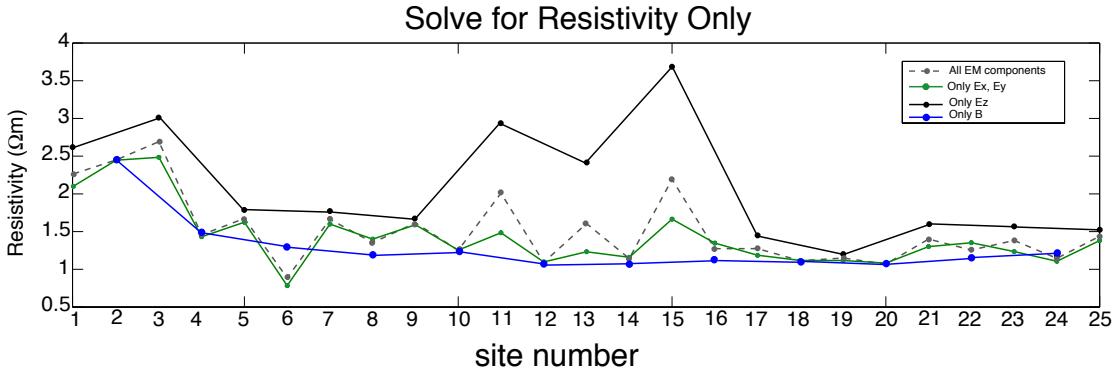


**Figure 5.10**: A resistivity inversion by site using different data types. Vertical electric field data (solid black line) and all data (dashed line) produce larger apparent resistivities than the horizontal only (green line) and magnetic field (blue) only inversions.

The resistivities produced from the different inversions vary especially between sites 10 to 16. The $E_z$ component gives larger half-space resistivity values than using only the horizontal electric field data. The magnetic field data give lower or similar resistivities compared to horizontal electric field data. The influence of the vertical electric fields on the resistivity when using all components of the electric fields is to increase the estimates of seafloor resistivity. This maybe because the dip of the antenna affects $E_z$ the most.

The average of the inverted resistivities was used to estimate a starting value of 1.5 Ωm for a single half-space apparent seafloor resistivity. When solving for transmitter and receiver parameters, model complexity was increased incrementally to see how important each of the parameters were. Figure 5.11 is a bar graph for various inversion runs for both the 8 node and 18 node cases. Allowing the Marquardt inversion program to solve for transmitter rotation and dip or transmitter rotation and receiver position instead of just solving for transmitter rotation lowered the RMS misfit from 7.6 to about 4 (Figure 5.11). Including

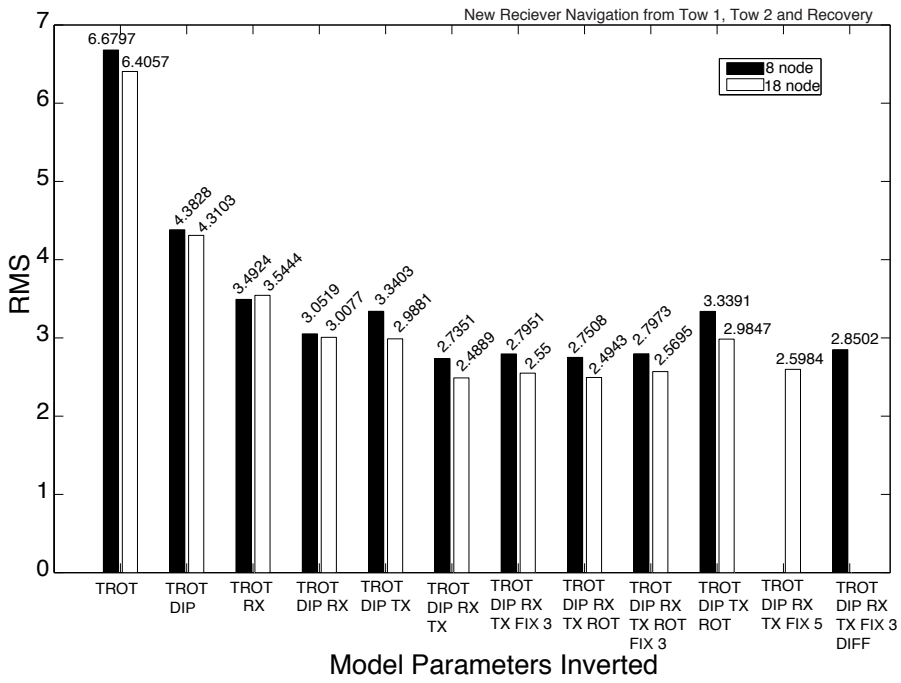


**Figure 5.11**: RMS misfit as a function of model parameters. Abbreviations are: TROT : transmitter rotation, DIP : transmitter dip, RX : receiver $x$, $y$ position, TX : transmitter $x$, $y$ position, ROT : receiver rotation, FIX : fixing a certain number of the receiver positions. DIFF : fixing a different set of receivers. Black bars are the 8 node cases and white bars are the 18 node cases.

either the transmitter $x$, $y$ positions or receiver $x$, $y$ positions dropped the misfit further to about 3. Adding additional degrees of freedom did not significantly improve the RMS misfit further. Fixing a number of the receiver sites in $x$ and $y$ became necessary to decouple transmitter and receiver motion in $x$-$y$ space. The addition of a rotation to the receiver parameters offered no significant improvement to the misfit, suggesting that the rotations are reasonable as estimated from the 2D modeling discussed in Chapter 4. The 18 node case gave only a slightly better RMS misfit and the models for transmitter position, rotation, and dip have oscillatory behavior, suggesting the inversion is fitting noise at this point.

Figures 5.12 and 5.13 are plots of the model parameters computed for the inversions shown in Figure 5.11. A general pattern common to all models emerges

for the rotation and dip of the transmitter for both nodal cases. Notice that when solving for the transmitter and all receiver positions simultaneously, the transmitter and receiver positions begin to move jointly. It is also clear that the 18 node case gives a irregular model for the transmitter parameters as compared to the 8 node case, often giving unreasonable transmitter dips and rotations. Most of the models diverge from one another at the first and final nodes. The 8 node models were preferred over the 18 node models as they are smoother.

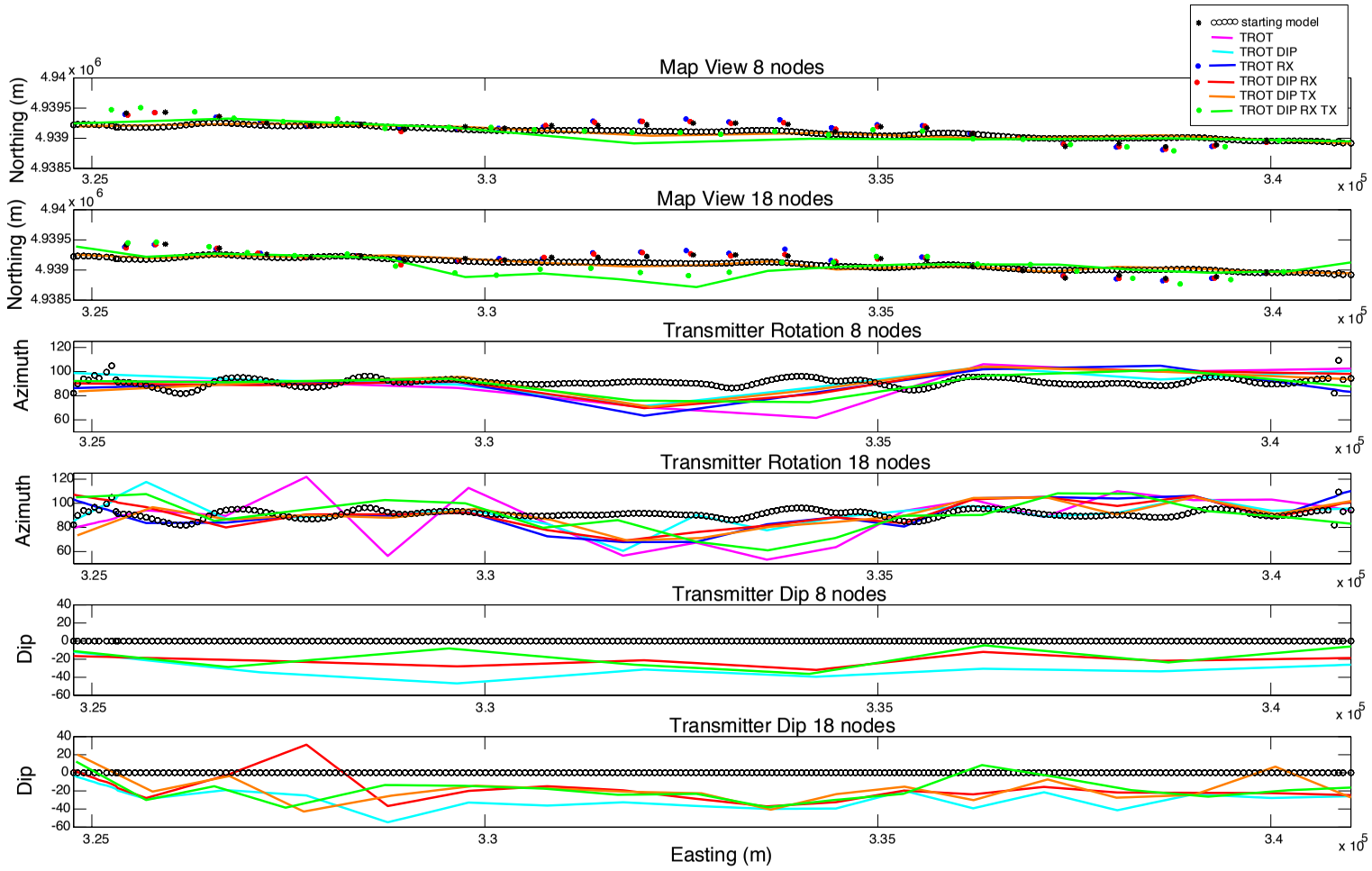


**Figure 5.12**: Map view of transmitter and receiver positions, transmitter rotation, and dip for the 8 node and 18 node models when inverted for rotation (TROT), rotation and dip (TROT DIP), rotation and receiver position (TROT RX), rotation, dip and receiver position (TROT DIP RX), rotation, dip and transmitter position (TROT DIP TX), rotation, dip, receiver and transmitter position (TROT DIP RX TX).

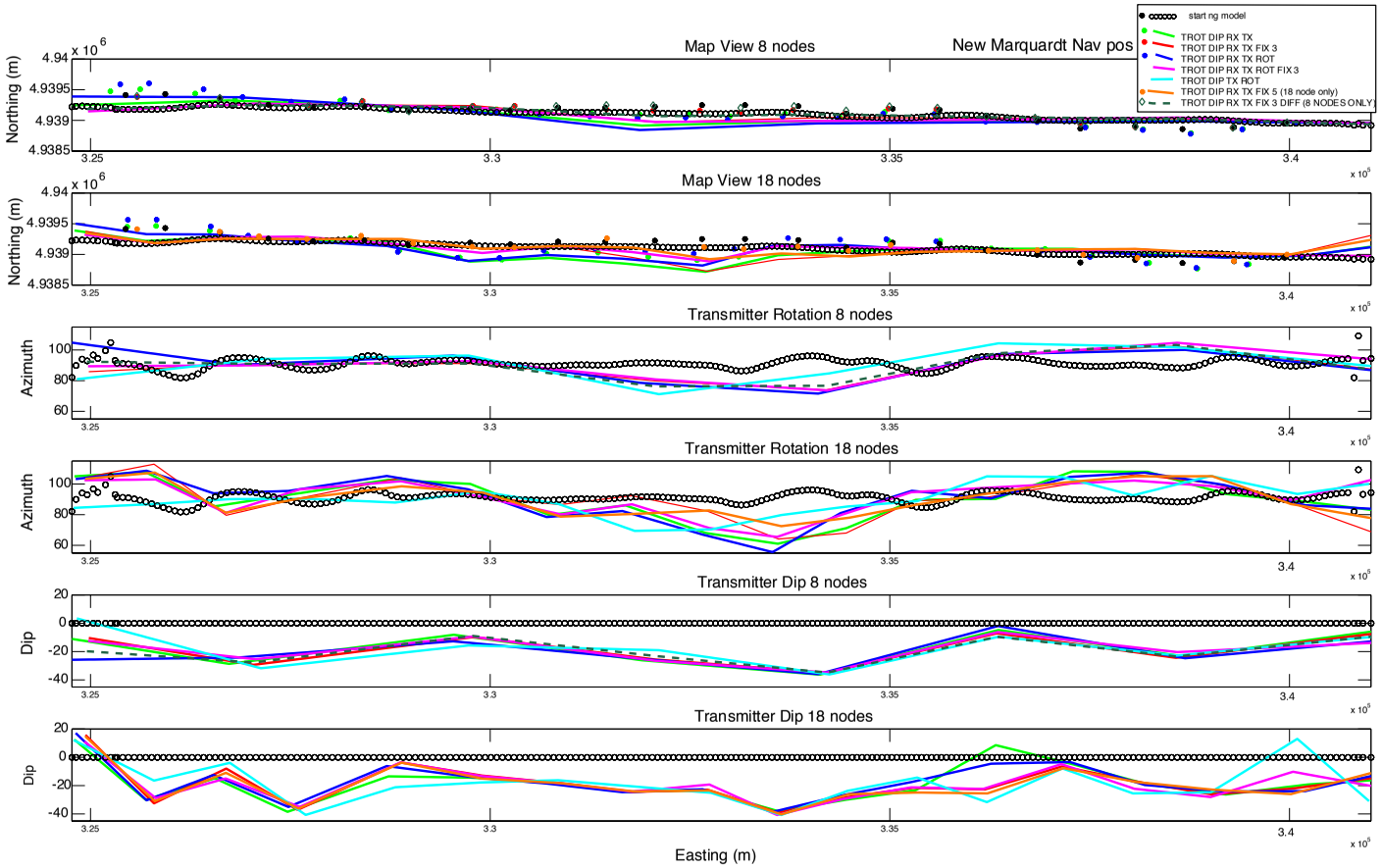


**Figure 5.13**: Map view of transmitter and receiver positions, transmitter rotation and dip for the 8 node and 18 node models when inverting for rotation, dip, receiver and transmitter position (TROT DIP RX TX), rotation, dip, receiver and transmitter position while fixing 3 receiver positions (TROT DIP RX TX FIX 3), rotation, dip, receiver and transmitter position, and receiver rotation (TROT DIP RX TX ROT), rotation, dip, receiver and transmitter position, and fixing 5 receiver positions (TROT DIP RX TX FIX 5 - 18 node case only), rotation, dip, receiver and transmitter position, and fix 3 different receiver postions (TROT DIP RX TX, FIX 3 DIFF - 8 node case only).

### 5.4.1 The Preferred Model

The preferred model is shown in Figure 5.14 and consists of the 8 node transmitter rotation, dip, and position, and with 3 out of 25 receiver positions fixed. The inversion ran to 16 iterations and exited with a converged RMS of 2.79 (given the 10% data noise estimate).

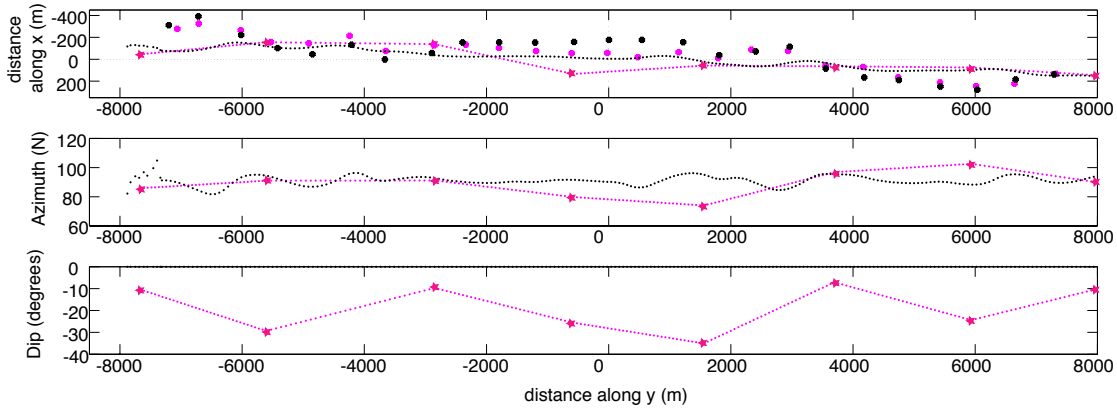


**Figure 5.14**: The preferred model solves for transmitter $x$, $y$, and receiver $x$, $y$ (top), transmitter rotation (second panel), transmitter dip (third panel), with fixed receiver positions at site 2, 10, 23. This model resulted in an RMS misfit of 2.79. Black is the original starting model, magenta is the final model. Magenta stars are the node locations.

The normalized residuals (Figure 5.15) for the preferred model are scattered about 0, most between $\pm 5$ ($M = 4876$ real and imaginary data points and the length of $\mathbf{m}$ is $N = 77$) and the tails (i.e. large residuals) are clustered around given components on given instruments (e.g. $Esat_x$, $Esat_y$ site 6). A normalized histogram of the residuals are shown in Figure 5.16 along with the best-fitting Gaussian probability density function.

The standard error associated with each model parameter is the square root of the diagonal terms of $\varepsilon$ (Equation 5.10) scaled by the residual variance (i.e. multiplied by the final RMS value of 2.79). The errors are given in Table

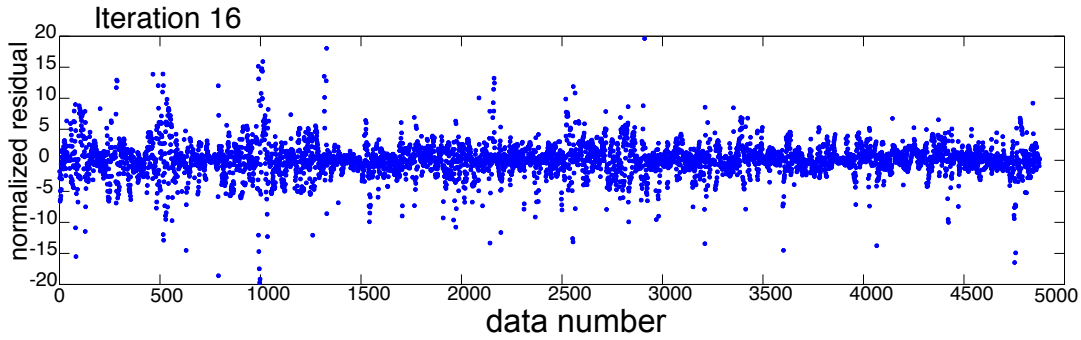


**Figure 5.15**: Normalized residuals for the final, $16^{th}$, iteration versus data point. The error floor is 10%.

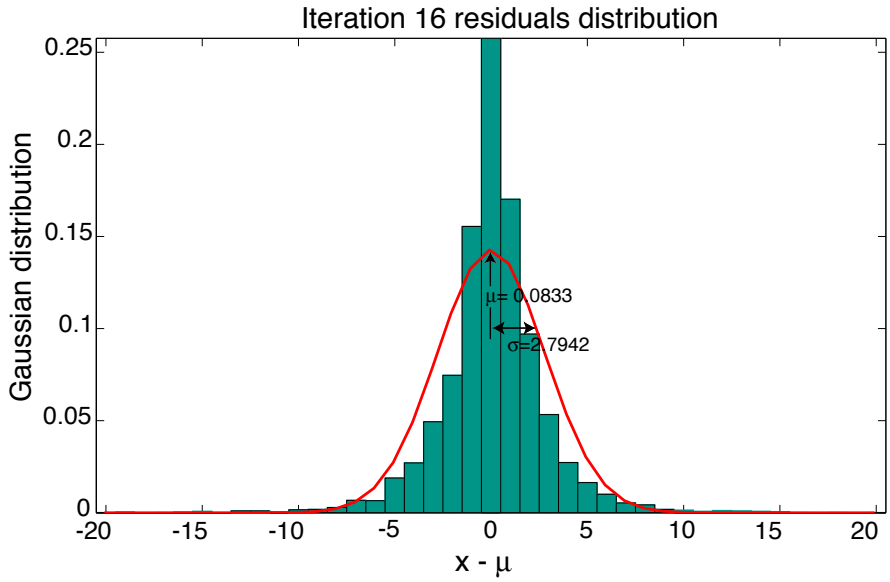


**Figure 5.16**: A normalized probability density function for the residuals and the best fitting Gaussian of the final iteration for the preferred model.

5.1 for the transmitter parameters and Table 5.2 lists the error for the receiver model parameters. The error of the final half-space seafloor resistivity (1.361 Ωm) is 0.008 Ωm, but since seafloor resistivity may vary along the profile, this must be interpreted as an error in the average resistivity.

**Table 5.1**: Final transmitter positions ($x$,$y$), rotation and dip at the nodal points with associated standard error.

| **Node** # | **Northing** UTM | **X** (meters) | $\varsigma_X$ | **Easting** UTM | **Y** (meters) | $\varsigma_Y$ | **Rotation** degrees | $\varsigma_{rotation}$ | **Dip** degrees | $\varsigma_{dip}$ |
|---|---|---|---|---|---|---|---|---|---|---|
| 1 | 4939149.8 | 45.5 | 6.5 | 324978.2 | -7666.6 | 6.1 | 85.8 | 1.5 | -10.4 | 2.0 |
| 2 | 4939260.1 | 155.8 | 1.5 | 327039.4 | -5605.4 | 7.4 | 91.0 | 0.1 | -29.4 | 1.3 |
| 3 | 4939242.0 | 137.7 | 2.1 | 329792.3 | -2852.5 | 7.1 | 91.2 | 0.2 | -9.7 | 1.9 |
| 4 | 4938969.8 | -134.5 | 8.1 | 332063.4 | -581.4 | 6.8 | 79.8 | 1.0 | -25.6 | 1.2 |
| 5 | 4939046.7 | -57.6 | 6.9 | 334202.1 | 1557.3 | 7.4 | 74.0 | 0.5 | -35.0 | 0.9 |
| 6 | 4939039.7 | -64.6 | 3.3 | 336338.4 | 3693.6 | 8.4 | 96.8 | 0.5 | -7.1 | 1.9 |
| 7 | 4939029.0 | -75.3 | 2.6 | 338580.3 | 5935.5 | 5.6 | 102.6 | 0.6 | -24.4 | 1.5 |
| 8 | 4938943.7 | -160.6 | 3.0 | 341053.1 | 8408.3 | 16.1 | 87.4 | 0.3 | -7.3 | 3.9 |

**Table 5.2**: Final receiver positions ($x$,$y$) and associated standard error.

| **Site** # | **Easting UTM** | **Y** (meters) | $\varsigma_Y$ | **Northing UTM** | **X** (meters) | $\varsigma_X$ |
|---|---|---|---|---|---|---|
| s1 | 325583.8 | -7061.0 | 5.6 | 4939381.3 | 277.0 | 5.9 |
| s3 | 326621.1 | -6023.7 | 4.1 | 4939369.4 | 265.1 | 6.6 |
| s4 | 327114.9 | -5529.9 | 1.9 | 4939261.6 | 157.3 | 7.6 |
| s5 | 327736.4 | -4908.4 | 1.2 | 4939249.4 | 145.1 | 7.9 |
| s6 | 328403.6 | -4241.2 | 5.0 | 4939318.4 | 214.1 | 6.6 |
| s7 | 328995.4 | -3649.4 | 9.2 | 4939179.9 | 75.6 | 5.8 |
| s8 | 329783.4 | -2861.4 | 2.5 | 4939238.6 | 134.3 | 7.0 |
| s9 | 330305.9 | -2338.9 | 2.9 | 4939237.7 | 133.4 | 6.4 |
| s11 | 331456.7 | -1188.1 | 7.1 | 4939179.7 | 75.4 | 6.0 |
| s12 | 332038.7 | -606.1 | 8.6 | 4939159.9 | 55.6 | 6.6 |
| s13 | 332623.4 | -21.4 | 7.8 | 4939162.2 | 57.9 | 6.7 |
| s14 | 333120.6 | 475.8 | 6.7 | 4939123.1 | 18.8 | 7.0 |
| s15 | 333789.0 | 1144.2 | 7.1 | 4939169.3 | 65.0 | 6.9 |
| s16 | 334436.9 | 1792.1 | 6.5 | 4939114.2 | 9.9 | 7.3 |
| s17 | 334980.7 | 2335.9 | 5.6 | 4939192.0 | 87.7 | 6.8 |
| s18 | 335580.6 | 2935.8 | 4.7 | 4939180.1 | 75.8 | 7.8 |
| s19 | 336199.2 | 3554.4 | 2.7 | 4939048.5 | -55.8 | 7.9 |
| s20 | 336809.5 | 4164.7 | 3.3 | 4939034.4 | -69.9 | 7.2 |
| s21 | 337382.9 | 4738.1 | 5.5 | 4938938.8 | -165.5 | 5.7 |
| s22 | 338069.1 | 5424.3 | 3.6 | 4938892.1 | -212.2 | 4.9 |
| s24 | 339287.4 | 6642.6 | 4.6 | 4938882.1 | -222.2 | 7.7 |
| s25 | 339966.3 | 7321.5 | 1.9 | 4938971.2 | -133.1 | 9.3 |

Figures 5.17 to 5.26 show the data and preferred model responses for the $E_x$, $Esat_x$, $E_y$, $Esat_y$, $E_z$, $Esat_z$, $B_x$, $Bsat_x$, $B_y$, and $Bsat_y$ components ($sat$ refers to saturated amplitudes of electric or magnetic field data). Each plot consists of five panels: the first two panels are $\log_{10}$ plots of the absolute value of the real and imaginary components, and the third and fourth panels are plots of amplitude and phase. The final panel shows the residual for real (filled circle) and imaginary (unfilled circle) components at each site. The data from each of the sites are color coded and labeled consistently for all plots.

Looking at the cross-line $E_x$ component in Figure 5.17 and Figure 5.18, the normalized residuals are below $\pm 10$ for data from 750 m range to 1500 m range. The effect of seafloor resistivity is obvious in site 6, previously modeled as having low seafloor resistivity, as this site has the largest residuals. The normalized residuals for $Esat_x$ are within $\pm 20$ and the data represented here are from short ranges $<$750 m largely influenced by the geometry of the transmitter, especially the transmitter rotation and dip. The position of the transmitter in $x$ and $y$ determines on which side of the receiver the transmitter is estimated to be, based on the jumps in phase. Phase jumps of 180° are present in most cases. However, when the transmitter is purely in-line with the receiver, the $E_x$ phase gets very small (site 20). There are also cases where the transmitter crosses the $y$-axis of the receiver several times and multiple 180° phase jumps occur (sites 4, 6, 8, 16, 19, 25).

The in-line $E_y$ component (Figure 5.19) has larger normalized residuals than the $E_x$ (cross-line) components discussed above. Specifically, site 6 and site 3 have larger normalized residuals which are probably due to the a different local seafloor resistivity at these sites. The $Esat_y$ (Figure 5.20) has similar normalized residuals to the $Esat_x$ – within $\pm 20$. The phase of the model response in the saturated cases shows very good agreement with the data, supporting our decision to include it by means of an artificial amplitude.

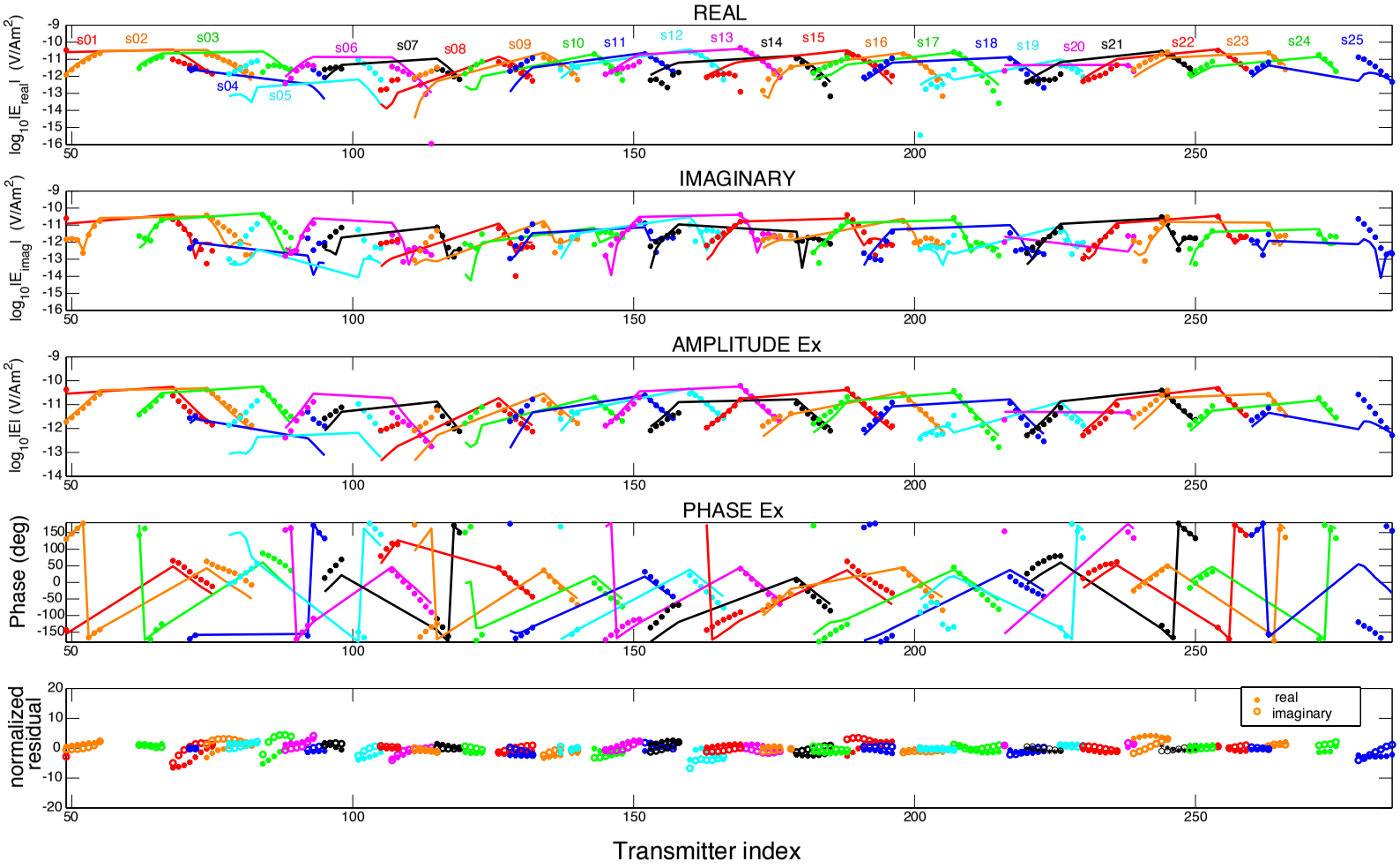


**Figure 5.17**: The cross-line $E_x$ real, imaginary, amplitude, wrapped phase and residual plots versus transmitter index.

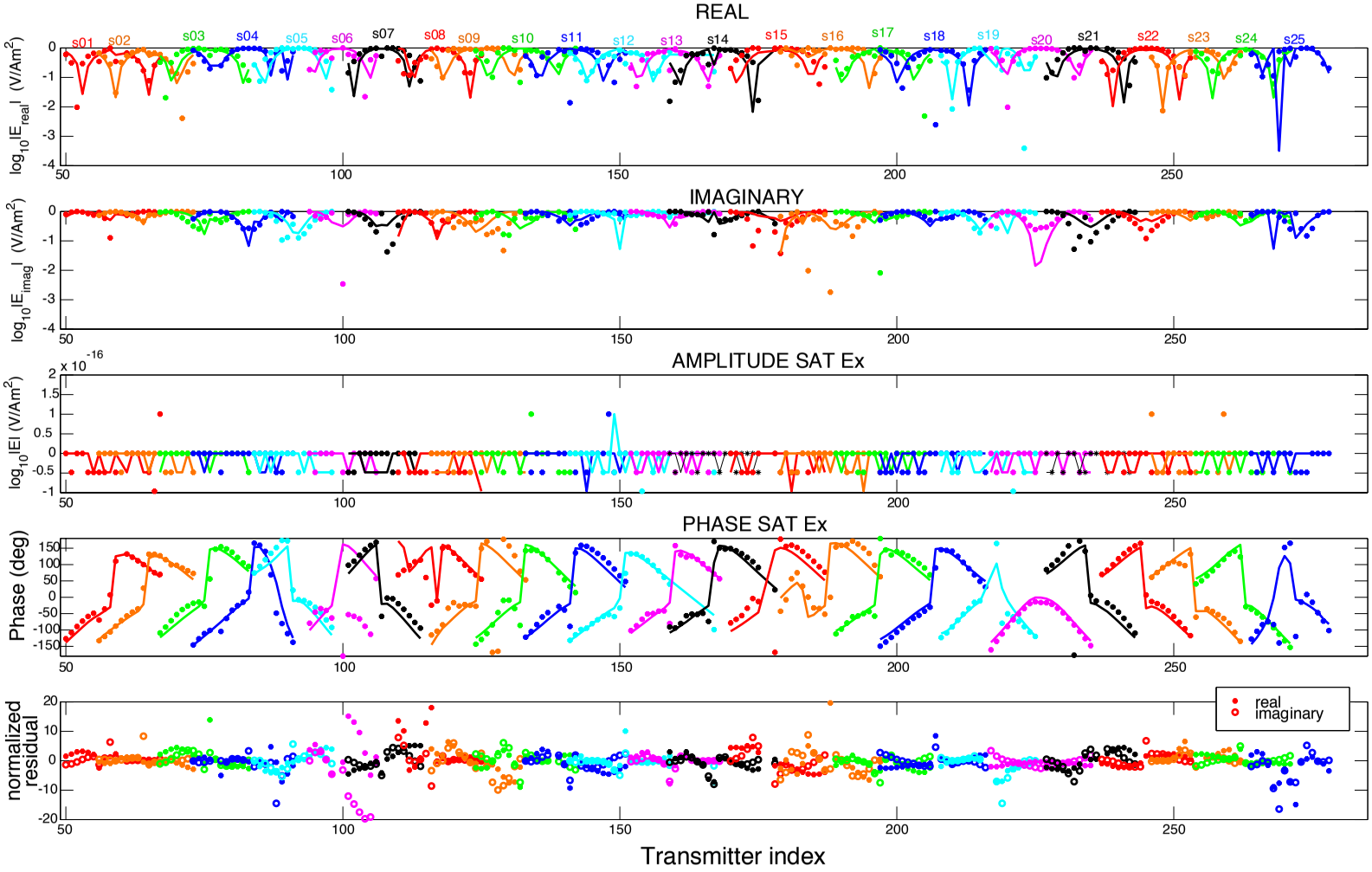


**Figure 5.18**: The cross-line $Esat_x$ real, imaginary, amplitude, wrapped phase and residual plots versus transmitter index.

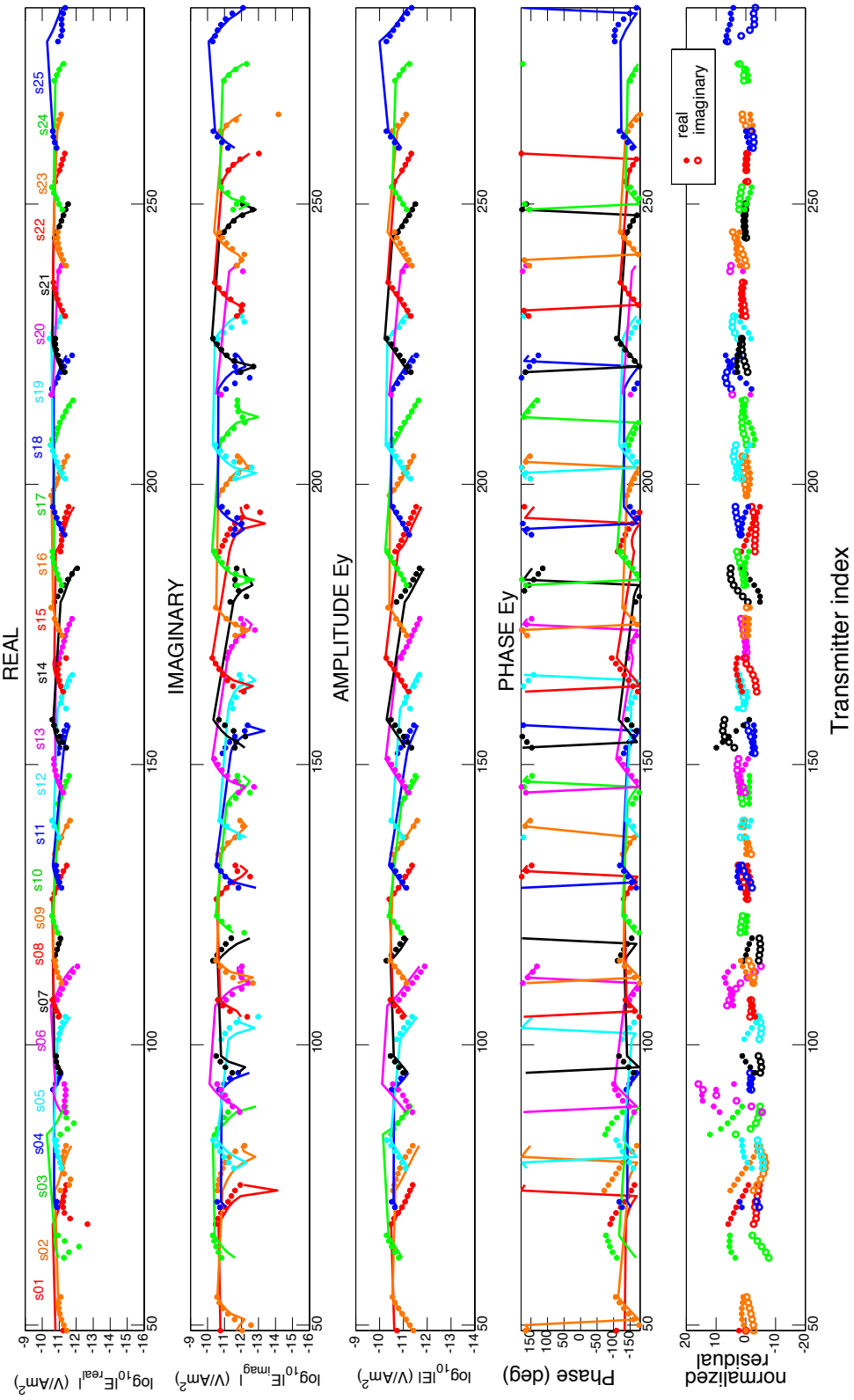


**Figure 5.19**: The in-line $E_y$ real, imaginary, amplitude, wrapped phase and residual plots versus transmitter index.

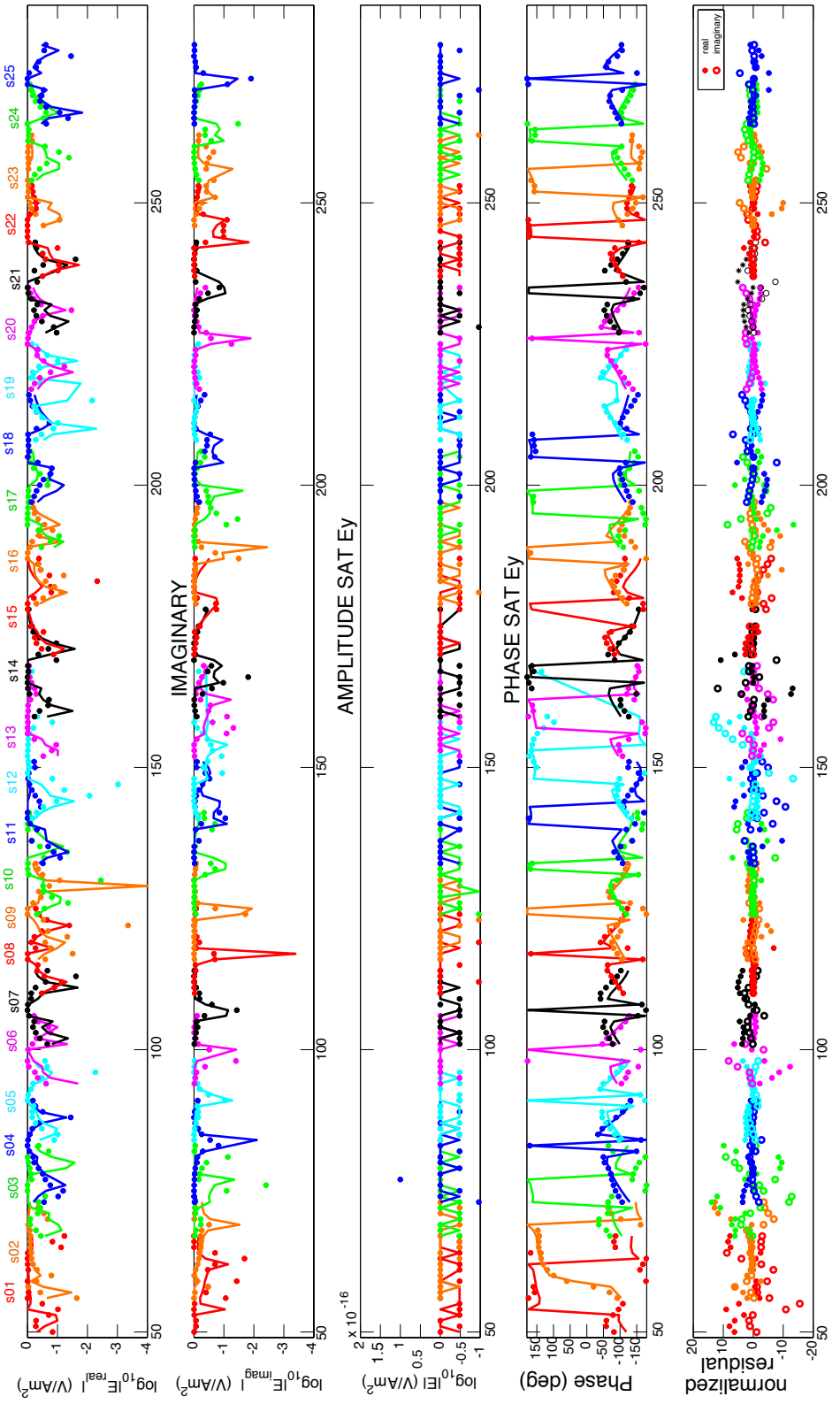


**Figure 5.20**: The in-line $Esat_y$ real, imaginary, amplitude, wrapped phase and residual plots versus transmitter index.

The vertical electric field data $E_z$ are shown in Figure 5.21 and saturated vertical electric field data $Esat_z$ are shown in Figure 5.22. The amplitude data that are not saturated exhibit antisymetric cusps, indicative of a dipping transmitter. The 180° phase jumps appear to be well modeled and the normalized residuals in these two data sets are below ±10.

The cross-line $B_x$, $Bsat_x$, and in-line $B_y$, $Bsat_y$ magnetic field data are well modeled with normalized residuals below ±20. Not all magnetic field sites saturate and this is reflected by the sparsity of data in Figure 5.24 and Figure 5.26. Most of the characteristic cusps in the data are well represented in the $B_x$ plots (Figure 5.23). The cross-line component $B_y$ (Figure 5.25) is also well fit and when the transmitter crosses the $y$ axis of the receiver there are jumps of 180° in phase, which happens at the same sites observed for the cross line $E_x$ component (sites 4, 6, 20).

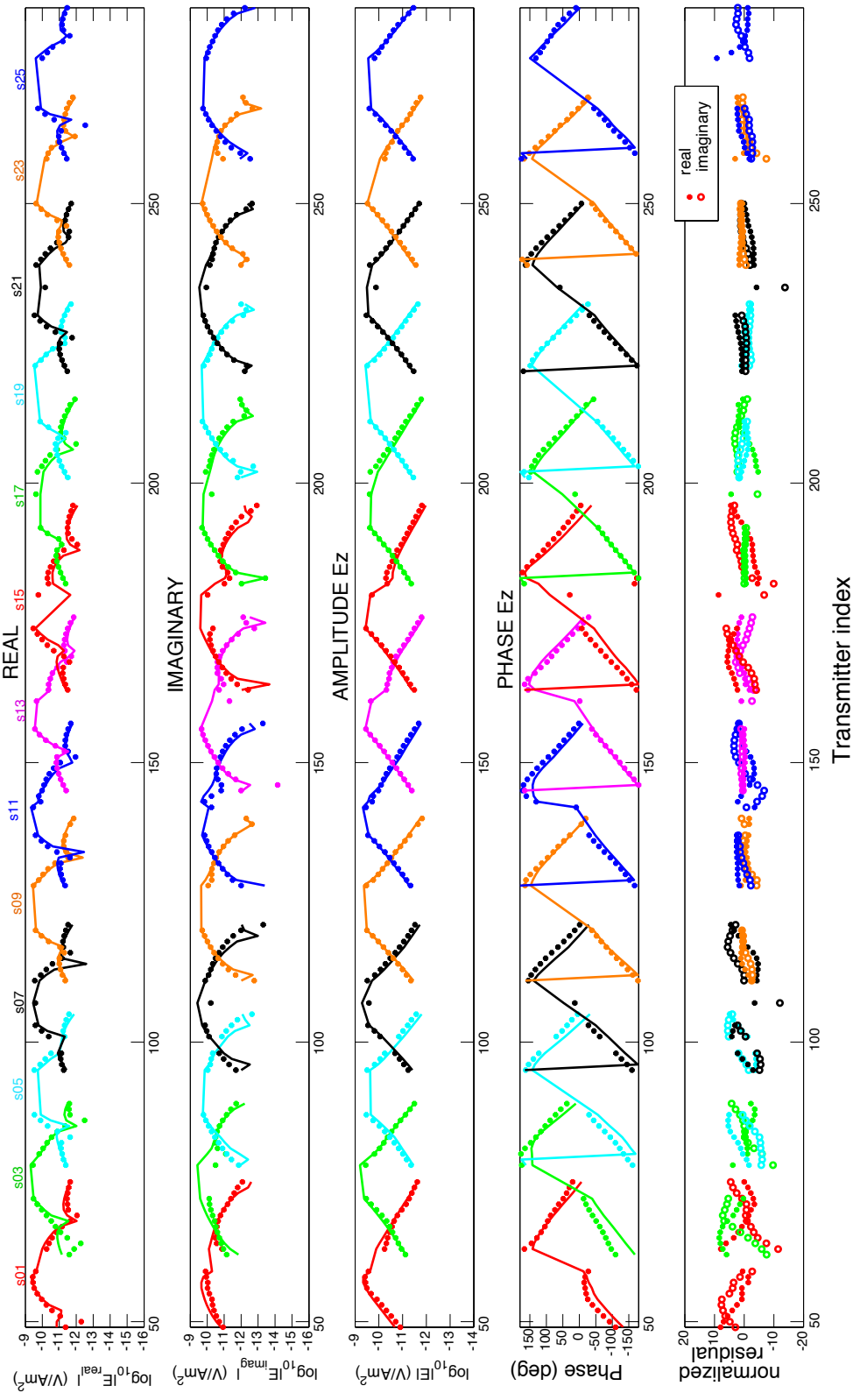


**Figure 5.21**: The inline $E_z$ real, imaginary, amplitude, phase and residual plots versus transmitter index.

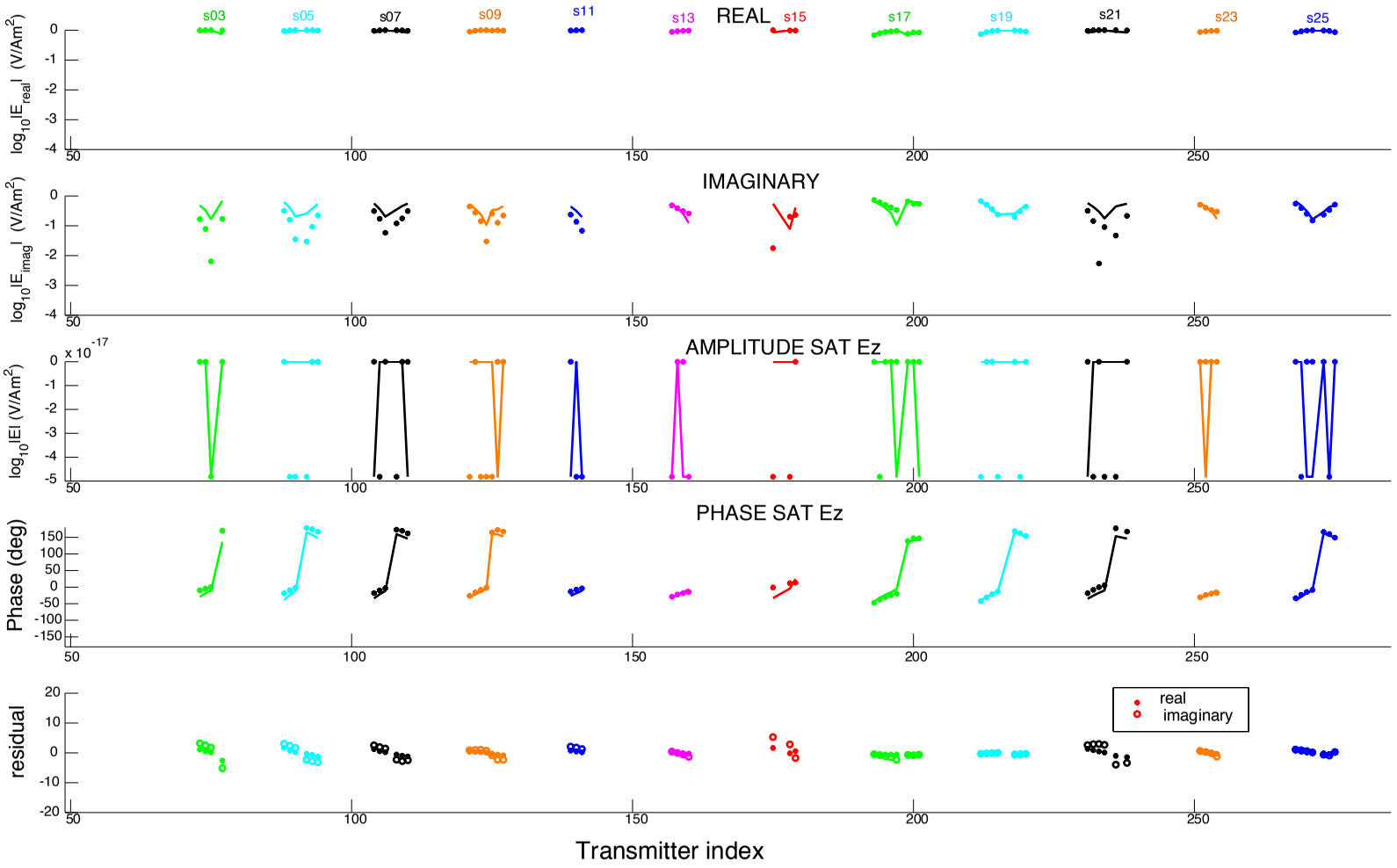


**Figure 5.22**: The inline $Esat_z$ real, imaginary, amplitude, phase and residual plots versus transmitter index.

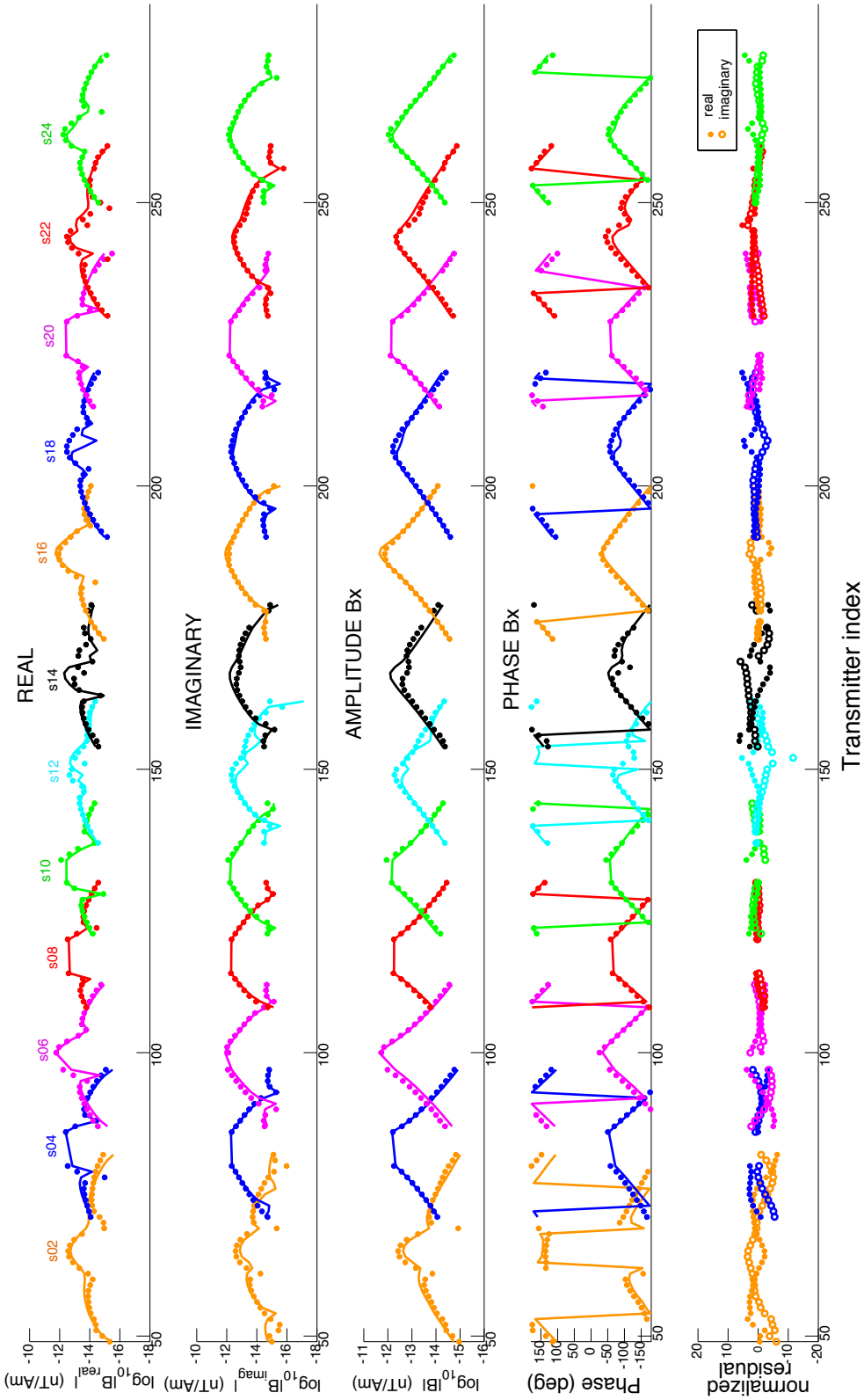


**Figure 5.23**: The cross-line $B_x$ real, imaginary, amplitude, wrapped phase and residual plots versus transmitter index.

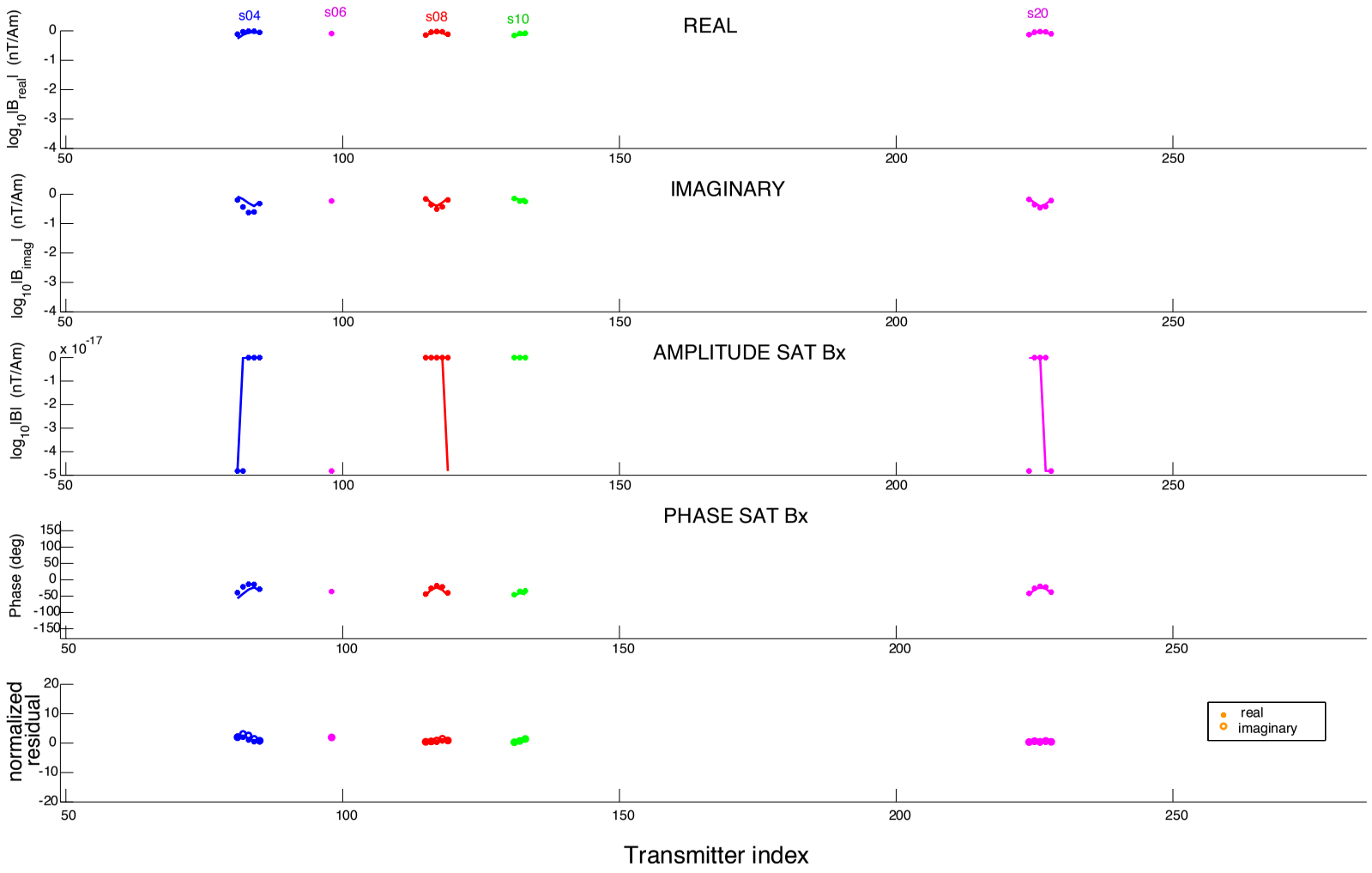


**Figure 5.24**: The cross-line $Bsat_x$ real, imaginary, amplitude, wrapped phase and residual plots versus transmitter index.

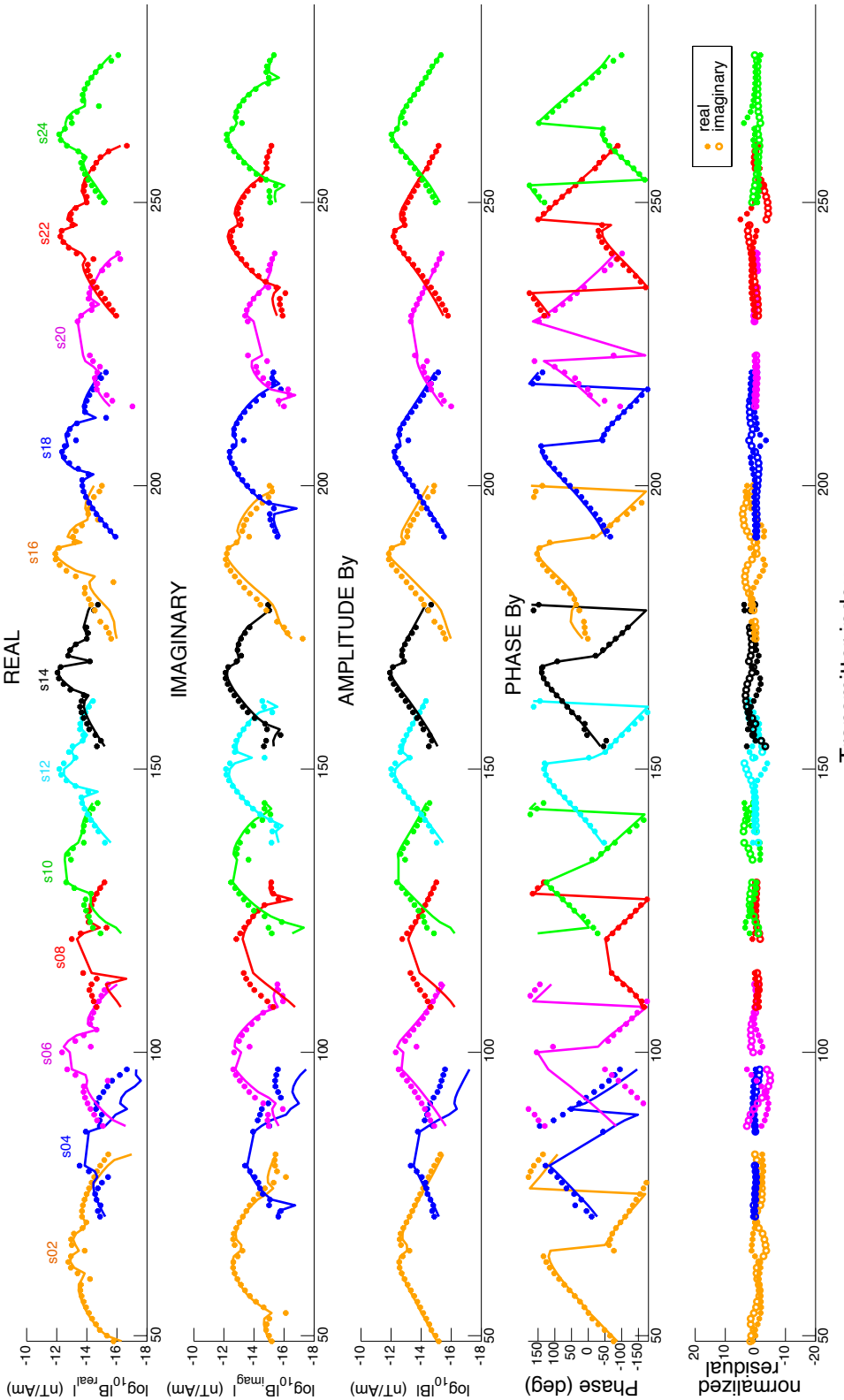


**Figure 5.25**: The in-line $B_y$ real, imaginary, amplitude, wrapped phase and residual plots versus transmitter index.

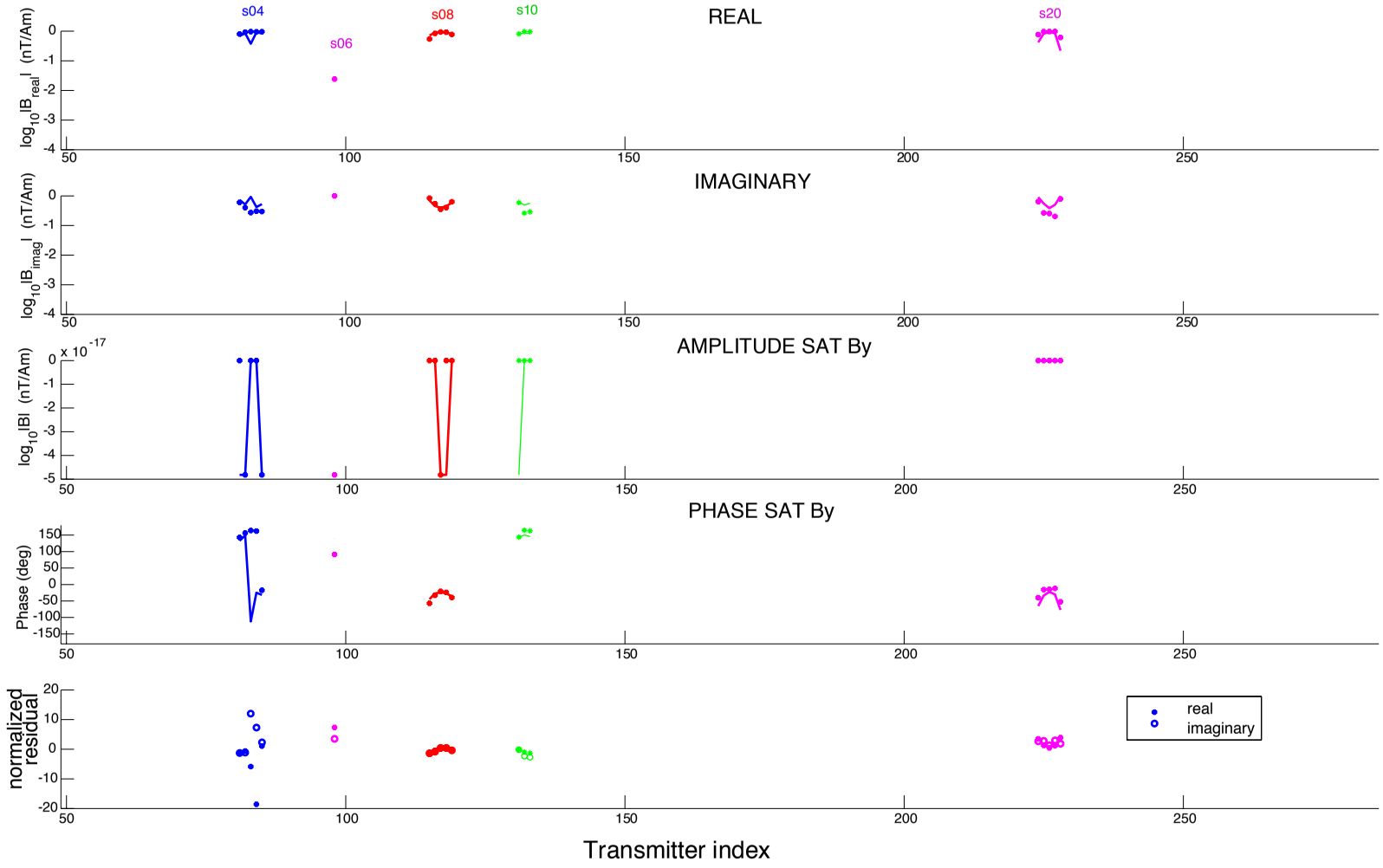


**Figure 5.26**: The in-line $Bsat_y$ real, imaginary, amplitude, wrapped phase and residual plots versus transmitter index.

## 5.5 Conclusions

Our case study using CSEM data collected at Hydrate Ridge demonstrated that a Marquardt inversion of short range electric and magnetic field CSEM data can be used to estimate the transmitter and receiver geometry. Because multiple receivers observe a single transmitter the solution is well constrained. The model requires at least four free parameters to achieve good fits to the data: transmitter rotation, dip, and $x$ and $y$ positions. In our case a model which found the transmitter $x$, $y$, dip, rotation; and 22 out of 25 receiver ($x$, $y$) positions, gave an RMS misfit of about 2.79, with a 10% error associated with each data point. We deem this a reasonable misfit and the model of the transmitter is smooth, with reasonable values for the rotation and dip of the transmitter antenna. While this method is useful to improve navigation in CSEM surveys it also demonstrates the sensitivity of each of the EM components to the geometry of the transmitter, especially at ranges shorter than 750 m.

Improvements to the algorithm can be made to take into account 2D bathymetry by utilizing a 2.5D forward modeling code. This would also provide the ability to solve for resistivity across the profile. The data currently must be given in an absolute orientation for $x$, $y$ and $z$ components of the electric and magnetic fields. An inversion program that accepts unrotated data (i.e. in their individual channels) would eliminate cross contamination of noise from one channel to the other when the data are rotated into an absolute reference frame. The inclusion of higher frequencies would further improve the position of transmitters and receivers. However, geologic noise may have more influence on these data, as the instrument noise floor is reached at the 1.5 km range. To make better interpretations using the $E_z$ data, receiver tilts might have to be included. A linearized error analysis (Tables 5.1 and 5.2) suggests the receiver positions and the transmitter positions are recovered to within about 5 m, and transmitter orientation to 1–2°.

# 6

# 2.5D Model Construction and Validation

## 6.1 Introduction

The next two chapters deal with forward and inverse modeling of the data using 2.5D finite element (FE) and 2.5D finite difference (FD) codes. Two-and-a-half-dimensional (2.5D) forward modeling refers to a 2D earth model excited by a 3D source, eliminating the need to discretize the model along one axis and thus reducing computational costs (Hohmann, 1987; Unsworth et al., 1993). The FD and the FE methods are the two most commonly applied techniques for forward modeling of CSEM data (Li and Key, 2007; Unsworth et al., 1993; Kong et al., 2008; Mitsuhata, 2000; Pridmore et al., 1981; Abubakar et al., 2006; Coggon, 1971; Newman and Alumbaugh, 1995). We used an in-house adaptive finite element 2.5D CSEM forward code called MARE2DCSEM – modeling with adaptively refined elements 2D marine CSEM – by Li and Key (2007) to determine the bathymetric effects on the CSEM data. Inversion of our data was carried out with a 2.5D finite difference forward and inverse code, called 2.5D Pixel Inversion, (Abubakar et al., 2007; Gao, 2007; Abubakar et al., 2008) through the cooperation of an industry partner, David Alumbaugh of EMI Schlumberger. The finite element responses were used as a benchmark to determine the grid size for the finite difference inversion. In Chapter 7 the finite difference inversion and results are discussed.

Forward modeling of geophysical data is an important step to understand the influence of certain physical quantities (resistivity, thickness, geometry, bathymetry) on the data. The profile of CSEM data collected at Hydrate Ridge lends itself easily to 2D modeling because the line was acquired normal to the dominant bathymetry. Information from seismic line 230 (Figure 4.10 in Chapter 4) provides evidence of lateral geologic changes, which also shows that 1D modeling is not adequate and 2D modeling at least is required to gain insight into the geologic properties represented in the Hydrate Ridge CSEM data.

The effect of topography on electromagnetic measurements has been examined in Fox et al. (1980) and Jiracek (1990), with specific attention to the marine CSEM problem by Li and Constable (2007). Bathymetric effects result from the conductivity contrast between seawater and the seafloor, the magnitude of the effect being dependent on transmission frequency, seabed conductivity, seawater depth, transmitter-receiver geometry, and the roughness of seafloor topography (Li and Constable, 2007). Bathymetric effects can have a significant impact on data interpretation when the predicted response from the geologic target is small (as for hydrates) (Li and Constable, 2007). However, finite difference techniques are limited to a stair step representation of bathymetry and accurate results require many small stair steps, which increases the computational time and memory needed to solve these large grids. Unstructured triangular finite element codes are more attractive and flexible for simulating bathymetric effects because the method allows for precise representation of bathymetry using a grid that can conform to any arbitrary surface (Li and Constable, 2007).

## 6.2 FD and FE Numerical Modeling

Numerical methods are necessary when no analytic solution exists or is not practical, which is typically the case for geophysical problems dealing with the

physical propogation of electromagnetic fields in heterogeneous media. The main concern in numerical modeling is casting the governing equations, boundary conditions, and initial conditions into a numerical equivalent or approximate format (Sadiku, 2001). The FD technique is a far more tractable and simpler technique to implement than the FE technique. However, the intricacy in programming the FE technique is compensated by its versatility for handling problems involving complex geometries such as bathymetry and inhomogeneities (Sadiku, 2001) by refining the number of elements around complex features without significantly affecting the entire model space. In the FD method any local refinement propagates throughout the mesh.

The FD and FE methods differ considerably in their mathematical constructs, but the aim is to solve the same physical problem. In general the FD technique requires a three step process as outlined in Sadiku (2001):

**1.** Divide the solution region into a grid of nodes.
**2.** Approximate the differential equations using finite differences by relating the value of a dependent variable at a point in the solution region to values at some neighboring points.
**3.** Solve the difference equations subject to the prescribed boundary conditions and/or initial conditions.

Four basic steps are outlined for the FE technique (Sadiku, 2001):

**1.** Discretize the solution region into a finite number of subregions or elements of the same type.
**2.** Derive governing equations for a typical element.
**3.** Assemble all elements in the solution region.
**4.** Solve the system of equations obtained.

In numerical solutions to physical problems there are three sources of error that are unavoidable: modeling errors, truncation (or discretization) errors, and roundoff errors (Sadiku, 2001). For example, a derivative expressed in terms of a discrete set of points (FD approximation) may be approximated by a Taylor series expansion that is usually truncated, imposing an error present in all FD solutions (Sadiku, 2001).

The SIO-FE and EMI-FD techniques both assume a 2D marine conductivity model that does not vary in the cross-line direction. The governing equations for the electric **E** and magnetic **B** fields are from Chapter 2, Equations 2.12 and 2.13. The 3D electromagnetic fields are Fourier transformed in the invariant resistivity direction in both modeling schemes to reduce the modeling problem to 2D (Hohmann, 1987), putting the governing equations into the wavenumber domain. The source current, $\mathbf{J}_s$, distribution is singular at the location of the source and is consequently difficult to simulate numerically (Nabighian, 1996). The SIO-FE code eliminates the source term from the FE approximation by utilizing the principle of superposition and expressing the electric and magnetic fields as primary and secondary/scattered fields. The EMI-FD code uses the total electric and magnetic fields. From this starting point the next two sections discuss the construction of the SIO-FE and EMI-FD modeling codes.

Figure 6.1A shows the bathymetric profile for CSEM tow 1 with 25 receivers spanning the 16 km line. Note that the EMI-FD code uses electrical conductivity as an input rather than resistivity (used in the SIO-FE code). The FE and FD grids discretize the bathymetric profile differently as shown in Figure 6.1B and C. The finite element mesh is able to provide a more accurate model of the bathymetry.

The FD grid has a discretization of 12.5 m in the vertical by 50 m in

the horizontal direction around the bathymetric features and 25 m to 50 m in the vertical direction by 50 m horizontally outside. There are 331 nodes horizontally and 80 nodes vertically for the entire model space. If the bathymetry cuts across a grid cell the program will automatically average the conductivities. The SIO finite element grid adaptively refines around receivers and transmitters, as is evident in the figure.

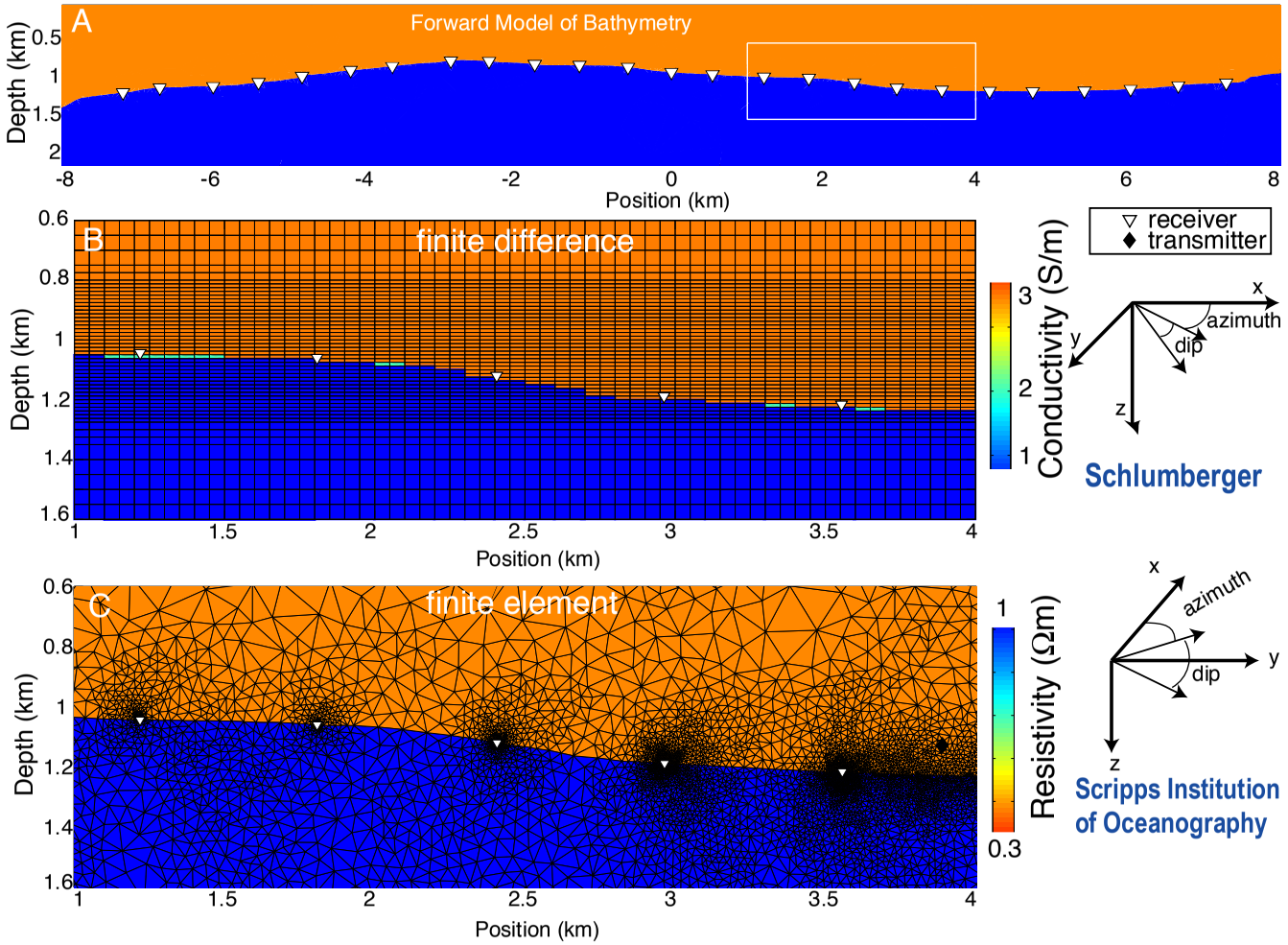


**Figure 6.1**: (A) The bathymetry profile for CSEM tow 1 across Hydrate Ridge can be represented as a FD grid (B) or a FE mesh (C) as shown for the white boxed region in (A). The Schlumberger FD and Scripps Institution of Oceanography FE 2.5D forward modeling codes have different coordinate systems as outlined in (B) and (C).

## 6.3 SIO Finite Element Code

The SIO finite element 2.5D forward modeling code, Modeling with Adaptively Refined Elements (MARE2DCSEM), is written in Fortan90 (Li and Key, 2007). A summary is presented here of the mathematical construction. The code eliminates the singularity of the source term by dealing with primary fields ($\mathbf{E}^p$ and $\mathbf{B}^p$) and secondary fields ($\mathbf{E}^s$ and $\mathbf{B}^s$) separately and using the principle of superposition. The primary fields $\mathbf{E}^p$, $\mathbf{H}^p$ are induced by a horizontal electric dipole in a 1D layered structure with primary conductivity $\sigma_p(z)$, and the secondary fields $\mathbf{E}^s$, $\mathbf{H}^s$ are caused by inhomogeneities with anomalous conductivity $\sigma_s = \sigma - \sigma_p(z)$. Thus, the secondary fields satisfy the following:

$$\nabla \times \mathbf{E}^s = i\omega\mu_o \mathbf{H}^s \tag{6.1}$$

$$\nabla \times \mathbf{H}^s - \sigma \mathbf{E}^s = \sigma_s \mathbf{E}^p. \tag{6.2}$$

The Equations 6.1 and 6.2 are converted from 3D differential equations into 2D equations by Fourier transformation with respect to $x$, the invariant resistivity direction, resulting in six partial differential equations:

$$\frac{\partial \hat{E}_z^s}{\partial y} - \frac{\partial \hat{E}_y^s}{\partial z} = i\omega\mu_o \hat{H}_x^s \tag{6.3}$$

$$\frac{\partial \hat{E}_x^s}{\partial z} - ik_x \hat{E}_z^s = i\omega\mu_o \hat{H}_y^s \tag{6.4}$$

$$ik_x \hat{E}_y^s - \frac{\partial \hat{E}_x^s}{\partial y} = i\omega\mu_o \hat{H}_z^s \tag{6.5}$$

$$\frac{\partial \hat{H}_z^s}{\partial y} - \frac{\partial \hat{H}_y^s}{\partial z} - \sigma \hat{E}_x^s = \sigma_s \hat{E}_x^p \tag{6.6}$$

$$\frac{\partial \hat{H}_x^s}{\partial z} - ik_x \hat{H}_z^s - \sigma \hat{E}_y^s = \sigma_s \hat{E}_y^p \tag{6.7}$$

$$ik_x \hat{H}_y^s - \frac{\partial \hat{H}_x^s}{\partial y} - \sigma \hat{E}_Z^s = \sigma_s \hat{E}_z^p \tag{6.8}$$

where $k_x$ is the wavenumber along the strike direction. The $\hat{}$ denotes the quantity in the wavenumber domain $(k_x, y, z)$. Once the parallel to strike components $\hat{E}_x^s$

and $\hat{H}_x^s$ are found the remaining components $\hat{E}_y^s$, $\hat{E}_z^s$, $\hat{H}_y^s$ and $\hat{H}_z^s$ are derived from the spatial derivatives of $\hat{E}_x^s$ and $\hat{H}_x^s$ and the primary fields. Equations 6.3 to 6.8 can be combined to yield two coupled first order partial differential equations for $\hat{E}_x^s$ and $\hat{H}_x^s$:

$$\nabla \cdot (\frac{\sigma}{\gamma^2} \nabla \hat{E}_x^s) - \sigma \hat{E}_x^s - \frac{\partial}{\partial y}(\frac{ik_x}{\gamma^2}\frac{\partial \hat{H}_x^s}{\partial z}) + \frac{\partial}{\partial z}(\frac{ik_x}{\gamma^2}\frac{\partial \hat{H}_x^s}{\partial y}) = -\frac{\partial}{\partial y}(\frac{ik_x\sigma_s}{\gamma^2}\hat{E}_y^p) - \frac{\partial}{\partial z}(\frac{ik_x\sigma_s}{\gamma^2}\hat{E}_z^p) + \sigma_s \hat{E}_x^p \qquad (6.9)$$

$$\nabla \cdot (\frac{i\omega\mu_0}{\gamma^2} \nabla \hat{H}_x^s) - i\omega\mu_0 \hat{H}_x^s - \frac{\partial}{\partial y}(\frac{ik_x}{\gamma^2}\frac{\partial \hat{E}_x^s}{\partial z}) + \frac{\partial}{\partial z}(\frac{ik_x}{\gamma^2}\frac{\partial \hat{E}_x^s}{\partial y}) = -\frac{\partial}{\partial y}(\frac{i\omega\mu_0\sigma_s}{\gamma^2}\hat{E}_z^p) + \frac{\partial}{\partial z}(\frac{i\omega\mu_0\sigma_s}{\gamma^2}\hat{E}_y^p) \qquad (6.10)$$

where $\gamma^2 = k_x^2 - i\omega\mu_0\sigma$. These equations are solved simultaneously for $\hat{E}_x^s$ and $\hat{H}_x^s$ and are cast into the finite element approximation by the method of weighted residuals (e.g. Zienkiewicz, 1977). A homogeneous Dirichlet boundary condition applies to the outer boundary of the model. The tangental components of the electric and magnetic field are continuous on the inter-element boundaries. A Galerkin variational method is used to select the weighting functions: Equation 6.9 is multiplied by an arbitrary variation of the transformed electric field and Equation 6.10 is multiplied by an arbitrary variation of the transformed magnetic field. The equations are integrated over the model area and modified by the divergence theorem and Greens's theorem. The model area is subdivided into triangular elements with nodal vertices and the homogeneous Dirichlet boundary condition is applied. Within each triangular element the transformed secondary fields are approximated as linear functions of $y$ and $z$ by interpolation of the three nodal values. The area integrals over each element are evaluated analytically, by summing up the integrals over all the elements and assembling the 6 by 6 element matrices (results from two coupled 3 by 3 systems) into a global system matrix to obtain a

linear equation system:

$$\mathbf{Ku} = \mathbf{p} \qquad (6.11)$$

where $\mathbf{u}$ is a column vector of the unknown transformed secondary fields whose size is twice the number of vertices in the model area, and $\mathbf{p}$ is the known vector consisting of the primary fields and arbitrary variation of the transformed fields. When the parallel to strike components of the secondary fields are found in wavenumber domain an inverse Fourier transform gives the fields in the spatial domain, and these are added to primary fields to give the total electromagnetic fields.

A Delaunay refinement algorithm is used for triangular mesh generation (Shewchuk, 2002), and an iterative refinement of the FE grid from a coarse starting grid to progressively more detailed grids is carried out until the desired solution accuracy is obtained (Li and Key, 2007). There is a bias of refinement toward elements that affect the solution at the EM receiver and transmitters locations, and complex geometry, which enables the computation of asymptotically exact solutions to the 2.5D partial differential equations (Li and Key, 2007). The error in the FE solution scales with element size (Li and Key, 2007).

## 6.4 EMI Finite Difference Code

A summary of the EMI finite differences forward modeling code is presented here and is taken from Abubakar et al. (2007) and Gao (2007). The finite difference method solves the total electromagnetic field by substituting $\mathbf{H}$ from Equation 2.12 (Chapter 2) into Equation 2.13 (Chapter 2) to obtain:

$$\nabla \times \nabla \times \mathbf{E} - (i\omega\mu_0\sigma) \cdot \mathbf{E} = i\omega\mu\mathbf{J}_s. \qquad (6.12)$$

The electromagnetic fields vanish at infinity making this an unbounded problem. However, for computational purposes a bounded domain of interest $D = \{(x, y, z) : x_{min} < x < x_{max}, y_{min} < y < y_{max}, z_{min} < z < z_{max}\}$ is assumed. On the outer

bounds the tangential component of the electric field is constrained by:

$$\mathbf{E} \times \mathbf{n} = \mathbf{0} \qquad (6.13)$$

where $\mathbf{n}$ is a unit normal vector. The Equations 6.12 and 6.13 are discretized using the Yee staggered grid formulation (Yee, 1966) with the electric fields located along the edges of discretization cells and the magnetic fields at the center of the discretization cell faces as shown in Figure 6.2. Equation 6.12 is also Fourier transformed in the invarient conductivity (reciprical resisitivity) direction (here it is the $y$ direction). The domain is discretized with a uniform cartesian grid and the boundaries are extended away from the uniform grid in the $x$ and $z$ directions with as few cells as possible using an optimal grid technique. With the Yee discretatization scheme the finite difference approximation to Equation 6.12 is obtained:

$$\hat{\mathbf{F}}(\sigma, \omega) \cdot \hat{\mathbf{E}} = \hat{\mathbf{s}} \qquad (6.14)$$

where $\hat{\mathbf{F}}$ is the stiffness matrix, $\hat{\mathbf{E}}$ is the vector of discretized electric field values, and $\hat{\mathbf{s}}$ is the source vector all in the wavenumber domain (designated by the $\hat{}$ ). Note that:

$$\hat{\mathbf{F}}(\sigma, \omega) \cdot \hat{\mathbf{E}} = \hat{\nabla} \times \hat{\nabla} \times \hat{\mathbf{E}} - (i\omega\mu_0\sigma) \cdot \hat{\mathbf{E}} \qquad (6.15)$$

where $\hat{\nabla} = (\partial_x, k_y, \partial_z)$, and

$$\hat{\mathbf{s}} = i\omega\mu_0\hat{\mathbf{J}}_s. \qquad (6.16)$$

The forward code has an LU decomposition solver that requires only one call to calculate the data misfit and the Jacobian matrix. Forward modeling computes the solution for all source receiver configurations simultaneously by a multi-frontal LU decomposition algorithm (Davis and Duff, 1997), which is a cost equivalent to computing a single source for each frequency. It is a non-iterative solver made possible by employing an optimal grid technique to limit the number of unknowns in the forward problem. This affords accurate solutions as round-off errors and 'spurious modes' associated with the use of iterative matrix inversion

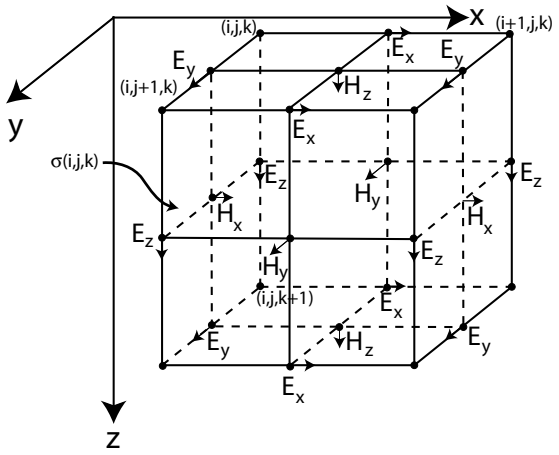


**Figure 6.2**: Positions of the field components in a unit cell of the Yee's lattice applicable to the EMI finite difference forward modeling program. Electric and magnetic fields in a cell (i,j,k) are staggered whereby magnetic fields are calculated on faces of the cell and electric fields are computed on the edges. A cell will have a conductivity $\sigma$(i,j,k) assigned to it (modified from Sadiku (2001)).

techniques are avoided. The total run time is dependent on the number of frequencies to be simulated. After solving the stiffness matrix in Equation 6.14 the electric and magnetic field vectors at the finite difference nodes can be obtained from the inverse Fourier transformation, and **H** is found from Equation 2.12 (Chapter 2).

The use of the Yee staggered grid requires that fields be located at *a priori* defined locations which may not necessarily correspond to the exact source and receiver positions. A simple interpolation is performed from the source point to the staggered grid field locations to provide for the source vector, and a reverse process is used for the receivers. Some components of the electric and magnetic fields are discontinous at the seafloor and so an extrapolation process is used to obtain the fields at receiver positions from nodes above the seafloor.

## 6.5 2.5D Bathymetric Model of Hydrate Ridge

At the time of initial forward modeling the transmitter and receiver positions were still poorly constrained, so a single bathymetric profile was extracted from the bathymetry data collected by Clague et al. (2001) that roughly followed the tow path. The geometry was assumed to be purely in-line (radial) and the transmitter dip was assumed to be zero because the initial version of the SIO-FE code (released 2007) was not capable of modeling an arbitrarily oriented transmitter. A general comparison of the CSEM tow 1 bathymetry profile was made between the SIO-FE and EMI-FD forward modeling codes to examine the relative accuracies. A number of bathymetric half-spaces resistivities (0.5, 1, 2, 3, and 5 $\Omega$m) were used to construct a finite difference grid that will adequately model the bathymetry and be useable for inversion of the Hydrate Ridge data set.

The SIO finite element forward modeling code requires creation of a model domain and boundary condition far away from the bathymetric effects. The bathymetry profile is about 25 km in length, and on either end of the profile an assumed constant depth is extended out to the boundary. The distance to the boundary was $\pm$20 km (about 89 skin depths away at 5 Hz, assuming a 1 $\Omega$m seafloor), making the entire model space 80 km by 80 km ($y \times z$). A total of 282 transmitter positions and 25 receivers were modeled. Forty-three wavenumbers were used, logarithmically spaced from 0.0000001 to 0.9. A single frequency of 5 Hz was used and the primary fields were computed assuming a seawater resistivity of 0.3 $\Omega$m. The air layer is included and assigned an extremely large resistivity of about $10^8$ $\Omega$m. The actual transmitter altitude was used for the height of the transmitter above the bathymetry profile. With the large number of transmitters the problem was split up by sending approximately 40 transmitters to each computer on a 30 node cluster of Power Mac G5 Dual 2.7GHz CPUs, allowing the problem to be solved more quickly. It took approximately 8 hours to solve for the

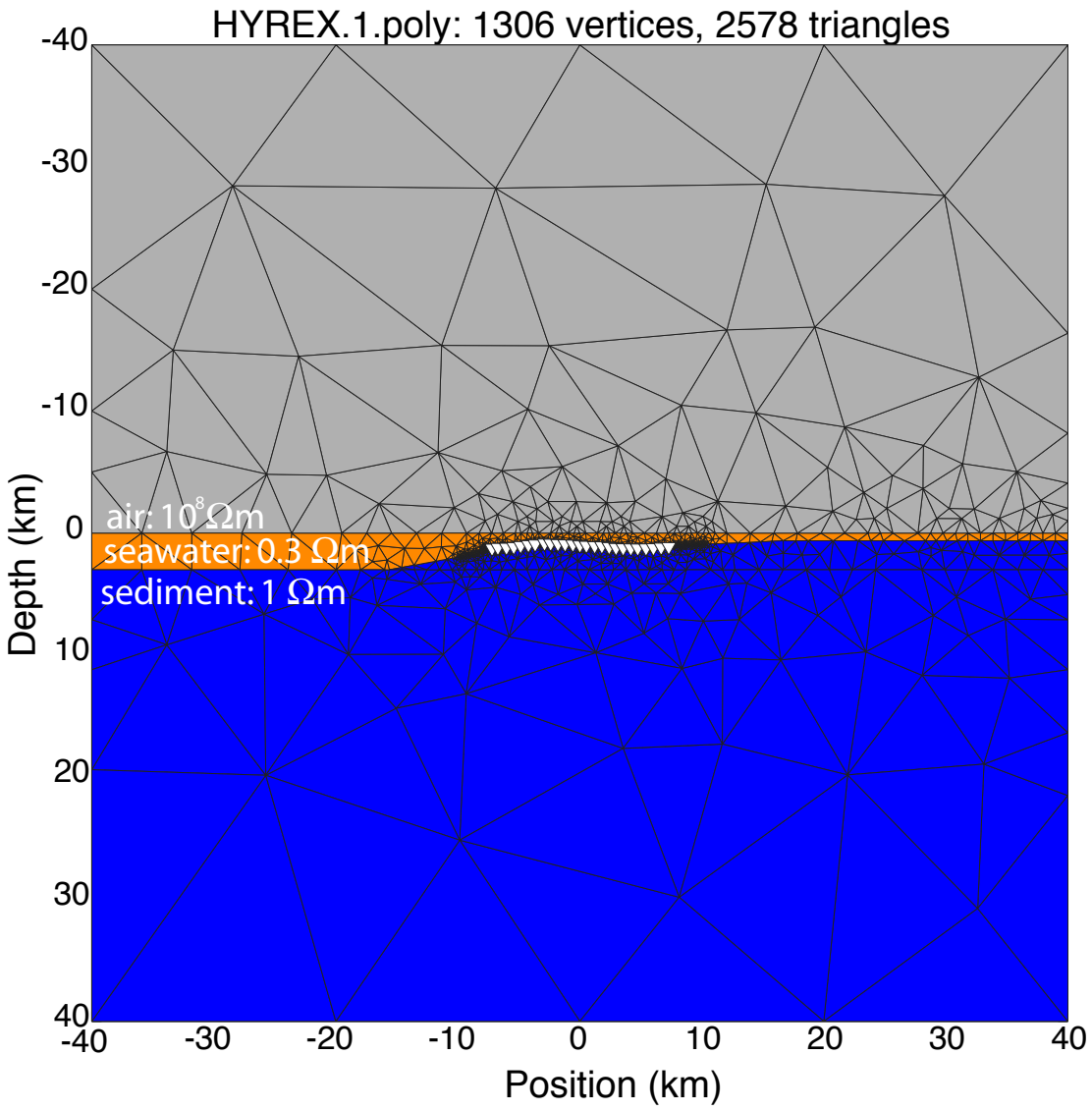


**Figure 6.3**: The entire forward model domain for the SIO-FE code is about 20 km beyond the bathymetric variations. Notice the size of the triangular elements increases away from the bathymetry profile.

forty transmitter positions. For transmitters located near complex bathymetry, grid refinement increases considerably and computation time increases to about 16 hours. The solutions converged in about 16-24 grid refinements per transmitter. In some cases the solutions in some parts of the model appeared to be corrupted with numerical errors. For these places the models were re-run with a forced grid

refinement condition. The number of nodes and elements in total varied, but for one typical case came out to about 11594 nodes and 23154 elements.

Since the EMI code utilizes an optimum grid technique one only needs to consider the single 16 km bathymetry profile; the boundary conditions are automatically taken care of. The Schlumberger Geotool software program was used to generate the mesh and model space. Where the bathymetry crossed a grid cell an average conductivity was assigned to that cell to take into account the seawater and the seafloor conductivity. To increase the speed of computation on a single computer only every second transmitter position was modeled, reducing the problem to about 137 transmitter positions. A result was obtained within a few hours. The selection of a grid was determined by computing the skin depth. For an accurate solution the spatial increment $\delta x$ and $\delta z$ must be small compared to the wavelength. In places where a poor comparison with the SIO-FE grid was obtained, a modification of the grid, by increasing the grid size or modifying the conductivities, improved the solutions, especially where the bathymetry changed more severly.

### 6.5.1 Comparison of FE and FD Models

A comparison of the FE and FD forward modeling is shown in Figures 6.4 and 6.5 at two different sites (site 4 and site 17) showing agreement (Figure 6.4) and disagreement (Figure 6.5) between the results. Site 4 is on relatively flat bathymetry whereas site 17 is on a steeper slope, where we observe the limitations of the finite difference grid compared to the finite element grid. All components of the in-line (radial) electromagnetic field are plotted as amplitude, phase, and an amplitude ratio of the EMI-FD to SIO-FE versus distance along profile. At the bottom of Figures 6.4 and Figures 6.5 is the bathymetric profile, with the transmitter tow and receiver positions in the region surrounding the respective sites ($\pm$3000 m). The first example (Figure 6.4) has very similar model results for the

two approaches with the largest difference occuring at the closest approach of the the transmitter to the receiver site 4. This is expected because the finite difference grid is limited to interpolation of the electromagnetic fields across a grid size of 12.5 m by 50 m, whereas the finite element code will refine the grid to get as accurate a solution as possible. Furthermore, the finite element code has computed the scattered field rather then the total field and so there are no inaccuracies in the representation of the transmitter. The finite difference code cannot properly model the rapid changes near the source without using a much finer grid, whereas the scattered field solution can model these changes as long as there are not any scatterers immediately adjacent to the source.

There are also bathymetric effects in the responses captured by both the finite element and finite difference codes at 7800 m, where the transmitter first attains the target height of 100 m. Notice the magnetic field has the smallest difference compared to the in-line electric field, and vertical electric field has the largest difference compared to the in-line electric and magnetic fields. In the finite difference modeling three different types of grids where used: (a) 100 m in the horizontal by 12.5 m in the vertical, (b) 50 m horizontal by 12.5 m vertical and (c) 50 m horizontal by 25 m vertical. It was quickly determined that the 50 m by 12.5 m gave the better solution with most improvement in the vertical electric field computation. The 50 m by 25 m grid tended to underestimate the fields. Any differences that do occur between the FD and FE codes are amplified by a higher seafloor resistivity; observe the 5 $\Omega$m and 1 $\Omega$m differences.

The improvements with mesh refinement are most noticeable for site 17 (Figure 6.5) (distance $\approx$2500 m), located on a slope deepening to the east. The horizontal electric fields are underestimated on the upward side ($\leq$2500 m) and are overestimated on the downslope side ($\geq$2500 m) in the 100 m by 12.5 m grids, but for both the 50 m by 12.5 m and 50 m by 25 m grids the ratio of EMI:SIO

is ≈1. The vertical electric field component has the largest errors from a poor representation of bathymetry, and is vastly improved by making the grid finer. The small effect in the magnetic field is probably due to the fact that the magnetic field is perpendicular to the bathymetric profile and less susceptible to galvanic effects associated with conductivity contrasts along the profile.

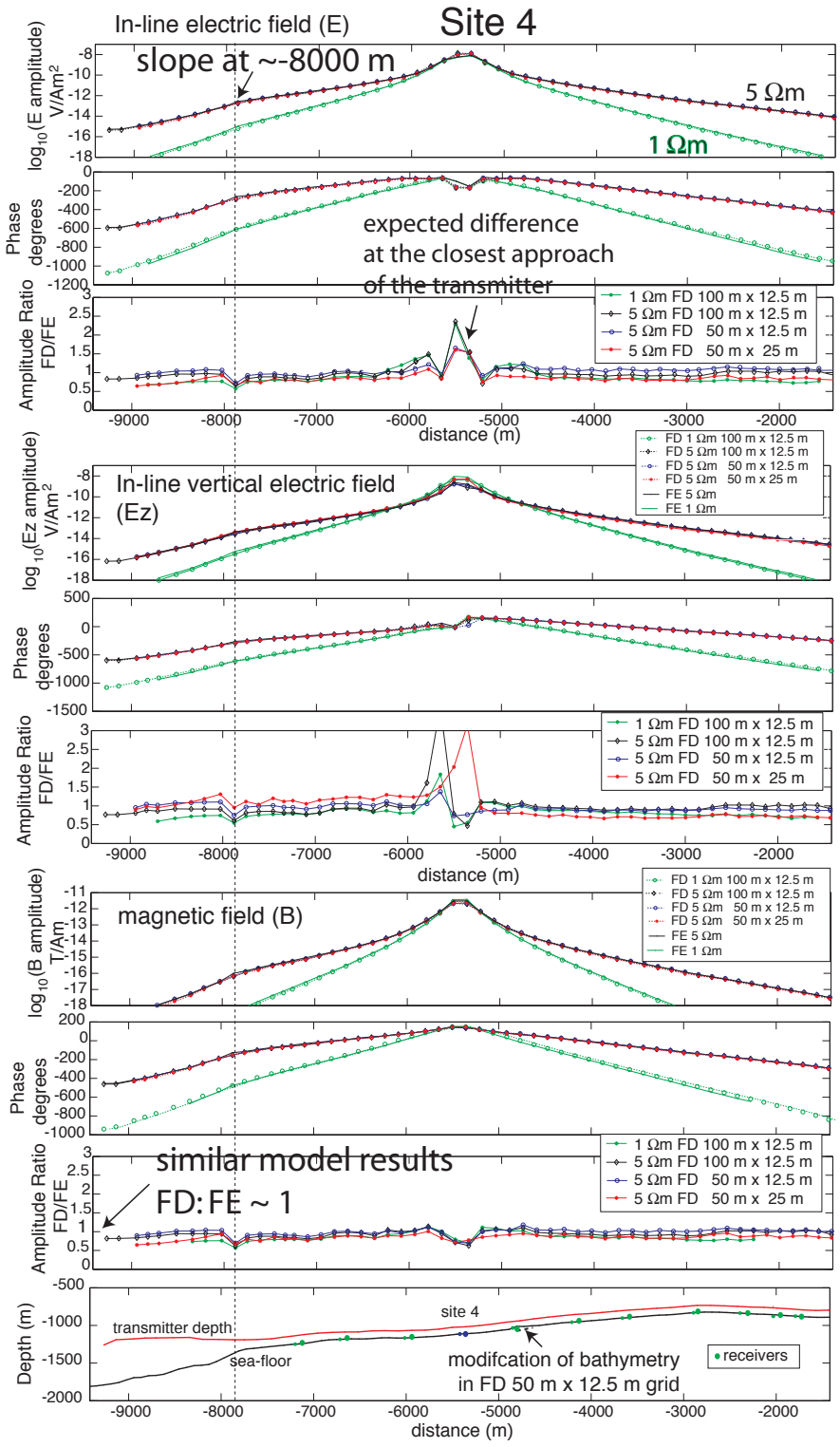


**Figure 6.4**: FE and FD bathymetric forward models shows good agreement for a 1 Ωm and 5 Ωm half-space at site 4 – on relatively flat seafloor. All components of the in-line electric and magnetic fields are plotted.

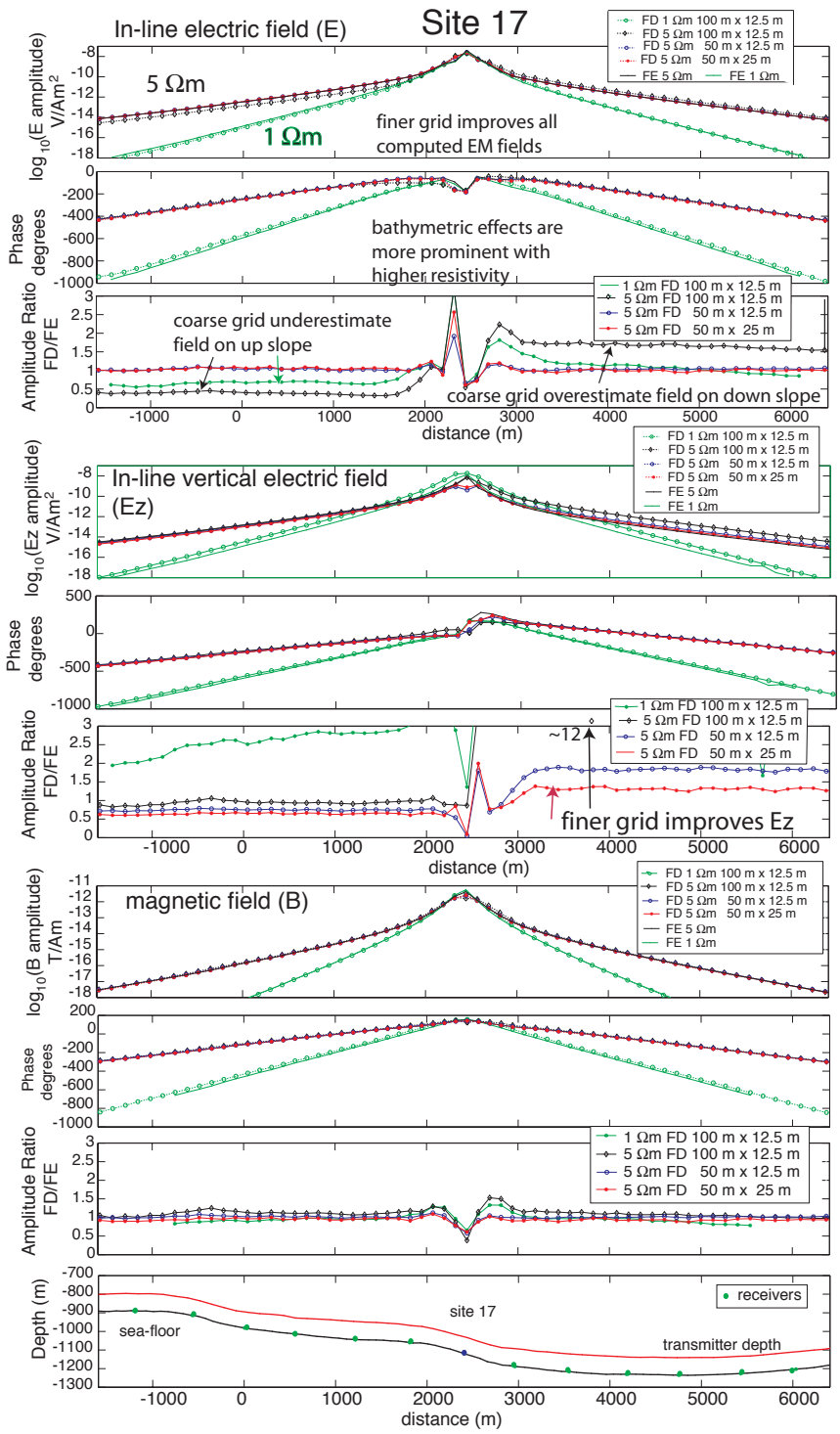


**Figure 6.5**: FE and FD bathymetric forward models shows vast differences for a 1 Ωm and 5 Ωm half-space at site 17. All components of the in line electric and magnetic fields are plotted. Site 17 is on relatively steep seafloor and has improved results for the FE and FD when the grid is refined.

## 6.6 Conclusion

A comparison of a finite element and finite difference code allowed the construction of an accurate finite difference grid for use in a 2D inversion of the data set (next chapter). The finite element code was used as a benchmark for the finite difference grid, since the finite element code is more accurate in modeling bathymetry, compared to the limitation of stair-step representation of bathymetry offered by the finite difference grid. The comparison shows that in-line magnetic fields are less affected by choosing either a finite element or finite difference grid. However the in-line horizontal electric fields are dependent on an adequate representation of bathymetry. The grid which gave a reasonable comparison between the finite element and finite difference was the 50 m by 12.5 m discretization for the seafloor bathymetry. The vertical electric fields were affected the most by a poor representation of sloping bathymetry, and while improvements were made by using the 50 m by 12.5 m grid, there are still large differences $\approx$2 (which is approximately the order of signal expected from hydrate). To keep the problem smaller the vertical electric and magnetic fields were left out of any inversions discussed in the following chapter because further FD grid refinement would be needed to include the vertical electric fields and more computation time would be required for the magnetic fields, which are also unlikely to have a significant hydrate signal.

# 7

# Inversion of Hydrate Ridge Data

A proprietary, 2.5D controlled source electromagnetic inversion program was made available to us by EMI Schlumberger and applied to the fundamental frequency (5 Hz) for tow 1 of the CSEM data collected at Hydrate Ridge. The results are compared to the initial pseudosection and MT results, Ocean Drilling Program Leg 204 well logs, and seismic line 230 to gain a more complete understanding both of CSEM technology and the Hydrate Ridge geology.

## 7.1 General Theory

A brief introduction to the proprietary 2.5D "DeepEM" inversion code is presented based on information provided from Abubakar et al. (2007, 2006, 2008). The code uses an iterative linearized approach to solve the non-linear inverse problem (Farquharson and Oldenburg, 1998). The 2.5D DeepEM inversion seeks to minimize the difference between the measured field data and the predicted response generated by the forward simulator, subject to constraints that stabilize the inversion (Abubakar et al., 2006). The multiplicative cost function, $\Phi_n$, is minimized by the inversion at the $n^{th}$ iteration:

$$\Phi_n(\mathbf{m}) = \phi^d(\mathbf{m}) \times \phi_n^m(\mathbf{m}), \qquad (7.1)$$

where the first term is the data misfit $\phi^d$ and the second term $\phi_n^m$ is a measure of the variation of the model parameters and serves to regularize (or stabilize)

the inversion (Abubakar et al., 2007). The $\mathbf{m}$ is the vector of model parameters to be solved, in this case electrical conductivity, $\sigma$, at each node. Specifically, $\mathbf{m}$=$m(x_p, z_p) = \sigma(x_p, z_p)/\sigma_o$, where $(x_p, z_p)$ denotes the center of the 2D discretization cell and $\sigma_o$ is the spatial average of the initial model conductivity (Abubakar et al., 2007).

The data misfit, $\phi^d$ is the weighted difference between the measured data, $d_{i,j}^{obs}$, and predicted forward model response, $S_{i,j}(\mathbf{m})$ ($i$ indexes source position, $j$ indexes receiver position):

$$\phi^d(\mathbf{m}) = \frac{\Sigma_{i=1}^{I}\Sigma_{j=1}^{J}|W_{d;i,j}[d_{i,j}^{obs} - S_{i,j}(\mathbf{m})]|^2}{\Sigma_{i=1}^{I}\Sigma_{j=1}^{J}|W_{d;i,j}d_{i,j}^{obs}|^2}. \qquad (7.2)$$

Here $W_{d;i,j}$ is the data weighting made up of the estimates of the standard deviations of the noise (Abubakar et al., 2007).

The regularization function $\phi_n^m$ is a measure of the variation of the model from a known reference model, $\mathbf{m^{ref}}$:

$$\phi_n^m(\mathbf{m}) = \int_D b_n^2(x,z)\{|\nabla_t[m(x,z) - m^{ref}(x,z)]|^2 + \delta_n^2\} \qquad (7.3)$$

where $\nabla_t$ is the spatial differentiation in $x$ and $z$, the weight $b_n(x,z)$ is the $L_2$ norm regularizer, and the $\delta_n^2$ is a constant that ensures a non-zero condition for the regularization function. The weight $b_n(x,z)$ may be given as a $L_2$ norm regularizer or as a weighted $L_2$ norm regularizer, which are quadratic functions with a well-defined gradient solved with a Gauss-Newton minimization approach (Abubakar et al., 2007). Equation 7.1 may be approximated as:

$$\mathbf{H}_n \cdot \mathbf{p}_n = -\mathbf{g}_n \qquad (7.4)$$

where $\mathbf{H}$ is the Hessian matrix (a square matrix of second order partial derivatives of a function), $\mathbf{p}_n$ is the search vector along which the quadratic cost function is minimized, and $\mathbf{g}_n$ is the gradient of the cost function. The Hessian matrix is

approximated by neglecting the second order derivative of the cost function and the non-symmetric terms (Abubakar et al., 2006);

$$\mathbf{H}_n \approx \mathbf{J}_n^T \cdot \mathbf{W}_d^T \mathbf{W}_d \cdot \mathbf{J}_n^T + \phi^d(\mathbf{m}_n) L(\mathbf{m}_n) \qquad (7.5)$$

and the gradient;

$$\mathbf{g}_m = \mathbf{J}_n^T \cdot \mathbf{W}_d^T \cdot [\mathbf{d}^{obs} - \mathbf{S}(\mathbf{m}_n)] + \phi^d(\mathbf{m}_n) L(\mathbf{m}_n) \cdot \mathbf{m}_n \qquad (7.6)$$

where $L(\mathbf{m}_n) \cdot \mathbf{m}_n = \nabla_t \left[ b_n^2(x,z) \nabla_t m_n(x,z) \right]$ and $\mathbf{J}_n$ is the Jacobian matrix. The Jacobian matrix is calculated using an adjoint method with a set of forward computations in which the roles of the receiver and transmitter are interchanged. All source excitations are solved simultaneously, providing a fast solution for the inverse problem where the solution for many source locations and orientations can be achieved by inverting the stiffness matrix $\mathbf{H_n}$ only once. To improve conditioning of the inversion two different regularizations are employed: a $L_2$ norm regularization which provides a smooth solution, and a weighted $L_2$ norm constraint which provides a sharp reconstructed image (Habashy and Abubakar, 2004; Abubakar et al., 2007, 2006).

The Hessian matrix is large and Equation 7.4 is solved with an iterative technique utilizing a conjugate gradient least squares scheme to solve for $\mathbf{p}_n$. The model parameters are updated via a line search algorithm to check that the cost function is reduced at each iteration (Habashy and Abubakar, 2004; Abubakar et al., 2007). A nonlinear transformation procedure may force the model parameters to lie within upper and lower bounds if *a priori* information is added to the inversion (Habashy and Abubakar, 2004; Abubakar et al., 2007).

The iterative scheme of calculating the forward solutions and minimizing the cost function proceeds until one of four conditions are met (Habashy and Abubakar, 2004; Abubakar et al., 2007):

1. The data misfit reaches a predetermined tolerance.
2. The differences between the data misfit at two successive iterates are within a predetermined small number.
3. The difference between the model parameters at two successive iteration is within a predetermined small number.
4. The total number of iterations exceeds a prescribed maximum.

## 7.2 Application to Hydrate Ridge Data

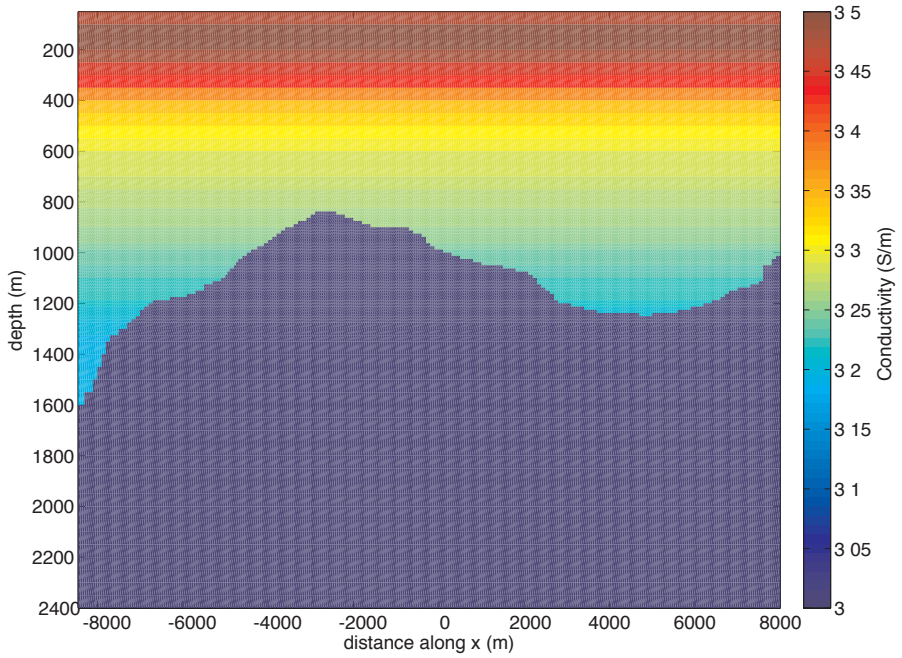


**Figure 7.1**: Seawater and sediment conductivity model used for the inversion. The color scale has been saturated to allow the seawater conductivity values of 3 S/m to 3.5 S/m to be seen clearly. The darkest blue colors are representative of the 1 S/m bathymetric half-space conductivity for the sediments. The axes are not equal.

The forward modeling presented in Chapter 6 allowed us to construct an appropriate grid to maintain model accuracy during the inversion of the data. A vertical profile of seawater conductivity based on the transmitter's conductivity

profiler (Figure 7.1) was used for the inversion because seawater resistivity and seafloor resistivity are coupled (Constable, pers comm; Key, pers comm; Alumbaugh, pers. comm).

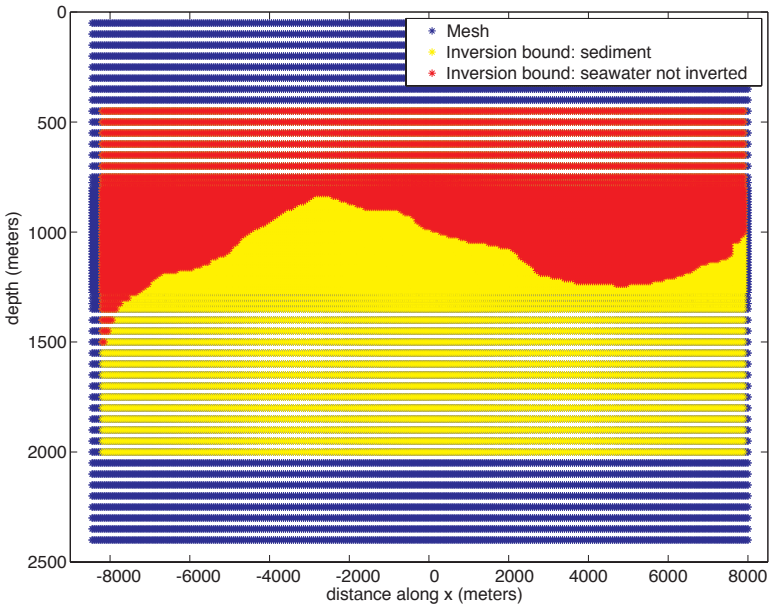


**Figure 7.2**: The mask and inversion domain used for the 2.5D inversion. The red and yellow regions mark the inversion domain used from the entire mesh (blue) where red represents seawater conductivity and yellow represents the seafloor conductivity. The seawater conductivity is not solved for in the inversion because it is known from direct measurements and will be "masked" from the inversion domain. The axes are not equal and the horizontal lines are a change in the vertical grid size to 50 m.

The inversion domain was initialized with a single seafloor resistivity of 1 Ωm and the seawater conductivity profile. The entire model mesh extends from 0 to 2400 m depth and from -8500 m to 8000 m in $x$. The inversion domain is ideally specified to be only where the transmitters and receivers are located. In this case the inversion domain is from -8250 to 7850 m in $y$ and from 812.5 m to 1950 m in $z$. This region contains both seawater and sediment (marked red and yellow in Figure 7.2). A mask was used to remove seawater from the inversion region so we only invert for sediment conductivity (Figure 7.2).

## 7.3 2D Inversion Results

The inversion program was given 59 transmitter positions spaced ≈240 m apart and 25 seafloor receivers spaced ≈ 700 m apart. The observed in-line imaginary and real electric field data were assigned a noise estimate of 5% of the maximum datum amplitude. The 2.5D inversion, Figure 7.3, achieved an RMS misfit of 4.73 in 22 iterations from a starting RMS of 12.03.

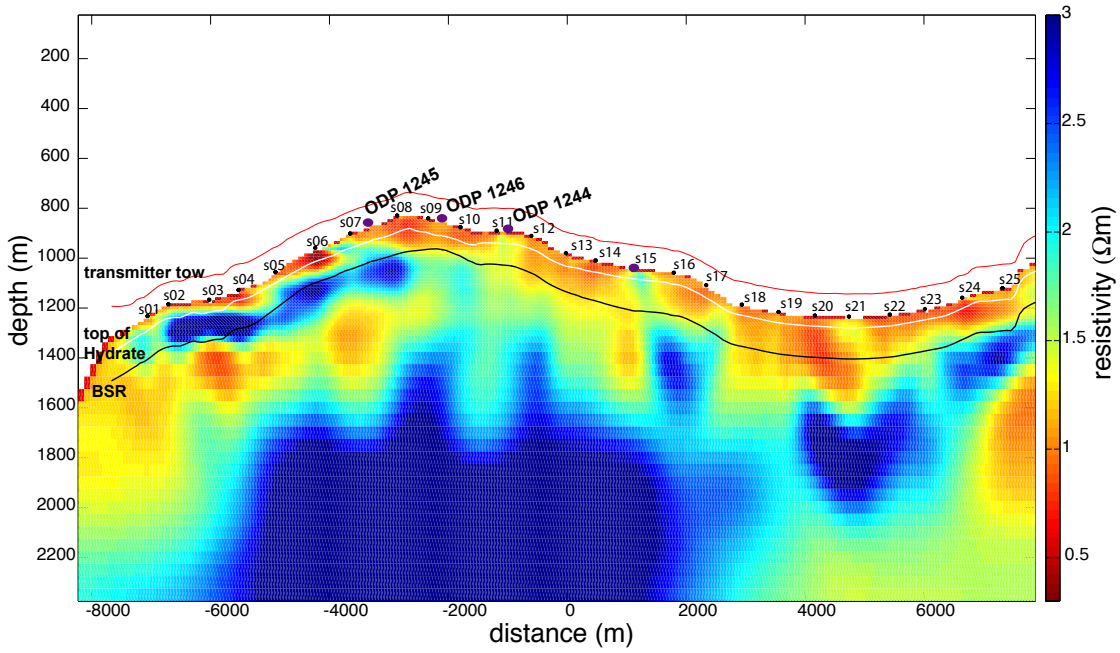


**Figure 7.3**: A 2.5D DeepEM inversion plotted with a resistivity scale from 0.5 to 3 Ωm (2 to 0.3 S/m). The transmitter positions are marked by the red line above the seafloor; receivers are marked and labeled. The estimated top of hydrate is marked by the white line and the seismic bottom simulating reflector is marked by a black line. The four ocean drilling program leg 204 well logs – 1245, 1244, 1246, 1252 – are marked with purple circles.

The inversions were run by EMI Schlumberger because of restrictions on proprietary access to the code, and a couple of mistakes were made that we had no opportunity to correct. First, the transmitter altitude was set too shallow by about 10 m because we used data from the pressure depth gauge rather then the al-

timeter height. The forward modeled bathymetry profile used in the original mesh setup differs from the sum of the depth and altitude by about 10 m. This caused shallow conductors to appear in some places because the transmitter is modeled a little closer than it should be to the seafloor. In retrospect the mesh should have been made using the transmitter's depth profile, but during the comparison with the 2.5D finite element models the same bathymetry profile had to be used. The second mistake is that the inversion domain is a little too big. The transmitter profile starts at about -7667 m, but the inversion bound extends to -8225 m, and edge effects appear to be present. Another minor mistake is that the grid spacing is too large at the western side of the profile, resulting in a lack of accuracy there.

The inversion result in Figure 7.3 includes a shallow conductive basin below sites 18-25, and a shallow resistor at about the depth of the BSR to the west below sites 1 to 7. Deeper in the inversion at about 1600 m there is evidence of folding in the accretionary prism.

### 7.3.1 Comparison with Pseudosections

The first CSEM pseudosections results (Weitemeyer et al., 2006c) are plotted along with the new 2.5 DeepEM inversion results in Figure 7.4. The inversion provides a depth scale unattainable from the pseudosections, giving both lateral and vertical resistivity distributions. There are many similarities in spite of the fact that the pseudosections lack the navigational rigor applied to the inversion and do not include bathymetry. First, the conductive pant leg feature observed in the pseudosections still appears but has been collapsed to a surface conductor in the inversion, confirming that it was an artifact of the pseudosection projection technique. Deeper, the inversion provides an image of the folding associated with the accretionary complex sediments. The resistive feature associated with the seismic anticline under site 16 is still present, and the conductive basin to the east also remains. Under sites 1 to 4 a resistor is clearly present in all images.

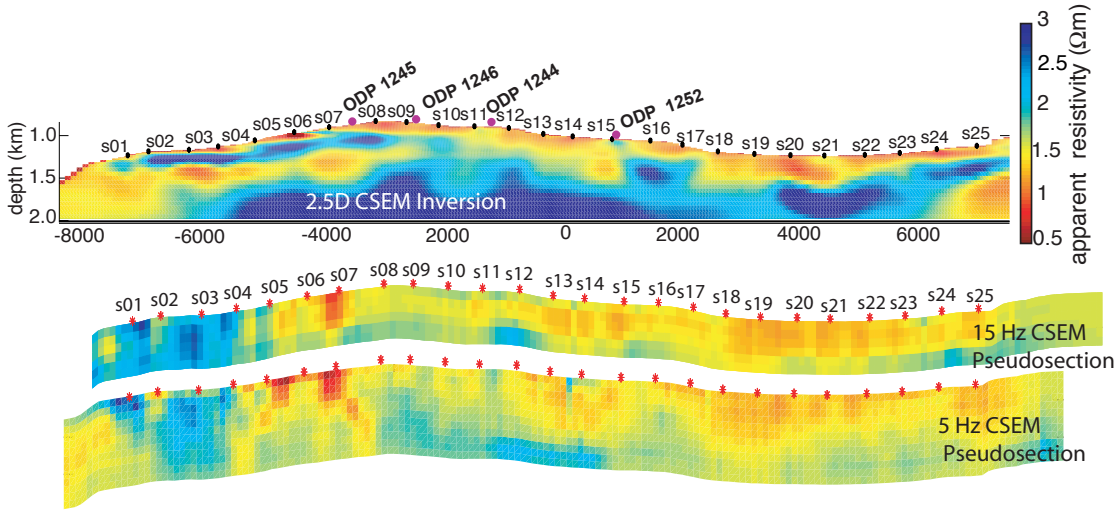


**Figure 7.4**: The 5 and 15 Hz pseudosections are plotted with the new CSEM inversion result. The lateral heterogeneity across the pseudosections is remarkably similar the the CSEM inversion. However, the depth and resolution the inversion provide us with differences as well between the two models.

The differences between the CSEM inversion and the pseudosections are obvious by the layering pattern observed in the inversion. The resistive layer near the seismic BSR was not obvious at all in the pseudosections. The extent of the resistor to the east of site 4 was not obvious because a conductive pant leg artifact dominated the pseudosection image.

### 7.3.2 Comparison with Logging While Drilling (LWD)

There are three Ocean Drilling Program Leg 204 LWD boreholes along the CSEM profile with well logs that we can compare with the CSEM inversion. CSEM soundings provide a bulk resistivity measurement in the meter to kilometer scale, compared with the detailed centimeter scale resolution of the well log and so we expect some differences between the two very different samplings of the seafloor resistivity. For example the logging while drilling (LWD) deep focussed resistivity measurement has penetration depths of 12.7 cm and vertical resolution of 5-8 cm

(Shipboad Scientific Party, 2003a). The resistivity at the bit (RAB) has a lateral depth of investigation of 30.48 cm (Shipboad Scientific Party, 2003a). The logging while drilling (LWD) resistivity data is used rather than wireline logging because LWD takes place during excavation of the hole (or shortly after), ensuring a measurement of resistivity before conductive drilling fluids invade deeply into the formation (Schlumberger, 2008) or hydrates destabilize. The deep resistivity log provides the most useful data for comparison with the CSEM inversion because it samples the greatest volume. The CSEM resistivity values in the inverted model closest to each of the ODP Leg 204 well logs (1245, 1244, 1246) are used to make a comparison between the two data sets, LWD and RAB, in Figure 7.5.

The RAB image maps the electrical resistivity around the borehole wall and is shown here as unwrapped borehole images with a color scale provided by ODP Leg 204 Scientific Party. A differential caliper log provides a measure of the quality of the borehole conditions and it indicates regions that have "washout" areas, which typically occur in the top 50 m of the well log (Shipboad Scientific Party, 2003c). For these reasons the shallowest resistivity measurements are not that reliable: the top 38 m for 1244D, the top 24 m for 1245A and top 50 m for 1246A (Shipboad Scientific Party, 2003c,d,e).

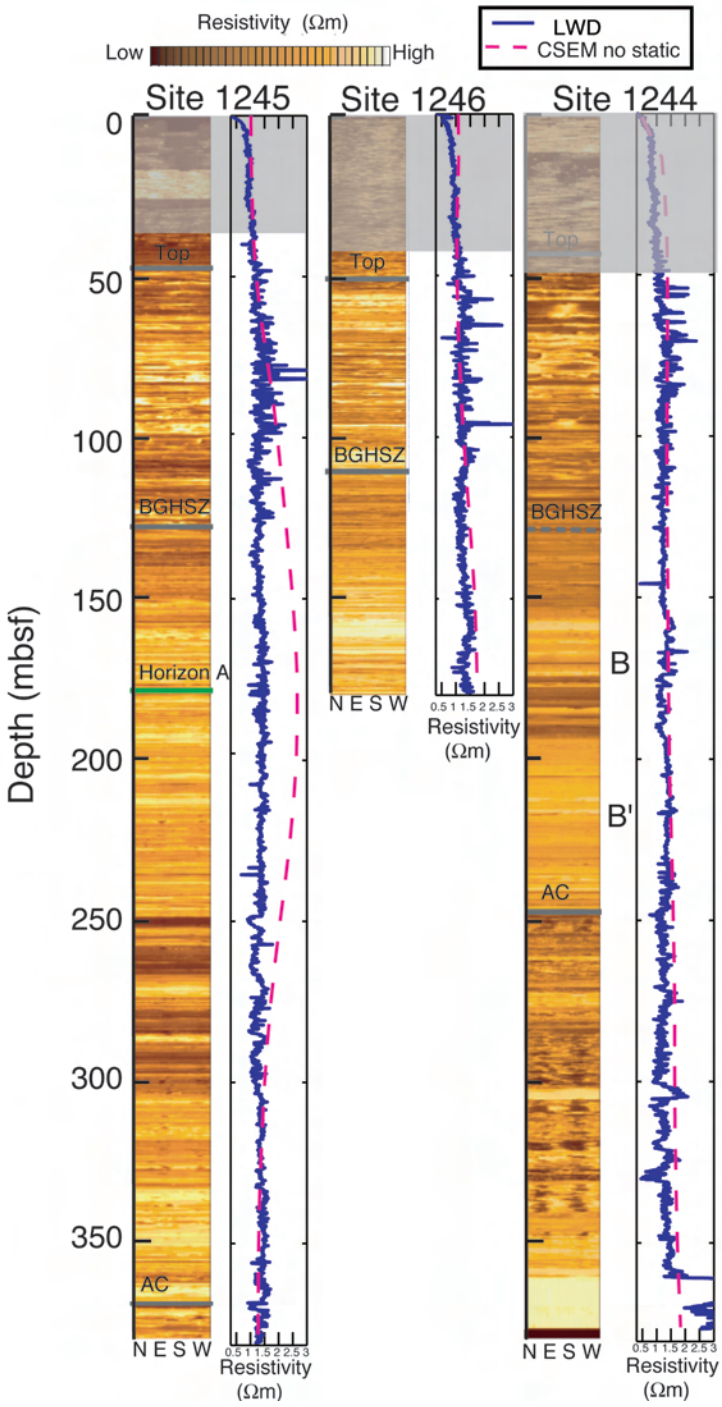


**Figure 7.5**: RAB and deep LWD resistivity measurements from Shipboard Scientific Party (2003) are compared with the CSEM inversion result. Sites 1246 and 1244 compare well to the CSEM inversion. Site 1245 compares well at the top and bottom of the log, but differs significantly in the middle (see text for more detail). The grayed out region is where RAB and LWD measurements are unreliable (ODP Leg 204 data from http://brg.ldeo.columbia.edu/logdb/).

There is broad general agreement between the CSEM and the LWD resistivities at sites 1246 and 1244. The CSEM provides an average resistivity value compared to the many small changes in resistivity observed in LWD and will never be able to provide the centimeter detail offered by LWD. Site 1245 has a very obvious difference between the LWD and CSEM at the central portion of the log. The upper 100 m and last 75 m in depth appear to agree well with the logged resistivities, however in the region between 100 m and about 300 m depth there are differences of nearly a factor of 2. The CSEM inversions give a relatively large resistivity value, about 2.75 Ωm at the location of seismic horizon A, whereas the well logged resistivities show an average resistivity of about 1.5 Ωm and the RAB shows a high electrical resistivity in this region. The differences between the CSEM and LWD could be that CSEM is observing the cummulative effect of all the thin resistive layers observed in the RAB, and is thus seeing the bulk effect of all these thin resistors, or that the CSEM inversion has over-smoothed the resistive layers at 75 m (CSEM methods measure mostly vertical resistivity but the thin layers will result in anistropy). However, considering that horizon A is known to be a fluid conduit carrying quantities of free gas to the summit it is possible that it is being seen as a resistor by the CSEM data but not by the well logs.

Site 1252 has no logging while drilling measurements due to drilling safety concerns associated with its location on an anticline with a significant BSR. There are, however, wireline logging induction measurements and any hydrate that was present would have largely been disturbed or dissociated. The well log resistivity measurements are in general agreement with the CSEM inversion results but slightly more resistive throughout the sequence.

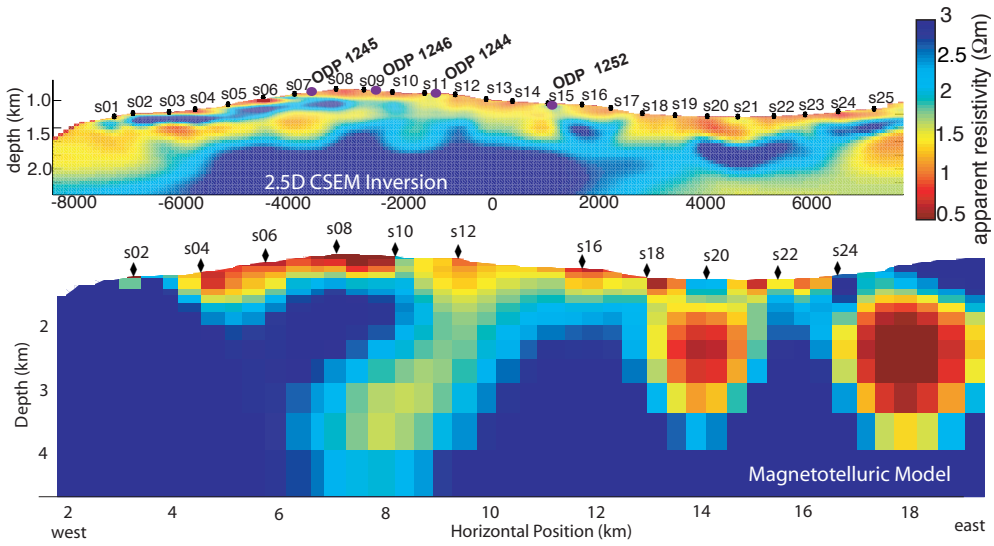


**Figure 7.6**: Magnetotelluric inversion model has a lower resolution than the CSEM inversion. The folding associated with the accretionary complex becomes more obvious in the CSEM inversion.

### 7.3.3 Comparison with MT Results

The instruments with magnetic sensors collected MT data for the entire duration of the experiment (about 46 hours) and periods from 10-1000 s were measured. The data were processed using Egbert (1997) multi-station MT processing code and were inverted using a 2D MT OCCAM inversion program (deGroot Hedlin and Constable, 1990). The results were briefly presented in Weitemeyer et al. (2006a). Figure 7.6 shows a close-up of the MT model with a color scale saturated to match the CSEM model's resistivity scale. The conductive basin from sites 17 to 25 is present in all data sets. There is an increase in resistivity with depth as a result of compaction and lithologic changes. The MT model highlights the conductors more than the resistors, but both models show the presence of folding associated with the accretionary complex which was less apparent in the pseudosection projection technique. Under site 16 is the anticline obvious in all images. The MT model includes a dipping conductor at around 8 km that is less pronounced in the CSEM inversion, possibly because of a lack of depth penetra-

tion. The MT model also has a deep resistor to the west, whereas the CSEM model has a shallow resistor around the BSR in this region. Both the MT model and CSEM model place a surface conductor just below site 6.

### 7.3.4 Comparison with Seismic Line 230

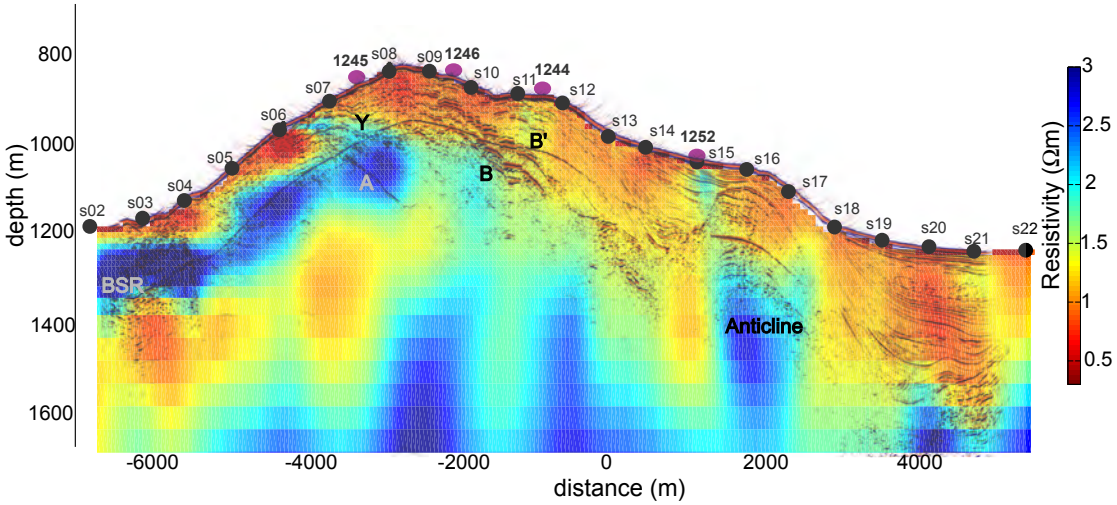


**Figure 7.7**: The CSEM inversion is overlain by seismic line 230. A number of seismic features are labeled: BSR – bottom simulating reflector; A – seismic horizon that carries free gas to the summit (out of the page); B and B' – highly faulted conduits; Y and Y' a regional unconformity.

The co-location of the CSEM tow 1 with seismic line 230 allows us to make a comparison between the CSEM inversions and the seismic data (Figure 7.7). To the west is a resistor at about the depth of the seismic bottom simulating reflector (BSR), which typically marks the phase change from solid hydrate above and free gas below. In this region of Hydrate Ridge the hydrates are biogenic and hence a concentration of gas at the BSR is expected (Shipboad Scientific Party, 2003b). The chaotic seismic region between sites 2 to 4 was interpreted as having high free gas or gas hydrate saturations in inversion by Zhang and McMechan (2003). The CSEM inversion has a large resistor in the same region, also suggesting high hydrate concentrations. The shallow resistor between sites 6 and 7

may correspond to seismic horizons Y and Y', a regional geologic unconformity (Chevallier et al., 2006). Seismic horizon A is a gas-charged fluid conduit taking methane gas to the southern summit (out of the page), which also shows up as a resistor in the CSEM inversion. Seismic horizons B and B' are largely faulted volcanic ash-lined conduits carrying free gas into the gas hydrate stability zone, which then freezes into hydrate (Tréhu et al., 2003). A conductive region exists within the hydrate stability zone at the summit of this profile suggesting lower hydrate concentrations and/or the presence of brines. The anticline under site 16 is present as a resistor and may be a result of a change in lithology.

## 7.4 Conclusions

The inversion results so far are only for the fundamental frequency of 5 Hz. Including the higher frequency harmonics, such as the 15 Hz data, may constrain the depth of the layered resistor that is around the seismic BSR. There is also azimuthal tow data, vertical electric field data, and magnetic field data available. However, the forward modeling showed that the EMI finite difference code would need a much finer mesh to invert $E_z$ data. We would also need to account for tilt of the receivers, in addition to that of the transmitter. The magnetic field data could also be inverted but modeling shows that it is no more sensitive to hydrate than the horizontal electric fields.

# 8

# Discussion and Conclusions

Marine electromagnetic methods to detect gas hydrates have long been discussed but few field trials have been carried out. Our study at Hydrate Ridge represented an opportunistic use of ship time with very limited funding from Exxon Mobil and from GERD, Japan to study gas hydrates. We only had 3 days of data collection on station. For these reasons it is merely a pilot study, which aimed to demonstrate that CSEM may provide a valuable tool in discriminating hydrate. Although this study provides no conclusive evidence, there are strong indications that it is sensitive to hydrate distribution, and it acts as a starting point from which new development and improvements to the technology can be made.

Many technical improvements have already been implemented since the Hydrate Ridge experiment. To avoid saturation of amplifiers all of the gains have been reduced. The orientation of the instruments is determined with an external compass located on the top of the instrument frame away from the distortions of the magnetometers and batteries. The transmitter has a tail end depth gauge and an acoustic transponder to determine the transmitter dip. A new navigation system has been developed in which two paravanes with GPS receivers and acoustic LBL transponders are towed behind the vessel on the sea surface a few hundred meters from the ship. Ranging from the transmitter to these transponders allows a triangulation of the transmitter position.

Problems with navigation of the transmitter for the Hydrate Ridge experiment led to the development of an innovative way to use the near-field electromagnetic data to constrain the position of the transmitter and receivers. The improvement in navigation was required for a finite difference 2D inversion of the data set. The Scripps Institution of Oceanography finite element 2.5D forward modeling code was used as a benchmark for the Schlumberger finite difference code and to choose an appropriate grid for inversion of the horizontal electric fields. Without the use of the SIO FE code, it is likely that the FD code would have been inadequately meshed and subject to errors.

Our forward model studies demonstrated the advantage of collecting high frequency data to detect the more sensitive part of the the hydrate anomaly. However, with higher frequencies comes the requirement of meter scale resolution for the source-receiver range. This led to the development of a towed receiver which contains three orthogonal electric field dipoles. The fixed length of line used to attach the towed receiver to the transmitter antenna means there is very little navigational error. The three component receiver allows for both in-line and vertical electric fields to be recorded, which is important when looking for other hydrate geometries such as dipping hydrate dikes.

Shortly after the collection of the Hydrate Ridge data a proposal was circulated to extend our studies to the Gulf of Mexico. In October 2008 three sites are to be surveyed in the Gulf of Mexico. One site is currently a designated hydrate observatory (MC 118) and two other sides are hydrate targeted Joint Industry Program drill sites (GC 955 and AC 818).

One major problem for using electromagnetic techniques to map hydrate is that there have been few electrical conductivity laboratory measurements made

on hydrate. We thus lack a mechanism for determining the quantity or concentration of hydrate expected from an electrical resistivity measurement. Relationships like Archie's Law are perhaps valid for a disseminated distribution of hydrate, but if hydrate forms in veins and fractures other relationships, such as the Hashin-Strikmen bounds, might be more valid. Unlike Archie's Law, these relationships depend on a quantitative estimate of hydrate conductivity. Recent funding will allow this work to take place.

While the Hydrate Ridge data was meant to target hydrate, the simultaneous collection of magnetotelluric data allowed us to obtain a glance at the electrical conductivity image of the oceanic crust and mantle and an image of the folding of the accretionary complex associated with the subduction zone. While the footprint is too small to image the subducting plate, these data present the potential for a much larger scale survey to successfully image the subducting slab.

Future work on the Hydrate Ridge data will involve an inversion of the vertical electric field data, but this will require the development of a 2.5D finite element inversion scheme. So far only the 5 Hz in-line data have been inverted. Inclusion of higher harmonics might provide more information and perhaps improve the resolution of the current 5 Hz inversion.

There is the potential for collaboration with Anne Tréhu to look for horizon A at the summit of Southern Hydrate Ridge, thought to be a salty pipe (Liu and Flemings, 2006). The presence of a 200 m hydrate pinnicle limited our ability to deep tow in this area, but a deployed transmitter developed for hydrate studies both eliminates navigational uncertainty and provides flexibility in utilizing CSEM technology where deep tow operations are hazardous or impossible to conduct.

# References


Abubakar, A., Habashy, T., Druskin, V., Alumbaugh, D., and Zerelli, A., 2006: Two-and-half-dimensional forward and inverse modeling for marine CSEM problems. In *SEG/New Orleans Annual Meeting*, 750–754.

Abubakar, A., Habashy, T., Druskin, V., Knizherman, L., and Alumbaugh, D., 2007: Two-and-half dimensional forward and inverse modelling for the interpretation of low-frequency electromagnetic measurements. EMI-Schlumberger.

Abubakar, A., Habashy, T., Druskin, V., Knizherman, L., and Alumbaugh, D., 2008: 2.5D forward and inverse modeling for interpreting low frequency electromagnetic measurements. *Geophysics*, **73**(4), F165–F177.

Anderson, W., 1979: Numerical integration of related Hankel transforms of orders 0 and 1 by adaptive digital filtering. *Geophysics*, **44**, 1287–1305.

Anderson, W. L., 1989: A hybrid fast Hankel transform algorithm for electromagnetic modeling. *Geophysics*, **54**(2), 263–266.

Archer, D., 2007: Methane hydrate stability and anthropogenic climate change. *Biogeosciences*, **4**, 521–544.

Archer, D., and Buffett, B., 2005: Time-dependent response of the global ocean clathrate reservoir to climatic and anthropogenic forcing. *Geochemistry Geophysics and Geosystems*, **6**(3), 1–13.

Archie, G. E., 1942: The electrical resistivity log as an aid in determining some reservoir characteristics. *Transactions of the American Institute of Mining and Metallurgical Engineers*, **146**, 54–62.

Behrens, J. P., 2005: *The Detection of Electrical Anisotopy in 35 Ma Pacific Lithosphere: Results from a Marine Controlled-Source Electromagnetic Survey and Implications for Hydration of the Upper Mantle*. PhD, University of California, San Diego, Scripps Institution of Oceanography.

Bevington, P. R., and Robinson, D. K., 2003: *Data Reduction and Error Analysis for the Physical Sciences*. McGraw Hill, 3 edition.

Bohrmann, G., Greinert, J., Suess, E., and Torres, M., 1998: Authigenic carbonates from the Cascadia subduction zone and their relation to gas hydrate stability. *Geology*, **26**, 647–650.

Buffett, B. A., 2000: Clathrate hydrates. *Annual Reviews Earth Planet Science*, **28**, 477–507.

Chatti, I., Delahaye, A., Fournaison, L., and Petitet, J.-P., 2005: Benefits and drawbacks of clathrate hydrates: a review of their areas of interest. *Energy Conversion and Management*, **46**, 1333–1343.

Chave, A. D., 1983: Numerical integration of related Hankel transforms by quadrature and continued fraction expansion. *Geophysics*, **48**(12), 1671–1686.

Chave, A. D., Constable, S. C., and Edwards, R. N., 1991: Electrical exploration methods for the seafloor. In *Electromagnetic Methods in Applied Geophysics*, editor M. Nabighian, chapter 12, 931–966. Society of Exploration Geophysicists.

Chave, A. D., and Cox, C., 1982: Controlled electromagnetic sources for measuring electrical-conductivity beneath the oceans .1. Forward problem and model study. *Journal of geophysical research*, **87**(NB7), 5327 –5338.

Cheesman, S., Edwards, R., and Chave, A., 1986: On the theory of sea-floor conductivity mapping using transient electromagnetic systems. *Geophysics*, **52**(2), 204–217.

Chevallier, J., Tréhu, A. M., Bangs, N. L., Johnson, J. E., and Meyer, H. J., 2006: Seismic sequence stratigraphy and tectonic evolution of Southern Hydrate Ridge. In *Proceedings of the Ocean Drilling Program, Scientific Results*, editors A. Tréhu, G. Bohrmann, M. Torres, and F. Colwell, volume 204, 1–29. College Station, TX.

Clague, D. A., Maher, N., and Paull, C. K., 2001: High-resolution multibeam survey of Hydrate Ridge, offshore Oregon. In *Natural Gas Hydrates Occurrence, Distribution and Detection*, editors C. K. Paull, and W. P. Dillon, volume 124 of *Geophysical Monograph*, 297–304. American Geophysical Union, Washington, DC.

Coggon, J., 1971: Electromagnetic and electrical modeling by finite element method. *Geophysics*, **36**(1), 132–155.

Collett, T., 1998: Well log evaluation of gas hydrate saturations. In *SPWLA 39$^{th}$ Annual Logging Symposium*, 1–14.

Collett, T. S., and Ladd, J., 2000: Detection of gas hydrate with downhole logs and assessment of gas hydrate concentrations (saturations) and gas volumes on the Blake Ridge with electrical resistivity log data. *Proceedings of the Ocean Drilling Program, Scientific Results*, **164**, 179–191.

Constable, S., 1990: Marine electromagnetic induction studies. *Surveys in Geophysics*, **11**, 303–327.

Constable, S., 2006: Marine electromagnetic methods – A new tool for offshore exploration. *The Leading Edge*.

Constable, S., and Cox, C. S., 1996: Marine controlled-source electromagnetic sounding 2. The PEGASUS experiment. *Journal of Geophysical Research*, **101**(B3), 5519–5530.

Constable, S., Orange, A., Hoversten, G., and Morrison, H. F., 1998: Marine magnetotellurics for petroleum exploration part 1: A sea-floor equipment system. *Grophysics*, **63**(3), 816–825.

Constable, S., and Weiss, C., 2006: Mapping thin resistors and hydrocarbons with marine EM methods: Insights from 1D modeling. *Geophysics*, **71**(2), G43–G51.

Constable, S. C., Parker, R., and Constable, C., 1987: Occam's inversion: A practical algorithm for generating smooth models from electromagnetic sounding data. *Geophysics*, **52**(3), 289–300.

Cox, C., Constable, S., and Chave, A., 1986: Controlled-source electromagnetic sounding of the oceanic lithosphere. *Nature*, **320**(6), 52–54.

Davis, T., and Duff, I., 1997: An unsymmetric pattern multifrontal method for sparse LU factorization. *SIAM Journal on Matrix Analysis and Applications*, **18**, 140–158.

Dawe, R. A., and Thomas, S., 2007: A large potential methane source– natural gas hydrates. *Energy Sources, Part A: Recovery, Utilization, and Environmental Effects*, **29**(3), 217–229.

deGroot Hedlin, C., and Constable, S., 1990: Occam's inversion to generate smooth, two-dimensional models from magnetotelluric data. *Geophysics*, **55**, 1613–1624.

DeMets, C., Gordon, R., Argus, D., and Stein, S., 1990: Current plate motions. *Geophysical Journal International*, **101**, 425–478.

Dickens, G., 2001: The potential volume of oceanic methane hydrates with variable external conditions. *Organic Geochemistry*, **32**, 1179–1193.

Dickens, G. T., 2003: Rethinking the global carbon cycle with a large dynamic and mirobially mediated gas hydrate capacitor. *Earth and Planetary Science Letters*, **213**, 169–183.

Dunbar, J., 2008: Electrical resistivity investigation of gas hydrate distribution in Mississippi Canyon Block 118, Gulf of Mexico. De-fc26-06nt42959, DOE/NETL Methane Hydrate Projects.

Dvorkin, J., Helgerud, M., Waite, W., Kirby, S., and Nur, A., 2003: *Coastal Systems and Continental Margins Natural Gas Hydrate in Oceanic and Permafrost Environments*, chapter Introduction to Physical Properties and Elastic Models, 245–260. Kluwer Academic Publishers, Netherlans.

Edwards, N., 2005: Marine controlled source electromagnetics: principles, methodologies, future commercial applications. *Surveys in Geophysics*, **26**, 675–700.

Edwards, R. N., 1997: On the resource evaluation of marine gas hydrate deposits using sea-floor transcient electric dipole-dipole methods. *Geophysics*, **62**(1), 63–74.

Edwards, R. N., and Chave, A. D., 1986: A transient electric dipole-dipole method for mapping the conductivity of the sea floor. *Geophysics*, **51**(4), 984–987.

Egbert, G., 1997: Robust multiple-station magnetotelluric data processing. *Geophysical Journal International*, **130**, 475–496.

Eidesmo, T., Ellingsrud, S., MacGregor, L. M., Constable, S., Sinha, M. C., Johansen, S., Kong, F. N., and Westerdahl, H., 2002: Sea bed logging (SBL), a new method for remote and direct identification of hydrocarbon filled layers in deepwater areas. *First Break*, **20**, 144–152.

Ellingsrud, S., Eidesmo, T., Johansen, S., Sinha, M., MacGregor, L., and Constable, S., 2002: Remote sensing of hydrocarbon layers by seabed logging (SBL): Results from a cruise offshore Angola. *The Leading Edge*, 972–982.

Ellis, M., Minshull, T., Best, A., Sinha, M., and Sothcott, J., 2006: Joint seismic and electrical measurements of gas hydrates in clastic sediments. In *AGU Fall Meeting San Franscisco*.

Evans, R., Constable, S., Sinha, M., and Unsworth, M., 1994: On the electrical nature of the axial melt zone at 13°N on the East Pacific Rise. *Journal of Geophysical Research*, **99**, 577–588.

Evans, R. L., 2007: Using CSEM techniques to map the shallow section of seafloor: From coastline to the edges of the continental slope. *Geophysics*, **72**(2), WA105–WA116.

Farquharson, C., and Oldenburg, D., 1998: Non-linear inversion using general measures of data misfit and model structure. *Geophysical Journal International*, **134**, 213–227.

Field, M., and Barber, J., 1993: *Submarine landslides: selected studies in the US exclusive economic zone*, chapter A submarine landslide associated with shallow seafloor gas and gas hydrates off Northern California, 151–157. US Geological Survey Bulletin.

Flosadóttir, A. H., and Constable, S., 1996: Marine controlled-source electromagnetic sounding 1. Modeling and experimental design. *Journal of Geophysical Research*, **101**(B3), 5507–5517.

Fox, R. C., Hohmann, G. W., Killpack, T. J., and Rijo, L., 1980: Topographic effects in resistivity and induced polarization surveys. *Geophysics*, **45**(1), 75–93.

Francisca, F., Yun, T., Ruppel, C., and Santamarina, J., 2005: Geophysical and geotechnical properties of near-seafloor sediments in the Northern Gulf of Mexico gas hydrate province. *Earth and Planetary Science Letters*, **237**, 924–939.

Fyke, J., and Weaver, A., 2006: The effect of potential future climate change on the marine methane hydrate stability zone. *Journal of Climate*, **19**, 5903–5917.

Gao, G., 2007: *2.5D Pixel Inversion Manual*. Schlumberger, EMI Technology Center, 1.0.0 edition.

Gorman, A. R., Holbrook, W., Hornback, M. J., Hackwith, K. L., Lizarralde, D., and Pecher, I., 2002: Migration of methane gas through the hydrate stability zone in a low-flux hydrate province. *Geology*, **30**(4), 327–330.

Goto, T.-N., Kasaya, T., Machiyama, H., Takagi, R., Matsumoto, R., Okuda, Y., Satoh, M., Watanabe, T., Seama, N., Mikada, H., Sanada, Y., and Kinoshita, M., 2008: A marine deep-towed DC resistivity survey in a methane hydrate area, Japan Sea. *Exploration Geophysics*, **39**, 52–59.

Griffiths, D. J., 1999: *Introduction to Electrodynamics*. Prentice Hall, 3 edition.

Habashy, T., and Abubakar, A., 2004: A general framework for constraint minimization for the inversion of electromagnetic measurements. *Progress in Electromagnetics Research PIER*, **46**, 265–312.

Hashin, Z., and Shtrikman, S., 1963: A variational approach to the theory of the elastic behaviour of multiphase materials. *Journal of Mechanics of Physical Solids*, **11**, 127–140.

Hesthammer, J., and Boulaenko, M., 2005: The offshore EM challenge. *First Break*, **23**, 59–66.

Hohmann, G. W., 1987: *Electromagnetic Methods in Applied Geophysics*, volume 1 of *Investigations in Geophysics Volume 3*, chapter 5: Numerical Modeling for Electromagnetic Methods of Geophysics, 313–363. Society of Exploration Geophysicists.

Hornback, M. J., Holbrook, S., Gorman, A. R., Hackwith, K. L., Lizarralde, D., and Pecher, I., 2003: Direct seismic detection of methane hydrate on the Blake ridge. *Geophysics*, **68**(1), 92–100.

Hovland, M., and Gudmestad, O. T., 2001: Potential influence of gas hydrates on seabed installations. In *Natural Gas Hydrates Occurrence, Distribution, and Detection*, editors C. K. Paull, and W. P. Dillon, Geophysical Monograph Series, 307–315. American Geophysical Union.

Hyndman, R. D., Yuan, T., and Moran, K., 1999: The concentration of deep sea gas hydrates from downhole electrical resistivity logs and laboratory data. *Earth and Planetary Science Letters*, **172**, 167–177.

Jiracek, G. R., 1990: Near-surface and topographic distortions in electromagnetic induction. *Surveys in Geophysics*, **11**, 163–203.

Jr, E. S., and Koh, C., 2007: *Clathrate Hydrates of Natural Gas, Third Edition*, volume Chemical Industries 119. CRC Press Taylor and Francis Group, 6000 Broken Sound Parkway NW, Suite 300 Boca Raton FL 33487-2742, 3 edition.

Kennett, J., Cannariato, K. G., Hendy, I. L., and Behl, R. J., 2003: *Methane Hydrates in Quaternary Climate Change The Clathrate Gun Hypothesis*. American Geophysical Union, Washington, DC.

Key, K., 2003: *Application of Broadband Marine Magnetotelluric Exploration to a 3D Salt Structure and a Fast-Spreading Ridge*. Ph.D. thesis, University of California, San Diego Scripps Institution of Oceanography.

Key, K., submitted: 1d dipole forward modeling code.

Klauda, J., and Sandler, S., 2005: Global distribution of methane hydrate in ocean sediment. *Energy and Fuels*, **19**, 459–470.

Kleinberg, R., 2006: New deposit accumulation model for marine gas hydrates. In *Offshore Technology Conference*, editor OTC, 18246. Offshore Technology Conference, OTC, P.O. Box 833836 Richardson Texas.

Koh, C. A., and Sloan, E., 2007: Natural gas hydrates: Recent advances and challenges in energy and environmental applications. *American Institute of Chemical Engineers*, **53**(7), 1636–1643.

Kong, F., 2007: Hankel transform filters for dipole antenna radiation in a conductive medium. *Geophysical Prospecting*, **55**, 83–89.

Kong, F., Johnstad, S. E., Rosten, T., and Westerdahl, H., 2008: A 2.5D finite element modeling difference method for marine CSEM modeling in stratified anisotropic media. *Geophysics*, **73**(1), F9–F19.

Kvenvolden, K., 1988: Methane hydrate - a major reservoir of carbon in the shallow geosphere? *Chemical Geology*, **71**, 41–51.

Kvenvolden, K., 1993a: Gas hydrates - geological perspective and global change. *Reviews of Geophysics*, **31**(2), 173–187.

Kvenvolden, K., 1999: Potential effects of gas hydrate on human welfare. In *Proceedings of the National Academy of Science*, volume 96, 3420–3426.

Kvenvolden, K., 2000: Gas hydrate and humans. *Annals of the New York Academy of Sciences*, **912**, 17–22.

Kvenvolden, K., 2003: Coastal systems and continental margins natural gas hydrate in oceanic and permafrost environments. In *Natural Gas Hydrate: Background and History of Discovery*, editor M. D. Max, 9–16. Kluwer Academic Publishers, Netherlands.

Kvenvolden, K., 2005: Gaia's breath- global methane exhalations. *Marine and Petroleum Geology*, **22**, 579–590.

Kvenvolden, K., Ginsburg, G., and Soloviev, V., 1993: Worldwide distribution of subaquatic gas hydrates. *Geo-Marine Letters*, **13**, 32–40.

Kvenvolden, K. A., 1993b: Gas hydrates - geological perspective and global change. *Reviews of Geophysics*, **32**(2), 173–187.

Lee, M., and Collett, T., 2001: Comparison of elastic velocity models for gas-hydrate-bearing sediments. In *Natural Gas Hydrates: Occurrence, Distribution and Detection*, editors C. Paull, and W. Dillon, Geophysical Monograph Series 124, 179–187. American Geophysical Union, Washington D.C.

Lee, S., Liang, L., Riestenberg, D., West, O., Tsouris, C., and Adams, E., 2003: CO2 hydrate composite for ocean carbon sequestration. *Environmental Science Technology*, **15**(37), 3701–8.

Li, Y., and Constable, S., 2007: Two dimensional marine controlled source electromagentic modelling, Part 2: Bathymetry effects. *Geophysics*, **72**(2), WA63–WA71.

Li, Y., and Key, K., 2007: Two dimensional marine controlled source electromagentic modelling, Part 1: An adaptive finite element algorithm. *Geophysics*, **72**(2), WA51–WA62.

Liu, X., and Flemings, P. B., 2006: Passing gas through the hydrate stability zone at southern hydrate ridge, offshore oregon. *Earth and Planetary Science Letters*, **241**, 211–226.

Løseth, L. O., Pedersen, H. M., Ursin, B., Amundsen, L., and Ellingsrud, S., 2006: Low-frequency electromagnetic fields in applied geophysics: Waves or diffusion? *Geophysics*, **71**(4), W29–W40.

MacGregor, L., Constable, S., and Sinha, M., 1998: The ramesses experiment iii: Controlled source electromagnetic sounding of the reykjanes ridge at $57^o$ 45'n. *Geophysics Journal International*, **135**, 772–789.

MacKay, M. E., Moore, G. F., Cochrane, G. R., Moore, J., and Kulm, L. D., 1992: Landward vergence and oblique structural trends in the orrgon margin accretionary prism: Implications and effect on fluid flow. *Earth and Planetary Science Letters*, **109**, 477–491.

Malone, R., 1985: Gas hydrates topical report. DOE/METC/SP-218, U.S. Department of Energy.

Marquardt, D. W., 1963: An algorithm for least-squares estimation of nonlinear parameters. *Journal of the Society for Industrial and Applied Mathematics*, **11**(2), 431–441.

Max, M., Johnson, A., and Dillon, W., 2006: *Economic Geology of Natural Gas Hydrate*. Springer.

Mienert, J., Vanneste, M., Bunz, S., Andreassen, K., Haflidason, H., and Sejrup, H. P., 2005: Ocean warming and gas hydrate stability on the mid-Norwegian margin at the Storegga slide. *Marine and Petroleum Geology*, **22**, 233–244.

Milkov, A. V., 2004: Global estimates of hydrate bound gas in marine sediments: how much is really out there? *Earth Science Reviews*, **66**, 183–197.

Milkov, A. V., 2005: Molecular and stable isotope compositions of natural gas hydrates: A revised global dataset and basic interpretations in the context of geological settings. *Organic Geochemistry*, **36**, 681–702.

Milkov, A. V., Dickens, G. R., Claypool, G. E., Lee, Y.-J., Borowski, W. S., Torres, M. E., Xu, W., Tomaru, H., Trehu, A. M., and Schultheiss, P., 2004: Co-existence of gas hydrate, free gas, and brine within the regional gas hydrate stability zone at Hydrate Ridge (Oregon margin): evidence from prolonged degassing of a pressurized core. *Earth and Planetary Science Letters*, 829–843.

Milkov, A. V., and Sassen, R., 2002: Economic geology of offshore gas hydrate accumulations and provinces. *Marine and Petroleum Geology*, **19**, 1–11.

Mitsuhata, Y., 2000: 2-D electromagnetic modeling by finite-element method with a dipole source and topography. *Geophysics*, **65**(2), 465–475.

Moridis, G., and Sloan, E., 2007: Gas production potential of disperse low-saturation hydrate accumulations in ocean sediments. *Energy Conversion and Management*, **48**, 1834–1849.

Nabighian, M. N., editor, 1996: *Electromagnetic Methods in Applied Geophysics*, volume 2 Application, Part A and B. Society of Exploration Geophysicists.

Newman, G. A., and Alumbaugh, D. L., 1995: Frequency-domain modelling of airborne electromagnetic responses using staggered finite differences. *Geophysical Prospecting*, **43**, 1021–1042.

Nixon, M., and Grozic, J., 2007: Submarine slope failure due to gas hydrate dissociation: a preliminary quantification. *Canadian Geotechnical Journal*, **44**, 314–325.

Ostergaard, K., Tohidi, B., Danesh, A., and Todd, A., 2000: Gas hydrates and offshore drilling predicting the hydrate free zone. *Annals New York Academy of Sciences*, **912**, 411–419.

Paull, C., III, W. U., and Holbrook, W., 2007: Assessing methane release from the colossal Storregga submarine landslide. *Geophysical Research Letters*, **34**(L04601).

Paull, C., and Ussler, W. I., 2001: *Natural Gas Hydrate: Occurrence, Distribution and Detection*, chapter History and significance of gas sampling during the DSDP and ODP, 53–66. Number 124 in Geophysics Monograph. American Geophysical Union.

Pearson, C., Murphy, J., and Hermes, R., 1986: Acoustic and resistivity measurements on rock samples containing tetrahydrofuran hyrates: laboratory analogues to natural gas hydrate deposits. *Journal of Geophysical Research*, **91**(B14), 14132–14138.

Pearson, C. F., Halleck, P. M., McGuire, P. L., Hermes, R., and Mathews, M., 1983: Natural gas hydrate deposits: A review of *in situ* properties. *Journal of Physical Chemistry*, **87**, 4180–4185.

Pridmore, D., Hohmann, G. W., Ward, S. H., and Sill, W., 1981: An investigation of finite element modeling for electrical and electromagnetic data in three dimensions. *Geophysics*, **46**(7), 1009–1024.

Riedel, M., Long, P., Liu, C. S., Schultheiss, P., and Party, O. L. . S., 2003: Ocean drilling program (ODP) Leg 204 physical properties: stratigraphic and structural control of hydrate formation. In *Geophysical Research Abstracts*, volume 5.

Sadiku, M. N., 2001: *Numerical Techniques in Electromagnetics*. CRC Press LLC, 2 edition.

Santamarina, J., Francisca, F., Yun, T., Lee, J., Martin, A., and Ruppel, C., 2004: Mechanical, thermal, and electrical properties of hydrate-bearing sediments. In *AAPG Hedberg Conference Gas Hydrates: Energy Resource Potential and Associated Geologic Hazards*.

Schlumberger, 2008: Logging While Drilling Oilfield Glossary.

Schmeling, H., 1986: Numerical models on the influence of partial melt on eleastic and anelastic and electrical properties of rocks. Part II: electrical conductivity. *Physics of the Easrth and Planetary Interiors*, **43**, 123–136.

Schwalenberg, K., Willoughby, E., Mir, R., and Edwards, R. N., 2005: Marine gas hydrate electromagnetic signatures in Cascadia and their correlation with seismic blank zones. *first break*, **23**, 57–63.

Shewchuk, J. R., 2002: Delaunay refinement algorithms for triangular mesh generation. *Computational Geometry*, **22**, 21–74.

Shipboad Scientific Party, 2003a: Explanatory notes. In *Proceedings Ocean Drilling Program ODP Leg 204 Initial Reports*, editors A. Tréhu, G. Bohrmann, F. Rack, M. Torres, and et al., volume 204, 1–102 [CD–ROM]. Ocean Drilling Program, Texas A&M University, College Station TX 77845-9547, USA.

Shipboad Scientific Party, 2003b: Leg 204 summary. In *Proceedings Ocean Drilling Program ODP Leg 204 Initial Reports*, editors A. Tréhu, G. Bohrmann, F. Rack, M. Torres, and et al., volume 204, 1–75 [CD–ROM]. Ocean Drilling Program, Texas A&M University, College Station TX 77845-9547, USA.

Shipboad Scientific Party, 2003c: Site 1244. In *Proceedings Ocean Drilling Program Initial Reports*, editors A. Tréhu, G. Bohrmann, F. Rack, M. Torres, and et al., volume 204, 1–132 [CD–ROM]. Ocean Drilling Program, Texas A&M University, College Station TX 77845-9547, USA.

Shipboad Scientific Party, 2003d: Site 1245. In *Proceedings Ocean Drilling Program Initial Reports*, editors A. Tréhu, G. Bohrmann, F. Rack, M. Torres, and et al., volume 204, 1–131 [CD–ROM]. Ocean Drilling Program, Texas A&M University, College Station TX 77845-9547, USA.

Shipboad Scientific Party, 2003e: Site 1246. In *Proceedings Ocean Drilling Program Initial Reports*, editors A. Tréhu, G. Bohrmann, F. Rack, M. Torres, and et al., volume 204, 1–131 [CD–ROM]. Ocean Drilling Program, Texas A&M University, College Station TX 77845-9547, USA.

Shipboard Scientific Party, 2003: Proceedings ODP, Initial Reports. In *Leg 204 Summary*, editors A. M. Trehu, G. Bohrmann, F. R. Rack, M. E. Torres, and et al., volume 204, chapter Leg 204 summary, 1–75. Ocean Drilling Program, College Station TX.

Shipley, T. H., Houston, M. H., Buffler, R. T., Shaub, F. J., McMillen, K. J., Ladd, J. W., and Worzel, J., 1979: Seismic evidence for widespread possible gas hydrate horizons on continetal slopes and rises. *AAPG Bulletin- American Association of Petroleum Geologists*, **63**(12), 2204–2213.

Sloan, E., 2003: Fundamental principles and applications of natural gas hydrates. *Nature*, **426**, 353–363.

Sloan, E. D., 1990: *Clathrate Hydrates of Natural Gas*. Marcel Dekker Inc., New York.

Smith, B., and Ward, S., 1974: Short note: On the computation of polarization ellipse parameters. *Geophysics*, **39**(6), 867–869.

Smith, D., Shi, S., and et al., R. C., 2004: The Holocene Storrega slide tsunami in the United Kingdom. *Quaternary Science Review*, **23**(23-24), 2291–2321.

Spangenberg, E., 2001: Modeling of the influence of gas hydrate content on electrical properties of porous sediments. *Journal of Geophysical Research*, **106**(B4), 6535–6548.

Spangenberg, E., Kulenkampff, J., Naumann, R., and Erzinger, J., 2005: Pore space hydrate formation in a glass bead sample from methane dissolved in water. *Geophysical Research Letters*, **32**(L24301), DOI:10.1029/2005GL024107.

Stern, L., Kirby, S., Circone, S., and Durham, W., 2004: Scanning electron microscopy investigations of laboratory grown gas clathrate hydrates formed from melting ice and comparison to natural hydrates. *American Mineralogist*, **89**, 1162–1175.

Stratton, J., 1941: *Electromagnetic Theory*. McGraw-Hill Book Company, Inc.

Sultan, N., Cochonat, P., Foucher, J. P., and Mienert, J., 2004: Effect of gas hydrates melting on seafloor slope instability. *Marine Geology*, **213**, 379–401.

Telford, W. M., Geldart, L., and Sheriff, R., 1998: *Applied Geophysics*. Cambridge University Press, second edition.

Torres, M. E., Wallmann, K., Tréhu, A. M., Bohrmann, G., Borowski, W., and Tomaru, H., 2004: Gas hydrates growth, methane transport, and chloride enrichment at the Southern Summit of Hydrate Ridge, Cascadia margin off Oregon. *Earth and Planetary Science Letters*, **226**, 225–241.

Tréhu, A., Torres, M., Bohrmann, G., and Colwell, F., 2006: Leg 204 Synthesis: Gas hydrate distribution and dynamics in the Central Cascadia accretionary complex. In *Proceedings of the Ocean Drilling Program, Scientific Results*, editors A. Treéhu, G. Bohrmann, M. Torres, and F. Colwell, volume 204, 1–40.

Tréhu, A. M., and Bangs, N., 2001: 3-D seismic imaging of an active margin hydrate system, Oregon continental margin report of cruise ttn112. Data Report 182, Oregon State University.

Tréhu, A. M., Bohrmann, G., Rack, F., Torres, M., and Shipboard Scientific Party, 2003: Procedings ODP, Initial Reports. *Available from: Ocean Drilling Program, Texas A&M University, College Station TX 77845-9547,USA*, **204** [**CD-ROM**].

Tréhu, A. M., and Flueh, E. R., 2001: Estimating the thickness of the free gas zone beneath Hydrate Ridge, Oregon continental margin, from seismic velocities and attenuation. *Journal of Geophysical Research*, **106**(B2), 2035–2045.

Tréhu, A. M., Long, P. E., Torres, M. E., Bohrmann, G., Rack, F. R., Collett, T. S., Goldberg, D. S., Milkov, A. V., Reidel, M., Schultheiss, P., Bangs, N. L., Barr, S. R., Borowski, W. S., Claypool, G. E., Delwiche, M. E., Dickens, G., Garcia, E., Guerin, G., Holland, M., Johnson, J. E., Lee, Y.-J., Liu, C.-S., Su, X., Teichert, B., Tomaru, H., Vanneste, M., Watanabe, M., and Weinberger, J. L., 2004: Three-dimensional distribution of gas hydrate beneath southern Hydrate Ridge: constraints from ODP Leg 204. *Earth and Planetary Science Letters*, **222**, 845–862.

Tréhu, A. M., Torres, M., Moore, G., Suess, E., and Bohrmann, G., 1999: Temporal and spatial evolution of a gas hydrate bearing accretionary ridge on the Oregon continental margin. *Geology*, **27**, 939–942.

Tzirita, A., 1992: *A study of electrical and thermal properties and their use to detect natural gas hydrates in ocean sediments*. PhD, Texas A&M University.

Unsworth, M., Travis, B. J., and Chave, A. D., 1993: Electromagnetic induction by a finite electric dipole source over a 2-d earth. *Geophysics*, **58**(2), 198–214.

Vozoff, K., 1991: *Electromagnetic Methods in Applied Geophysics*, chapter The magnetotelluric method, 641–711. Society of Exploration Geophysicists, 2 edition.

Ward, S. H., and Hohmann, G. W., 1987: *Electromagnetic Methods in Applied Geophysics*, volume 1 of *Investigations in Geophysics*, chapter 4 Electromagnetic Theory for Geophysical Applications, 131–311. Society of Exploration Geophysicists.

Weitemeyer, K., Constable, S., and Key, K., 2006a: Marine EM studies of Hydrate Ridge, Oregon, USA-imaging hydrates and the accretionary complex. In *EM Workshop*. El Vendrell, Spain.

Weitemeyer, K., Constable, S., and Key, K., 2006b: Marine EM techniques for gas-hydrate detection and hazard mitigation. *Leading Edge*, **25**(5), 629–632.

Weitemeyer, K., Constable, S., Key, K., and Behrens, J., 2006c: First results from a marine controlled-source electromagnetic survey to detect gas hydrates offshore Oregon. *Geophysical Research Letters*, **33**(L03304), doi:10.1029/2005GL024896.

Winters, W., Dillon, W., Pecher, I., and Mason, D., 2003: *Natural Gas Hydrates: Background and History of Discovery*, chapter GHASTLI- Determining physical properties of sediment containing natural and laboratory formed gas hydrate, 311–322. Kluwer Academic Publishers.

Yee, K. S., 1966: Numerical solution of initial boundary value problems involving Maxwell's equations in isotropic media. *IEEE Transactions on Antennas and Propagation*, **AP-14**(3), 302–307.

Yuan, J., and Edwards, R. N., 2000: The assessment of marine gas hydrates through electronic remote sounding: Hydrate without a BSR? *Geophysical Research Letters*, **27**(16), 2397–2400.

Yun, T., Narsilio, G., Santamarina, J., and Ruppel, C., 2006: Instrumented pressure testing chamber for characterizing sediment cores recovered at in sity hydrostatic pressure. *Marine Geology*, **229**, 285–293.

Zatsepina, O. Y., and Buffett, B., 2001: Experimental study of the stability of $CO_2$ hydrate in a porous medium. *Fluid Phase Equilibria*, **192**, 85–102.

Zatsepina, O. Y., and Buffett, B., 2002: Nucleation of $CO_2$-hydrate in a porous medium. *Fluid Phase Equilibria*, **200**, 263–275.

Zhang, Z., and McMechan, G. A., 2003: *Elastic Inversion and interpretation of seismic data from Hydrate Ridge, offshore Oregon, with emphasis on structural controls of the distribution and concentration of gas hydrate and free gas*. Masters thesis, Center for Lithospheric Studies, The University of Texas at Dallas, PO Box 830688, Richardson, TX 75083-0688, USA.

Zienkiewicz, O., 1977: *The finite element method*. McGraw-Hill Book Co.